Exploring the Tumor and Premetastatic Microenvironment of the Ovary

Curtis McCloskey

Thesis submitted to the Faculty of Graduate and Postdoctoral Studies in partial fulfillment of the requirements for a doctoral degree in Cellular and Molecular Medicine.

Department of Cellular and Molecular Medicine

Faculty of Medicine

University of Ottawa

Dedication

This thesis is dedicated to Ms. Margaret Craig for her strength, compassion, and generosity in the face of ovarian cancer, without whom a large portion of this work would have remained an idea.

Authorization

Chapters 2 and 3 appear in the journals Frontiers in Oncology, and Journal of Biomedical Optics, respectively, and are authorized to be reproduced in this thesis.

The preclinical model section of Chapter 1 is based on our review article that appears in the journal Cancers (Basel) and is partially reproduced here with authorization from the publisher. See reference McCloskey et al., 2018.

“Science, like the Mississippi, begins in a tiny rivulet in the distant forest. Gradually other streams swell its volume. And the roaring river that bursts the dikes is formed from countless sources.”

-The usefulness of useless knowledge, Abraham Flexner, 1939

Abstract

Ovarian cancers are the most lethal gynecological malignancies, responsible for more than 150,000 deaths around the globe annually. Among ovarian cancers, high-grade serous ovarian cancer has a 5-year survival rate of only 40%. This poor survival is due to a widespread lack of understanding of this disease, from suboptimal prevention and screening methods to failures in treatment. Moving towards novel prevention and treatment methods requires better models of ovarian cancer that phenotypically and genetically recapitulate the features of ovarian cancers that are seen clinically. This thesis highlights the characterization of a novel syngeneic model of high-grade serous ovarian cancer that exhibits the growth, expression profile, histology, and a tumor-initiating cell population that closely resembles human disease. We expand on our initial characterization of the STOSE model in a proof-of-principle study using deep learning of second-harmonic generation and two-photon-excited-fluorescence images to classify normal compared to cancerous tissues. The use of deep learning for image classification based on extracellular matrix and cellular structure could have robust application to complementing common histological examination of tissues and in treatment planning. Building on the changes in structure found in normal compared to cancerous ovarian tissue and recent research that showed age-associated fibrosis develops in murine ovaries, we assessed the non-hereditary ovarian cancer risk factors of age and ovulation number for their effects in altering ovarian tissue structure. This thesis concludes with the first evidence of ovarian fibrosis in non-pathological post-

menopausal human ovaries. We show that ovarian fibrosis correlates with the development of a pre-metastatic (tumor-permissive) niche, revealing a novel avenue of research into ovarian cancer risk. Interestingly, age-associated fibrosis could be prevented or reversed by metformin use, revealing a possible mechanism for the previously identified ovarian cancer risk reduction seen with metformin use and further supporting the use of metformin for ovarian cancer prevention.

Table of contents

List of tables

List of figures

List of abbreviations

°C - Degrees Celsius
3D – Three dimensional
ABC – ATP-binding cassette
Ad-Cre – Adenovirus Cre recombinase
ANOVA - Analysis of variance
CD - Cluster of Differentiation
cDNA - Complementary DNA
CNN – Convolutional neural network
CO2 - Carbon dioxide
CSC – Cancer stem cell
DAB - Diaminobenzidine
DNA - Deoxyribonucleic acid
DPP4 – Dipeptidyl peptidase-4
ECM - Extracellular matrix
EMT - Epithelial-to-mesenchymal transition
EOC – Epithelial ovarian cancer
FC – Fully-connected
FFPE – Formalin-fixed paraffin-embedded
FTE - Fallopian tube epithelium
GEMM – Genetically engineered mouse model
GO - Gene ontology
h - Hour(s)
H_2O_2 - Hydrogen peroxide
HGSC – High-grade serous ovarian cancer
HRP - Horseradish peroxidase
IB - Intrabursal
IP - Intraperitoneal
IPA – Ingenuity pathway analysis
IUD – Intrauterine device
KO - Knockout
LGSC – Low-grade serous ovarian cancer
LoxP - Locus of X-over P1
M - Molar
mg - Milligram(s)
MHC – Major histocompatibility complex
min - Minute(s)
mL - Milliliter(s)
mm – Millimeter
mM - Millimolar
MOSE - Mouse ovarian surface epithelium

M-PER - Mammalian protein extraction reagent
mRNA - Messenger RNA
MTS – Masson's trichrome stain
ng - Nanogram(s)
OC – Oral contraceptive
OSE - Ovarian surface epithelium
PBS - Phosphate-buffered saline
PCOS – Polycystic ovarian syndrome
PCR - Polymerase chain reaction
PET – Positron-emission tomography
PMN – Pre-metastatic niche
qPCR - Quantitative reverse transcription polymerase chain reaction
RA – Retinoic acid
RNA - Ribonucleic acid
RRSO – Risk-reducing salpingo-oophorectomy
RT-PCR - Reverse transcription-polymerase chain reaction
SCA1 – Stem-cell antigen-1
sec - Second(s)
SEM - Standard error of the mean
SHG – Second-harmonic generation
STIC – Serous tubal intraepithelial carcinoma
STOSE – Spontaneously transformed ovarian surface epithelium
SV40TAg – Simian-virus large T-antigen
SVM – Support vector machine
T2D – Type 2 diabetes
TGFβ - Transforming Growth Factor Beta
TIC – Tumor-initiating cell
TME - Tumor microenvironment
TPEF – Two-photon excitation fluorescence
UV – Ultraviolet
VCD – 4-vinylcyclohexene diepoxide
WT - wildtype
µg - microgram(s)
µL - microliter
µm – micrometer

Acknowledgements

There are so many people and experiences that have led me to complete this body of work over the past 6 years. First and foremost, I thank Dr. Barbara Vanderhyden who has been a mentoring marvel, for shaping me into a scientist with a strong skillset to forge into the academic world. You have taught me grant and paper writing, professionalism, the value of good controls, and most importantly, the value of teamwork and collaboration in science. From barging into your office unannounced with crazy ideas, you always listened no matter how far-fetched the idea, giving me the confidence that my ideas have worth. Your passion for science, for training the next generation of scientists, and for bringing students and patients together, have been the most inspiring parts of graduate school. Our work on the Let's Talk Science volunteer program has been a great addition to my training. I am very proud of everything we achieved with Let's Talk Science, from AMP, EWC, LTC, and Science Travels. You have created not only a patient advocate, but a scientist with a passion for inspiring youth and promoting science literacy.

Many thanks to my thesis advisory committee, Drs. Doug Gray, Michele Ardolino, Christine Pratt, and Ben Tsang for not only challenging me but also for their support and faith in the dynamic nature of my projects over the course of graduate school.

I thank Ken Garson, Elizabeth Macdonald, and Olga Collins for all of their help over the years and for always being a welcoming ear for anything life or science related, you have all been so important in my successes. I'd also like to acknowledge my lab mates, in particular Dr. Atefeh Abedini, and Dr. Galaxia Rodriguez, for all of their support, brainstorming, and laughs.

I would not have made it this far without my friends. Thank you to Danny Jomaa, Tabassom Baghai, and Andrea Ibrahim for your ongoing support over the last few years, you've given me many fond memories from working at the Cancer Centre.

I've been fortunate to have an extremely supportive family. Thank you to my parents, Donna and Tom McCloskey, and my brother and sister-in-law, Tyler and Sally McCloskey for their continuous support during graduate school.

Finally, a special thank you to my partner Patrick Teed, who has inspired and supported me throughout graduate school.

1 CHAPTER 1: GENERAL INTRODUCTION

1.1 Ovarian cancer incidence

Ovarian cancers are the eighth leading cause of cancer-associated deaths being responsible for 151,900 deaths globally in 2012 (Coburn et al., 2017). Among gynecological malignancies, ovarian cancers are the most lethal in the western world and are the second most lethal in Eastern Asia behind uterine cancers (Auersperg, 2013a; Lee et al., 2014). Ovarian cancer incidence has remained largely stable over the past 35 years with over 230,000 new cases in 2012 with the highest incidence in Europe, particularly in Latvia where incidence is 14.3 per 100,000 person-years (Coburn et al., 2017). In contrast, the lowest incidence is seen in Asia/Oceania, with the lowest risk in Thailand where incidence is 5.7 per 100,000 person-years (Coburn et al., 2017). Interestingly, incidence is proportional to the level of regional development, speculated to be driven by an increase in risk from low parity, accessible hormonal replacement therapy, genetic pre-disposition, and lower oral contraceptive use (Europe and the Americas) that is characteristic of developed regions (Coburn et al., 2017).

1.2 Ovarian cancer subtypes

Ovarian cancer was historically thought to be a singular disease; however, research efforts over the past few decades have identified numerous subtypes with differential risk factors, associated genetic alterations, incidence, mortality rates, and treatment response (reviewed in Coburn et al., 2017; Galic et al., 2013; Torre et al., 2018;

Wentzensen et al., 2016). Subtypes are largely based on the histologic presentation and genetic similarity to precursor tissues. Ovarian cancers are broadly divided into three subtypes: epithelial ovarian cancer (EOC), which is the most common subtype encompassing ~90% of ovarian cancers, and the rarer germ cell (5-8%) and sex-cord stromal (3-5%) subtypes (Auersperg, 2013a). These subtypes can be further subdivided, with sex-cord stromal cancers comprised of adult granulosa cell tumors, and Sertoli-Leydig cell tumors with characteristic *FOXL2* and *DICER1* mutations, respectively (Karnezis et al., 2017). These cancers are thought to develop from the stromal granulosa cells of the ovary (Karnezis et al., 2017). Germ cell tumors are subdivided into embryonal carcinoma, teratoma, yolk-sac tumor, choriocarcinoma, and seminomas based on differentiation profiles and histology (reviewed in Cools et al., 2011). EOC is subdivided into type 1 carcinomas: low-grade serous (LGSC, 3%), endometrioid (10%), clear-cell (10%), and mucinous (3%), and the aggressive type II carcinoma: high-grade serous carcinoma (HGSC, ~65%) (Auersperg, 2013a). Subtype classification and diagnosis is currently performed by highly-skilled pathologists using a panel of immunohistochemical markers along with tumor histology. However, in a step towards automation, new methodologies are currently in development that use machine learning of non-linear microscopy images of unstained tumor sections to classify ovarian cancer subtypes (Wen et al., 2016, 2014).

1.2.1 Type I ovarian carcinomas

Endometrioid and clear-cell carcinomas are thought to develop from endometriosis with characteristic *PTEN* and *ARID1A* mutations, and with increased risk seen in familial Lynch syndrome (Karnezis et al., 2017; Koshiyama et al., 2017). Similarly, mucinous tumors are thought arise from endometriosis or a teratoma with characteristic *KRAS* mutations (Karnezis et al., 2017; Koshiyama et al., 2017). Among serous EOC, LGSCs are genetically stable, indolent tumors that are refractory to most conventional chemotherapeutics, and are thought to arise from benign ovarian cystadenomas or serous borderline tumors (Galic et al., 2013; Koshiyama et al., 2017). LGSCs often present with *KRAS, BRAF, or PTEN* mutations (Wentzensen et al., 2016). Type I carcinomas generally have a better prognosis than type II carcinomas and given that type I tumors have characteristic mutations, numerous targeted therapies are currently in development to improve treatment (reviewed in Galic et al., 2013).

1.2.2 Type II: high-grade serous carcinoma

HGSC is the most common (70% of EOC cases) and aggressive subtype with a 5-year survival of just 43% compared to >60% for all other subtypes (Torre et al., 2018). Importantly, 5-year survival increases to 93% when HGSC is detected at localized stage I (Torre et al., 2018); however, this rarely occurs. Poor survival is largely due to a lack of sensitive screening methods and non-specific symptoms such as bloating, back pain, and fatigue that lead to women presenting with stage III or IV disseminated disease

(Torre et al., 2018). In two major screening trials, UKTOCS and PLCO, screening using transvaginal sonography and annual serum CA-125 levels did not improve EOC-specific mortality, highlighting the challenges and poor efficacy of worldwide screening efforts (Henderson et al., 2018). This was not surprising as serum CA-125 has poor sensitivity with a false positive rate of 4.2% and suboptimal specificity as elevated CA-125 can be present in women with benign disease, often leading to unnecessary surgery and increased surgery-associated complications (Henderson et al., 2018; Mannis et al., 2013). Numerous other biomarkers such as HE4 and biomarker panels often containing inflammatory mediators (TNFα, CRP, IL8) have been tested, although most of these methods have yet to improve screening and lack wide-spread uptake (Menon et al., 2018; Trabert et al., 2014). This stresses the need to improve our understanding of ovarian cancer development in order to generate screening methods with increased sensitivity and specificity that can detect disease or risk of disease at an earlier stage.

The lack of screening methods is also in part due to a long-standing controversy over the origin(s) of HGSC that has led to numerous resources being used in attempts to resolve this debate. For decades, it was thought that ovarian cancer initiates from the single layer of epithelium that lines the ovary, the ovarian surface epithelium (OSE); however, no bonafide precursor lesions have been identified beyond dysplasia of the OSE layer and epithelial inclusion cysts within the ovarian stroma (Auersperg, 2013a).

The origin debate largely stems from a study by Piek and colleagues (2001), where they showed dysplasia in the fallopian tube epithelium (FTE) in prophylactically removed tubes from high-risk women. This finding along with FTE differentiation common within epithelial ovarian inclusion cysts has catalyzed the research community to study an FTE origin of HGSC. These dysplasias are referred to as serous tubal intraepithelial carcinomas (STICs) and p53 signatures, which have shared genetic alterations and are histologically similar to HGSC (Karnezis et al., 2017). It is now generally accepted that the majority of ovarian cancers are FTE-derived, particularly in high-risk women (Karnezis et al., 2017). Yet, an OSE origin should not be fully discounted as there is evidence that salpingectomy alone does not fully protect against HGSC, given the development of bilateral HGSC in a patient three years following salpingectomy (Sato et al., 2017). Clinical trials are currently underway where salpingectomy alone is being compared to risk-reducing salpingo-oophorectomy (RRSO) in high-risk women (Menon et al., 2018; Nebgen et al., 2018). High-risk women are classified as those with familial mutations in predominantly the *BRCA1/2* genes, and less commonly, mutations in *BRIP1, PALB2, RAD51C,* and *RAD51D* (Karnezis et al., 2017). Hereditary cases represent only ~10% of HGSC (Auersperg, 2013a; Karnezis et al., 2017). Interestingly, among both sporadic and hereditary cases of HGSC, *TP53* mutation is the most common genetic alteration, being mutated in up to 94% of HGSCs with 35% of these tumors expressing high levels of TP53 and 62% expressing little to no detectable TP53

(Cole et al., 2016). Given the aggressive nature, frequency, and poor survival of HGSC, the majority of this thesis has focused on modeling HGSC and strategies to prevent it.

1.3 Chemoresistance and cancer stem cells

Beyond the origin(s) of disease, HGSC presents a clinical challenge due to the frequent development of chemoresistance (Cornelison et al., 2017). The standard of care is debulking surgery followed by a combination of carboplatin and paclitaxel chemotherapy. Even though over 80% of patients initially respond to this treatment, chemoresistant disease recurs in 60% of patients within 5 years (Cornelison et al., 2017). Intrinsic tumor chemoresistance can originate from a lack of drug accessibility through neovasculature, enhanced drug metabolism and drug efflux mechanisms, and extracellular matrix (ECM)-tumor cell interactions (Cornelison et al., 2017). Tumors can also acquire resistance through microevolution during treatment where they acquire escape mechanisms and persist (Cornelison et al., 2017). Treatment-driven tumor microevolution was initially thought to occur through clonal evolution whereby clones with a survival advantage persist and essentially purify the tumor cell population. Since HGSC is characterized by a high-degree of tumor heterogeneity, clonal evolution could produce tumor heterogeneity through the escape of multiple genetically dissimilar clones or through multiple genetic events within a single escaped clone (Cornelison et al., 2017; Foster et al., 2013). In contrast to the clonal evolution model, the Cancer Stem Cell (CSC) model posits that tumors are made up of heterogeneous cell populations that

differentiate along a hierarchy similar to the development of the neural and hematopoietic systems (Roy and Cowden Dahl, 2018). A hierarchical pattern of inheritance from a progenitor-like cell, for example, during treatment escape, could generate the heterogeneity that is characteristic of ovarian cancer recurrences (Foster et al., 2013). In addition, CSCs are characterized by slow turnover and the ability to initiate tumor formation from a small number of cells (Foster et al., 2013). This slow turnover of CSCs is thought to be a prime cause of recurrence in ovarian cancer patients, as traditional chemotherapeutics target rapidly dividing cells (Foster et al., 2013; Raja et al., 2013). In addition, similar to canonical stem cells, CSCs express drug efflux pumps (ABC transporters), and glutathione reductase for enhanced catabolism of chemotherapeutics (Foster et al., 2013; Roy and Cowden Dahl, 2018). CSCs can also exhibit asymmetric cell division, yielding differentiated tumor cells and replenishing the CSC pool, thereby providing a continuous source of chemoresistant cells (Foster et al., 2013).

Bapat and colleagues (2005) provided the first evidence that CSCs exist within EOC by isolating a single tumorigenic clone from patient ascites fluid. This single clone possessed stem cell characteristics and was able to generate tumors upon xenograft into immunocompromised mice (Bapat et al., 2005). Numerous ovarian cancer CSC markers have since been identified including CD44, CD133, CD117, CD24, and ALDH1 (Garson et al., 2012; Kulkarni-Datar et al., 2013; Parte et al., 2018). Recent

work in our lab has identified Stem Cell Antigen-1 (SCA1, also known as Ly6A) as the first defined marker of a normal OSE progenitor population *in vivo* (Gamwell et al., 2012). SCA1 is α-glycosyl phosphatidylinositol-anchored cell surface protein, implicated in the regulation and co-activation of cell signaling pathways (Holmes and Stanford, 2007). SCA1 has been used as a marker to isolate murine hematopoietic and cardiac stem cells (Holmes and Stanford, 2007). Of note, SCA1 is murine specific with no human homolog (Holmes and Stanford, 2007), constraining the study of SCA1+ CSCs to murine models. However, SCA1 represents one of the few defined markers of an OSE progenitor cell population, enabling studies on the transition from normal stem cells to CSCs. Other ovarian cancer CSC markers (CD44, CD133, and CD117) have yet to be identified as markers of OSE progenitors in normal tissue (Grange et al., 2008; Park et al., 2016). Given that many of these CSC markers identify populations with stem-like characteristics but have not yet been shown to be 'true somatic stem cells' with the ability to regenerate tissues, CSCs are instead commonly referred to as tumor-initiating cells (TICs), given their ability to generate tumors upon limiting dilution. Hereafter, CSCs are referred to as TIC populations.

Key studies on ovarian cancer TICs were performed using serial transplantation of patient-derived xenografts or limited dilution assays of human tumor-derived primary cultures. Both of these systems require the use of immunocompromised mice. It is becoming increasingly clear that the inflammation in the tumor microenvironment

(TME) helps to promote TIC formation and maintenance (Shigdar et al., 2014). This is largely due to cytokines such as TGFβ, TNFα, IL-1, and IL-6 secreted by tumor-associated immune cell infiltrates, that help to promote TIC characteristics among tumor cells (Shigdar et al., 2014). It is an important research goal to develop HGSC models that contain a TIC population and reliably generate tumors in immunocompetent mice to better phenocopy the environment seen by TICs *in vivo*.

1.4 Preclinical models of ovarian cancer

Due to the shifts in attention regarding the origins of EOC, researchers have largely focused on modeling ovarian cancer after specific subtypes or origins of disease, leading to a narrow characterization of many preclinical models in relation to their origin and common genomic alterations with HGSC. Commonly studied features include growth rate, tumorigenic potential, immunohistochemical markers, DNA mutations, BRCAness, RNA expression, and copy number variation, with the results correlated to The Cancer Genome Atlas (TCGA) or other large datasets on HGSC. Given our recently improved understanding of TICs and TIC-targeted therapeutics, we have a rich reservoir of human and murine-derived ovarian cancer models that have limited characterization for TIC populations, highlighting an area of focus to improve the utility of current and emerging preclinical models.

1.4.1 Syngeneic murine models

A syngeneic model is operationally defined by its immunological compatibility such that the host does not reject either the outgrowth or transplant of cancer cells in

immunocompetent animals. Syngeneic models are divided into spontaneously occurring and genetically engineered models, as described below.

1.4.2 Spontaneously transformed syngeneic models

The only two non-human animals that are known to spontaneously develop EOC are the egg-laying hen and the jaguar (Table 1-1). Up to 35% of egg-laying hens develop EOC with similar risk factors to humans such as age and ovulation number (Hawkridge, 2014). Hen tumors exhibit serous histology and contain T and B cell infiltration (Bradaric et al., 2013). Immune infiltration increases in late-stage disease and is restricted to the tumor stroma, while intratumoral immune infiltration largely decreases with the stage, indicating that late-stage tumors acquire mechanisms to limit immune trafficking (McNeal et al., 2016). No TIC populations have been characterized in the hen model and given the syngeneic nature and relevance to human HGSC, the hen model could offer a rich resource to study TICs.

Interestingly, 40% of captive jaguars develop ovarian carcinoma with non-synonymous mutations in *BRCA1* (Corner et al., 2015; McLean and Mehta, 2017). The endangered nature of this species prevents its use as an ovarian cancer model, though therapies that enhance survival of patients with *BRCA1*-associated cancers could at some point play a role in the conservation of this species.

The ID8 model was derived from the spontaneous transformation of a primary culture of murine OSE cells from C57BL/6 mice. The ID8 model shares epithelial markers (cytokeratin+, WT1+, inhibin−), growth rates, and expression profiles similar to human HGSC, and is tumorigenic in syngeneic mice (Roby et al., 2000). ID8 cells generate

tumors following orthotopic intrabursal (IB) injection, which then progress and form malignant ascites and disseminated disease (Leinster et al., 2012). The ID8 model has been the most commonly used model based on its established characterization and reliability in forming syngeneic tumors. Peritoneal tumors generated by intraperitoneal (IP) injection of ID8 cells develop a complex microenvironment with fibroblasts, T cells, macrophages, and neo-vasculature (Leinster et al., 2012). ID8 cells have been employed in the development of chemotherapies, epigenetic modifiers, immune checkpoint inhibitor and oncolytic virus studies, as well as dendritic cell and microparticle vaccines (Chiang et al., 2013; Gil et al., 2014; Guo et al., 2014; Nounamo et al., 2017; Turner et al., 2017; Wei et al., 2013). Numerous studies have profiled TIC populations within ID8 cultures and ID8-derived tumors (Gupta et al., 2016; Komorowski et al., 2016; Mo et al., 2015; Wang et al., 2013). The ability of cells to generate spheres in low-attachment plates in so-called 'sphere-forming' culture media is a characteristic of stem cells. Increasing sphere number upon serial passage provides evidence for self-renewal within a putative TIC population. Wang and colleagues (2013) showed that ID8 cells formed robust spheres that were dependent on the expression of PKCι. Mo and colleagues (2015) found that tumor cells within the ascites fluid derived from ID8 xenografts had increased cell-surface expression of GPR78 compared to parental ID8 cultures. These GPR78^{high} cells exhibited TIC features such as enhanced sphere-forming capacity and the ability to generate tumors upon limiting dilution (Mo et al., 2015). Interestingly, ascites fluid added to parental ID8 cultures enhanced GPR78 expression, highlighting the ability of the ascitic microenvironment to promote the generation of TICs (Mo et al., 2015). In another study aiming to elucidate the effects of TICs on treatment resistance and TIC-TME interactions, Gupta and colleagues (2016) showed that CD44+CD24+ TICs isolated from ID8 cell cultures

have enhanced PD-L1 expression. This suggested that TICs help to promote both immune escape and the immunosuppression characteristic of the ovarian cancer TME, given that PD-L1 is the inhibitory ligand for PD1 that is expressed on anti-tumor immune cells.

The relevance of the ID8 model to human HGSC was recently called into question given the poor immunogenicity of ID8 cells; out of their mutational burden of 92 somatic mutations, only 17 are predicted to generate transcribed neoantigens. Upon vaccination with synthetic peptides carrying these 17 mutations, none induced a neoantigen-specific T-cell response, indicating that they likely do not yield MHC presented epitopes (Martin et al., 2016). Thus, the use of modified ID8 cell lines better phenocopy human HGSC (Martin et al., 2016).

One of the notable weaknesses of the ID8 model is that it does not contain a *Trp53* mutation, which is characteristic of 94% of human HGSC (Cole et al., 2016). In addition, ID8 cells do not contain any *BRCA* mutations, limiting their use for studying hereditary HGSC. Walton and colleagues (2016, 2017) generated ID8 cells with both a *Trp53* and *Brca2* mutation using CRISPR-Cas9. ID8-*Trp53*−/−*Brca2mut* tumors were more aggressive than parental ID8 tumors and contained intraepithelial lymphoid aggregates, characteristic of hereditary human HGSC and making this model relevant to the study of *BRCA*-associated HGSC (Kroeger et al., 2016). Interestingly, *BRCA*-associated cancers, including breast and HGSC have a stem-like expression profile (Sau et al., 2016), highlighting the potential of ID8-*Trp53*−/−*Brca2mut* cells for TIC studies.

Roberts and colleagues (2005) have also published a spontaneously transformed murine OSE cell line, MOSE-L cells, which were highly proliferative, expressed epithelial markers, and were tumorigenic in syngeneic C57BL/6 mice, though uptake of this model has been sparse and no TIC population has been characterized, likely because of the well-established characterization of the ID8 model.

Given that the FTE is the origin of the majority of HGSC, Endsley and colleagues (2015) described spontaneously transformed oviductal (murine fallopian tube) epithelial cells derived from CD1 mice that exhibited features of transformation, but only generated subcutaneous tumors in athymic nude mice, preventing their use as a syngeneic model. The addition of PTEN loss in these cells resulted in the first syngeneic model of fallopian tube-derived EOC (Russo et al., 2018), however, no TIC populations were studied.

1.4.3 Genetically engineered mouse models (GEMM)

The majority of GEMM models were generated to improve our understanding of the origin(s) of ovarian cancer. Consequently, most characterizations of these models have placed emphasis on identifying the location of early lesions and assessing positivity in immunohistochemical panels for PAX8, P53, WT1, and cytokeratins, with a lack of inhibin and calretinin staining. With emerging TIC-based therapies requiring good models for optimization, characterization of the majority of GEMM models has been too narrow. Yet, many models may be ideal because of their shared genomic alterations and TME complexity that phenocopy HGSC. The various GEMM models of ovarian cancer have been comprehensively reviewed (Garson et al., 2012; Morin and Weeraratna, 2016), and a subset are discussed below.

Many models have been made using oncogenic simian-virus 40 T-antigen (SV40TAg) driven from the ovarian or oviductal epithelium (Table 1-2). These models include the TgMISIIRTAg model, which drives SV40TAg expression from the *MISIIR (Amhr2)* gene, leading to ovarian tumor development in 50% of mice at 6–13 weeks of age (Connolly et al., 2003). The inducible model, TgCAG-LS-TAg, drives SV40TAg from the chicken β-actin promoter and was used to show that estrogen can accelerate EOC development (Laviolette et al., 2010). Another model used the oviduct-specific gene, *Ovgp1*, to drive SV40TAg expression generating tumors derived from oviductal epithelial cells (Sherman-Baust et al., 2014). Among SV40TAg-driven ovarian cancer models, none have characterized a TIC population.

Given that 94 % of HGSCs possess *TP53* mutations (Cole et al., 2016), novel therapies should be tested in models that represent both high and low p53 expression. Multiple GEMMs have either *Trp53* knockout or *Trp53* mutation, driven from both the ovarian and oviductal epithelium (Flesken-Nikitin et al., 2013, 2003; Perets et al., 2013; Szabova et al., 2012). HGSCs with mutant *TP53* have been suggested to have more TICs due to the role of *TP53* in promoting an epithelial-to-mesenchymal transition (EMT), and the groundbreaking work that revealed EMT promotes stem cell attributes (Mani et al., 2008; Shetzer et al., 2014). A possible role of *TP53* in TIC regulation could be extrapolated from a study by Son and colleagues (2012) who showed that *Trp53* loss enhanced pro-inflammatory cytokine expression including TNFα, which may promote TIC maintenance (Shigdar et al., 2014). More studies are needed to elucidate the effects of specific *TP53* mutations on the ovarian cancer TME and the role of these mutations in regulating TIC populations.

Interestingly, *BRCA1/2* has been shown to regulate mammary stem cell populations (Foulkes, 2004; Sigl et al., 2016; Wright et al., 2008). Given that *BRCA*-associated HGSC exhibits high rates of recurrence, it has been suggested that *BRCA*-associated tumors may have more robust TIC populations underlying these recurrences (Foulkes, 2004). Perets and colleagues (2013) generated GEMMs with doxycycline-inducible Cre-recombinase mediated deletion of *Brca1* or *2* and *Pten*, and *Trp53* loss or mutation, driven from the oviductal epithelium-specific *Pax8* promoter. All combinations yielded HGSC-like tumors with genomic alterations similar to the TCGA dataset on ovarian carcinoma such as c-myc amplification. Similarly, Zhai and colleagues (2017) characterized a model of tamoxifen-inducible deletion of *Brca1*, *Pten*, *Rb1*, and *Nf1* driven from the *Ovgp1* promoter, which generated STICs that progressed to HGSC. They also characterized a similar model with deletion of *Brca1*, *Pten*, and *p53* that also developed precursor lesions and HGSC, but had a mixed tumor phenotype with mucinous metaplasia. These models have numerous features relevant to human disease and characterizing TIC populations would be an exciting addition to extend the utility of these models.

Although GEMM models enable us to better model the origins of disease and the genomic alterations characteristic of HGSC, they have two weaknesses that limit their use for studying TIC biology. Firstly, most GEMMs have been generated on a mixed strain background, preventing the generation of transplantable syngeneic cell lines. Secondly, although GEMMs may reproducibly generate tumors, they tend to arise over a wide course of time. The difficulty in controlling tumor onset and size in GEMMs introduces a logistical challenge for TIC studies that rely on flow cytometric analysis of TIC populations, since flow cytometry is classically performed on all

samples at one time point. This limitation is easily overcome with transplantable syngeneic models, such as the ID8 model, where tumor onset is uniform and controlled.

Table 1-1. The utility of spontaneous and syngeneic models of epithelial ovarian cancer.

Model	Genetic Engineering	Tumor-initiating cell features	Advantages	Limitations	References
Laying Hen	None	- Unknown	- Shared risk factors with human disease - Tumors classified from Stage I–IV similar to HGSC - Ascites develops in later stages II–IV	- Time >2 years for tumor development - Lack of reagents for species	Barua et al., 2009; Bradaric et al., 2013
Jaguar	None	- Unknown	- Shared risk factors and familial BRCA mutations similar to high-risk women	- Endangered species - Lack of reagents for species	Corner et al., 2015; McLean and Mehta, 2017
ID8 (original)	None	- CD44+CD24+ population - GPR78^{high} population within ascites	- Reliable and fast tumorigenesis - Well characterized - Develops ascites	- Lacking mutations common to human HGSC	Martin et al., 2016; Mo et al., 2015; Roby et al., 2000
ID8-Trp53-/-	*Trp53* deletion	- Unknown	- Shared genomic alterations with human HGSC - Complex immune landscape similar to human HGSC	- *Trp53* deletion may not reflect biology of *TP53* mutations seen in human HGSC	Walton et al., 2016, 2017
ID8-Trp53−/− Brca2−/−	*Trp53* and *Brca2* deletion	- Unknown	- Shared genomic alterations with human HGSC - Complex immune landscape similar to human HGSC - CD3+ T cell rich tertiary lymphoid structures form	- *Trp53* deletion may not reflect biology of *TP53* mutations seen in human HGSC	Walton et al., 2016, 2017

High-grade serous ovarian cancer (HGSC).

Table 1-2. The utility of GEMM models of epithelial ovarian cancers.

Model	Genetic Engineering	Tumor-initiating cell features	Advantages	Disadvantages	References
TgMISIIRTAg	SV40TAg driven from reproductive tract-specific MISIIR (*Amhr2*) promoter during development	Unknown	- Forms ascites	- SV40TAg - Slow tumor development (6–13 weeks) - Non-inducible tumorigenesis	Connolly et al., 2003
TgCAG-LS-TAg	SV40TAg with lox-stop cassette driven from ubiquitous CAG promoter *	Unknown	- Ascites develops in a subset of mice - Inducible SV40TAg	- SV40TAg - Slow tumor development—>22 weeks - Surgical administration of Ad-Cre	Laviolette et al., 2010
mogp-TAg	SV40TAg driven from oviduct-specific *Ovgp1* promoter	Unknown	- Oviduct tumor origin	- SV40TAg - Non-inducible tumorigenesis - Slow tumor development (>6 weeks) - Fails to develop ascites	Miyoshi et al., 2002; Sherman-Baust et al., 2014
TgK18-GT121-Brca-Trp53	Inducible SV40TAg and either *Trp53*−/− or *Trp53*mut and *Brca1* or *2* deletions driven from epithelial specific cytokeratin 18 expression *	Unknown	- R172H *Trp53* mutation that phenocopies human R175H *TP53* mutation - Inducible SV40TAg	- SV40TAg - Surgical administration of Ad-Cre	Szabova et al., 2012
Trp53loxP/loxP-Rb1loxP/loxP	Inducible deletion of *Trp53* and *Rb1* *	Unknown	- Inducible gene deletions - Genomic alterations similar to human HGSC	- *Trp53* deletion may not reflect biology of all *TP53* mutations seen in HGSC - Slow tumor development (median survival 227 days)	Flesken-Nikitin et al., 2013, 2003
Pax8-Cre-Brca1(2)−/−; Trp53mut(−/−); Pten −/− *	Doxycycline inducible Cre-mediated deletion of *Brca*, *Pten*, and *Trp53*, driven from oviduct-specific *Pax8* promoter.	Unknown	- Inducible gene deletions from oviduct origin - Genomic alterations similar to human HGSC - Models with both *Trp53* deletion and mutation	- Fails to develop ascites - *Pten* deletion induces endometrial lesions	Perets et al., 2013
Ovgp1-iCre-ERT2 + tumor suppressor genes	Conditional deletion of *Brca1*, *Pten*, *Rb1*, and *Nf1* (BPRN mice) or *Brca1*, *Pten*, and *p53* (BPP mice), driven from the oviduct-specific *Ovgp1* promoter	Unknown	- Inducible gene deletions from oviduct origin - Genomic alterations similar to human HGSC - Models with both Trp53 deletion and mutation	- Ascites only in 12% of mice - BPP mice develop a mixed tumor phenotype with mucinous metaplasia	Zhai et al., 2017

***** Model tissue-specificity governed by the site of administration of adenovirus expressing Cre recombinase (Ad-Cre).

1.4.4 Human-derived and autologous cultures

Numerous ovarian cancer cell lines have been used historically with inconsistencies in their relevance to human HGSC, particularly A2780 and SKOV3 cells, which are unlikely to represent HGSC (reviewed by Domcke et al., 2013). Recently, HGSC primary cultures have been established that have genomic alterations and gene expression profiles consistent with TCGA datasets (Fleury et al., 2015; Ince et al., 2015; Kloudová et al., 2016), offering resources for TIC studies since they have defined subtype origins. The major weakness of using primary cultures is that tumorigenesis can only be studied using xenografts in immunodeficient mice that fail to develop a complex TME, which we have come to appreciate as an important regulator of TIC populations.

In addition, ovarian cancers are rich resources due to the easily accessible ascites fluid that is known to promote TIC development (Mo et al., 2015). Even though the use of human primary cultures have limitations for studying ovarian cancer TICs, they offer invaluable resources to determine the direct effect of TIC-based therapies. Recently, Starbuck and colleagues (2018) profiled human ovarian cancer cell lines and found that CD133+ TICs co-express the Siayl-Thomsen-noveau (STn) antigen. CD133+STn+ TICs displayed enhanced colony and sphere formation. Interestingly, the authors developed anti-STn antibody drug-conjugates that were able to reduce the CD133+STn+ TIC population both *in vitro* and *in vivo*, highlighting a promising therapeutic approach for ovarian cancers containing a CD133+STn+ TIC population (Starbuck et al., 2018).

Additionally, emerging methods have armed oncolytic virotherapies with TIC-targeting agents such as CXCR4 antagonists or the Nodamura virus protein B2 (Bastin et al., 2018; Komorowski et al., 2016).

1.5 Ovarian cancer prevention

Given the high incidence of ovarian cancer, particularly among developed nations (Coburn et al., 2017), along with the difficulty in the screening and effective treatment of HGSC, developing new prevention strategies is of pressing importance to global health. In the search for novel prevention strategies, much can be learnt from our knowledge of HGSC biology and the risk factors for ovarian cancers. Fortunately, our knowledge of ovarian cancer risk factors is robust, and we know that blocking certain risk factors can ameliorate ovarian cancer risk. However, there is much room for improvement, particularly with a global outlook, as issues such as access, genetic risk, family planning, and lifestyle vary greatly by region. In this next section, ovarian cancer risk factors and risk reduction strategies are detailed.

1.5.1 Risk factors for EOC

Ovulation and age are the primary non-hereditary risk factors for ovarian cancer (Auersperg, 2013a; Fathalla, 2013). In 1971, Fathalla proposed the incessant ovulation hypothesis from observations that ovarian cancer incidence correlated with ovulatory patterns, such that the higher number of lifetime ovulations a woman has is directly proportional to her risk of ovarian cancer (Fathalla, 2013). The mechanism behind ovulation-associated risk remains elusive; however, numerous hypotheses have been put forth, including the frequent wound healing of the OSE following ovulatory rupture,

inflammation, and the engraftment of opportunistic fallopian tube lesions at the time of ovulation (Fathalla, 2013; George et al., 2016; Kurman and Shih, 2010; Savant et al., 2018). Similarly, nulliparity increases the risk of ovarian cancer by 24% compared to women with one child, since pregnancy, in effect, reduces ovulation number during gestation (Gaitskell et al., 2018). A greater risk reduction of 6% per child is observed in women with more than one child (Gaitskell et al., 2018). After birth, breastfeeding can also confer a significant reduction of risk, reducing risk by 10% for every 12 months of breastfeeding (Gaitskell et al., 2018). Breastfeeding is thought to reduce risk by delaying ovulation through the hyperprolactinemic state induced by lactation (Chao, 1987).

Ovarian cancer is a disease of aging, with risk increasing most dramatically in women >45 years of age, with the median age at diagnosis being 63 years (National Cancer Institute, 2018). This is curious since ovarian cancer incidence is increasing at a time long after ovulations, the primary non-hereditary risk factor, have ceased at menopause. This produces somewhat of a conundrum that has remained unresolved in this field. A common explanation is that the wound healing process or secreted signaling factors produced during ovulation promote the transformation of a precursor cell into a CSC that sits quiescently until it awakens after menopause; however no models or support for this hypothesis have been produced.

Hereditary mutations in the *BRCA1/2, BRIP1, PALB2, RAD51C, or RAD51D* genes confer a significant increase in HGSC risk (Karnezis et al., 2017). Hereditary mutations in the *BRCA1* or *BRCA2* genes are the most frequently studied, given that they increase the risk

of both breast and ovarian cancer (Rebbeck et al., 2015). Interestingly, the site of mutation in the *BRCA1* gene confers differential risk, with an increased risk of 15-60% for HGSC conferred by mutations in exon 11 (Rebbeck et al., 2015; Weberpals et al., 2008). In the context of sporadic HGSC, *BRCA1* dysfunction is widespread with loss of heterozygosity, hypermethylation, or haploinsufficiency that results in no detectable BRCA1 expression in 66 % of sporadic tumors (Weberpals et al., 2008).

1.5.2 Ovarian cancer risk reduction methods

We currently have multiple strategies for ovarian cancer risk reduction that function by mitigating the risk factors detailed above; however there is much room for improvement as the uptake and feasibility of these methods are not suitable for global risk reduction strategies. RRSO is the most extreme risk reduction strategy that involves the removal of both sites of ovarian cancer origin, the ovary and the fallopian tubes. Even though RRSO confers the most robust reduction of risk (HR: 0.21, Rebbeck et al., 2009), it is only available to women at high risk. RRSO is far too extreme and costly as a global risk reduction strategy since it induces early menopause in young women, thereby increasing the risk of other diseases such as of cardiovascular disease (Arts-de Jong et al., 2014).

Hormonal oral contraceptive (OC) use also greatly reduces risk by approximately 35% following 5-9 years of consistent use (Torre et al., 2018). The mechanism of OC use-associated HGSC risk reduction remains elusive, though it is thought to be due to the negative feedback of estrogen and progesterone on the anterior pituitary that prevents gonadotropin release and effectively blocks ovulation (Cooper and Adigun, 2018). Interestingly, OC use also reduces HGSC risk by ~50% among *BRCA* mutation carriers,

centering ovulation as a driver of HGSC in both sporadic and hereditary cases (Cibula et al., 2011). Unfortunately, uptake of OCs is limited globally due to access, cultural barriers and an increased risk of thrombosis in some women (Brynhildsen, 2014; Grindlay et al., 2013). It further remains to be seen whether OCs increase the risk of breast cancer, a concern among many women that highlights the need to develop novel risk reduction strategies that maintain fertility and do not increase the risk of other pathologies.

Similarly, it is known that increased parity and breastfeeding decrease HGSC risk likely by reducing ovulation number; however, parity has been steadily decreasing in developed countries and is not a feasible method to promote for global risk reduction (Gaitskell et al., 2018; Nargund, 2009).

Interestingly, there is recent evidence that intrauterine devices (IUD) reduce ovarian cancer risk by up to 38% with prolonged use (Huang et al., 2015; Ness et al., 2011). Unfortunately, neither study specified whether hormonal or non-hormonal IUDs were used to generate their findings and no further evidence has emerged to provide any more detail or mechanism.

Tubal ligation reduces HGSC risk by 20% (Sopik et al., 2015). These findings have added support to the hypothesis that retrograde flow towards the ovary could allow for opportunistic STICs to migrate into the ovary and establish HGSC, since tubal ligation blocks such flow (Gaitskell et al., 2016).

Intriguingly, aside from RRSO, the largest documented risk reduction was seen in Taiwanese women with type II diabetes (T2D) who use the antidiabetic drug metformin (Tseng, 2015). T2D women taking metformin had up to an 82% reduction in ovarian cancer incidence, with lower incidence as dose and duration of metformin use increased (Tseng, 2015). However, this risk-reduction seems dependent on the patient cohort since Urpilainen and colleagues (2018) found that metformin did not reduce risk among Finnish T2D women. However, the small sample size of the Finnish T2D cohort compared to the Taiwanese cohort needs to be considered and highlights the need for more studies on metformin use and HGSC risk. Metformin is used by T2D women to maintain proper blood glucose levels since metformin inhibits hepatic gluconeogenesis through both AMPK-dependent and AMPK-independent mechanisms (Rena et al., 2017). The large risk reduction found within the Taiwanese T2D population was suggested to be due to this metabolic function of metformin that may starve cancer cells of their preferred metabolic route of glycolysis (Rena et al., 2017; Tseng, 2015). Given that metformin use does not affect fertility (Bertoldo et al., 2014) and is a well-tolerated FDA-approved drug, it is an attractive method for global HGSC risk reduction if more studies were to offer evidence that metformin may benefit the general non-T2D population. Overall, numerous risk reduction strategies have been identified, yet most have no concrete mechanisms to explain their observed risk reduction.

1.5.3 The ovary as a pro-tumor niche

Regardless of the origin of HGSC, one thing remains consistent: the ovary is a pro-tumor niche. Anecdotal evidence has long suggested that ovarian cancers progress once they establish themselves within the ovarian stroma, and a recent study has shown that the ovary

is necessary for ovarian cancer metastasis into peritoneal cavity (Coffman et al., 2016). Beyond primary ovarian cancers, up to 30% of cancers found in the ovary are later identified to be metastases from other primary malignancies from the breast or colon (Bigorie et al., 2010; Li et al., 2012); however, reasons why the ovary is permissive to tumor growth and metastasis are largely unexplored. Yang-Hartwich and colleagues (2014) identified granulosa cell-secreted SDF-1 as a chemoattractant for ovarian metastasis following intrauterine injection of CD44+MYD88+ ovarian cancer TICs, supporting a TIC based model of ovarian cancer metastasis. However, the levels of SDF-1 were not explored in post-menopausal mice, which may be an important consideration given the age-associated incidence of ovarian cancers.

1.5.4 Ovarian aging

Given that ovulations have largely ceased at the time most women are diagnosed with ovarian cancer (Torre et al., 2018), the effects of ovarian aging must be considered when designing novel prevention strategies. Historically, ovarian aging has been studied primarily in the context of circulating hormone and gonadotropin levels in post-menopausal women (Smith and Xu, 2008), and the effects of these hormones on ovarian cancer initiation. Structural changes in the ovary and fallopian tubes have also been explored, but these studies were carried out prior to recent technical advances and knowledge, yielding no obvious connections to ovarian cancer development (Best et al., 1996; Crow et al., 1994; Focchi et al., 1996; Makabe et al., 1998; Perheentupa and Huhtaniemi, 2009). However, a recent study by Briley and colleagues (2016) provided the first evidence of ovarian stromal fibrosis in aged mice. They showed that aged mice have increased deposition of collagen and enhanced inflammation, particularly through the

recruitment of F4/80+ macrophage giant cells (Briley et al., 2016). This ovarian fibrosis was suggested to reduce fertility with age and no links to ovarian cancer were explored. Recently, Loughran and colleagues (2018) showed that murine aging enhances peritoneal metastasis of ovarian cancer allografts. Metastases in these aged mice had increase tumor-infiltrating lymphocytes, particularly from the B-cell lineage, highlighting a possible immune-mediated mechanism in the age-associated spread of ovarian cancer (Loughran et al., 2018). Curiously, the authors also showed that aging enhances metastasis to the ovary, furthering support for the ovary as a pro-tumor niche, particularly with age (Loughran et al., 2018).

1.6 Project rationale

Given the poor survival and our lack of understanding of HGSC, the development of novel treatment and diagnostic methods requires better models of HGSC that allow for easy manipulation, are transplantable into immunocompetent mice, and have TIC populations similar to HGSC. At the start of this project, a technician in our lab, Olga Collins, noticed that one of our murine OSE primary cultures went rogue and began growing extremely fast, exhibiting morphology and anchorage-independent growth characteristic of cancer cells. ***We first hypothesized that these spontaneously transformed OSE cells (STOSE cells) are a good model of HGSC***. The development of the STOSE model has opened the door to numerous collaborations designed to test novel therapeutics such as immunotherapies, and to optimize novel imaging techniques that aim to improve histological classification of tumor tissue. One such collaboration has led us to ***further hypothesize that deep learning of non-linear optical imaging of STOSE tumors will generate a proof-of-principle dataset for the use of deep learning in ovarian tissue***

classification. Many of the structural changes seen in the tumor stroma such as fibrosis (desmoplasia) are also involved in the development of a pre-metastatic niche in non-cancerous tissue (Cox and Erler, 2014; DeClerck, 2012). With the recent discovery of age-associated stromal fibrosis in murine ovaries (Briley et al., 2016), the exciting potential of using metformin as a global risk reduction strategy, and the widespread use of metformin to treat fibrosis in pre-clinical models of skin, lung, kidney, liver, and heart fibrosis (Choi et al., 2016; Kita et al., 2012; Ursini et al., 2016; M. Wang et al., 2016; Xiao et al., 2010), we ***hypothesized that the ovarian cancer risk factors of age and ovulation promote ovarian fibrosis, thereby creating a tumor-permissive pre-metastatic niche within the ovary, which can be abrogated by metformin use.***

2 CHAPTER 2: THE STOSE MODEL

This paper is published:

McCloskey, C.W., Goldberg, R.L., Carter, L.E., Gamwell, L.F., Al-Hujaily, E.M., Collins, O., Macdonald, E.A., Garson, K., Daneshmand, M., Carmona, E., Vanderhyden, B.C., 2014. A New Spontaneously Transformed Syngeneic Model of High-Grade Serous Ovarian Cancer with a Tumor-Initiating Cell Population. Front. Oncol. 4:53 pp 1-13. https://doi.org/10.3389/fonc.2014.00053

A new spontaneously transformed syngeneic model of high-grade serous ovarian cancer with a tumor-initiating cell population

Curtis W. McCloskey[1,2], Reuben L. Goldberg[1,2], Lauren E. Carter[1,2], Lisa F. Gamwell[1,2], Ensaf M. Al-hujaily[1,2], Olga Collins[1,2], Elizabeth A. Macdonald[1,2], Kenneth Garson[1,2], Manijeh Daneshmand[2,5] Euridice Carmona[3], and Barbara C. Vanderhyden[*,1,2,4].

Affiliations:
[1]Department of Cellular and Molecular Medicine, University of Ottawa, Ottawa, ON, Canada
[2]Centre for Cancer Therapeutics, Ottawa Hospital Research Institute, Ottawa, ON, Canada[3]Centre de recherche du Centre hospitalier de l'Université de Montréal (CRCHUM), Institut du cancer de Montréal, Montréal, QC, Canada
[4]Department of Obstetrics and Gynecology, University of Ottawa, Ottawa, ON, Canada
[5]Department of Pathology and Laboratory Medicine, University of Ottawa, Ottawa, ON, Canada

*Correspondence:
Dr. Barbara Vanderhyden
Centre for Cancer Therapeutics,
Ottawa Hospital Research Institute
501 Smyth Rd, Box 926
Ottawa, ON, K1H 8L6, Canada
bvanderhyden@ohri.ca

Keywords: high-grade serous cancer, stem cell, tumor initiating cell, syngeneic, ovarian cancer, ovarian surface epithelium, mouse model of ovarian cancer

2.1 Author contributions:

Experiments were designed by Dr. Barbara Vanderhyden and me. All surgeries, IHC, microarrays, and cell cultures were performed by me, following the establishment of the STOSE cell line by Olga Collins. Reuben Goldberg performed the western blotting. Lauren Carter validated 3/8 genes by qPCR presented in Figure 2-3 and I completed the validation. Lisa Gamwell and I performed the flow cytometry prior to *in vitro* studies while I performed the flow cytometry for all *in vivo* studies. Ken Garson and I performed the cell cycle analysis. Elizabeth Macdonald helped me perform the IP injections and necropsies. Manijeh Daneshmond performed the pathology assessment and Euridice Carmona did the IPA analysis. Ensaf Al-hujaily and I performed the DNA sequencing of *p53*. I wrote the manuscript with Dr. Barbara Vanderhyden.

2.2 Abstract

Improving screening and treatment options for patients with epithelial ovarian cancer has been a major challenge in cancer research. Development of novel diagnostic and therapeutic approaches, particularly for the most common subtype, high-grade serous ovarian cancer (HGSC), has been hampered by controversies over the origin of the disease and a lack of spontaneous HGSC models to resolve this controversy. Over long-term culture in our laboratory, an ovarian surface epithelial (OSE) cell line spontaneously transformed (STOSE). The objective of this study was to determine if the STOSE cell line is a good model of HGSC. STOSE cells grow faster than early passage parental M0505 cells with a doubling time of 13 h and 48 h, respectively. STOSE cells form colonies in soft agar, an activity for which M0505 cells have negligible capacity. Microarray analysis identified 1755 downregulated genes and 1203 upregulated genes in STOSE compared to M0505 cells, many associated with aberrant Wnt/β-Catenin and Nf-κB signaling. Upregulation of *Ccnd1* and loss of *Cdkn2a* in STOSE tumors is consistent with changes identified in human ovarian cancers by The Cancer Genome Atlas. Intraperitoneal injection of STOSE cells into SCID and syngeneic FVB/N mice produced pan-CK+, WT1+, inhibin- and PAX8+ tumors, a histotype resembling human HGSC. Based on evidence that a SCA1+ stem cell-like population exists in M0505 cells, we examined a subpopulation of SCA1+ cells that is present in STOSE cells. Compared to SCA1- cells, SCA1+ STOSE cells have increased colony-forming capacity and form palpable tumors 8 days faster after intrabursal injection into FVB/N mice. This study has identified the STOSE cells as the first spontaneous murine model of HGSC and provides evidence for the OSE as a possible

origin of HGSC. Furthermore, this model provides a novel opportunity to study how normal stem-like OSE cells may transform into tumor-initiating cells.

2.3 Introduction

Ovarian cancer is the most lethal gynecological malignancy with an estimated incidence of 239,000 cases in 2012, making it the eighth most common cancer in women worldwide (Ferlay et al., 2015). Epithelial ovarian cancer (EOC) is the most common subtype, which is further divided into endometrioid, clear cell, mucinous, low-grade serous and high-grade serous (HGSC). HGSC is the most common and aggressive subtype of EOC, accounting for the majority of new cases (Auersperg, 2013a). With a 5-year survival rate of only 40%, a greater understanding of HGSC is essential to improve patient outcome (Coburn et al., 2017). The high mortality rate is due, at least in part, to a lack of screening methods to detect the disease before it metastasizes within the peritoneal cavity (Foster et al., 2013). The main reason for this inability to detect and diagnose early stage ovarian cancer is a lack of understanding of disease initiation, made even more challenging due to the current debate over the origin of HGSC. HGSC was long thought to arise from the ovarian surface epithelium (OSE) or inclusion cysts derived from them (Auersperg, 2013a; Flesken-Nikitin et al., 2013; Garson et al., 2012), but recent evidence has identified the distal fimbrial epithelium of the fallopian tube as the source for at least a subset of HGSC (Auersperg, 2013a; Jarboe et al., 2008; Lee et al., 2007; Piek et al., 2001).

To establish experimental models for the study of the initiation of EOC, much effort has been dedicated to the genetic modification of cells from an OSE or fimbrial origin, either

in tissue culture or *in vivo*. Attempts to model HGSC have been particularly challenging and have yielded inconsistent results (Garson et al., 2012; Jones and Drapkin, 2013; Lengyel et al., 2014). Transgenic approaches have generally involved targeting specific genes known to be associated with human HGSC. This targeted approach to tumorigenesis may not be fully reflective of human disease for a number of reasons. First, it is unclear, in human disease, whether commonly mutated genes are normally involved in disease initiation and/or progression. In addition, the expression of the designed genetic changes using developmentally regulated promoters may introduce founder effects that are not reflective of human disease (Jones and Drapkin, 2013). Furthermore, it has been shown that murine cells require fewer genetic alterations than human cells to undergo transformation, again making it difficult to draw conclusions on the origin of cancer in humans from transgenic murine models (Hamad, 2002; Rangarajan et al., 2004). For this reason, spontaneous models of EOC would be helpful to better understand the origins of this disease, but these models are rare and limited to the spontaneous development of ovarian cancer in hens (Barua et al., 2009; Stammer et al., 2008). New spontaneous models of HGSC are clearly needed to provide opportunities to determine the molecular basis of ovarian and fallopian tube epithelial transformation.

There is growing evidence to support the contribution of cancer stem cells (CSC) to the initiation and recurrence of cancer. The CSC theory posits that tumors arise from cells with stem-like characteristics and these cells underlie tumor heterogeneity and recurrence (Kulkarni-Datar et al., 2013; Sengupta and Cancelas, 2010; Yi et al., 2013). Stem cells are slowly dividing cells with drug efflux mechanisms that allow them to escape the effects of

chemotherapeutics that commonly target rapidly dividing cells. Another characteristic of a stem cell is the ability to generate multi-lineage progeny. Recurrent cases of HGSC maintain the heterogeneity of the original tumor suggesting that a cell with multi-lineage potential underlies tumorigenesis, instead of a single clone with a survival advantage (Kulkarni-Datar et al., 2013). A cell with all the characteristics of CSCs is still elusive in ovarian cancer but cells with some of these CSC characteristics, identified by their expression of CD44, CD133, CD117, CD24, and ALDH1 (Foster et al., 2013), have been reported. These CSC-like cells are referred to as tumor-initiating cells (TICs) due to their increased tumorigenic capacity. The role and identification of TICs in ovarian cancer is a rapidly growing area of study.

We recently reported the first stem cell marker that identifies a subpopulation of mouse OSE cells with progenitor cell characteristics. A population of cells expressing Stem Cell Antigen 1 (SCA1; aka lymphocyte antigen 6 complex, locus A (LY6A)] is regulated by ovulation-associated factors present in the follicular fluid and possesses a number of features of stem cells, including slow growth and capacity for self-renewal (Gamwell et al., 2012). After several years of establishing and growing cultures of mouse OSE cells, one cell line that was grown for a prolonged period appeared to spontaneously transform. The following body of work describes the characterization of this spontaneously transformed OSE (STOSE) cell line, demonstrating that it reliably forms syngeneic HGSC tumors. Testing of the SCA1+ cells in the parental and transformed cell lines enabled us to compare the characteristics of these stem cell-like populations, as well as determine the relative malignant potential of SCA1+ vs. SCA1- STOSE cells.

2.4 Material and methods

2.4.1 Experimental animals

Severe combined immunodeficient (SCID) and FVB/N mice were obtained from The Jackson Laboratory and housed with a 12 h light: 12 h dark photoperiod. The animals had free access to food and water and experiments were done in accordance with the Canadian Council on Animal Care's *Guidelines for the Care and Use of Animals*. Protocols were approved by the University of Ottawa Animal Care Committee.

2.4.2 Mouse OSE cell isolation and culture

The M0505 OSE cell line was isolated and established in 2005 according to the protocol described in Gamwell et al. (2012). Upon long-term passage of the cells in adherent cultures on tissue culture plates (Beckton Dickinson) using MOSE media (Gamwell et al., 2012), the M0505 cell line spontaneously transformed and were from that point on labeled STOSE cells, which were also maintained in MOSE medium. The M1107 OSE cell line was established and maintained using the same methods as the M0505 cell line and is used as an independent control for mouse OSE cells.

2.4.3 Proliferation assay

M0505 and STOSE cell proliferation was assessed from 1-3 days after seeding $2x10^4$ cells in 24-well tissue culture dishes (Beckton Dickinson) in MOSE medium. The number of viable cells was determined using the Vi-CELL XR Cell Viability Analyzer (Beckman Coulter).

2.4.4 Chromosomal analysis

G-band karyotyping of 5-metaphase spreads each of M0505 and STOSE cells was carried out by the Cytogenomics and Genome Resource Facility at SickKids Hospital, Toronto, ON, Canada. Briefly, cells were harvested and colcemid (10 µg/mL) was added for 30 min and incubated at 37 ^{o}C. Cells were washed, trypsinized and a single-cell suspension was made. Following washing, a 0.075 M KCl hypotonic solution was added for 15min and incubated at 37 ^{o}C, and banding patterns were visualized.

2.4.5 Cell cycle analysis

The percentages of cells in G1/G0, S-phase, and G2/M phases as well as the percentage of apoptotic cells were determined for M0505 and STOSE cell lines using flow cytometry. Cells were trypsinized (0.05% Trypsin/0.53 mM EDTA, Corning Cellgro), washed in phosphate-buffered saline (PBS) and $1x10^{6}$ cells from three independent isolations of each cell line were resuspended in 300 µL of cold PBS. Cells were fixed in 70% ethanol for 2 h, washed and resuspended in 250 µL of PBS and 5 µL of RNAseA (Sigma Aldrich) for 1 h. The cell suspension was then incubated for 30 min with 10 µL of propidium iodide (Sigma Aldrich) and the cell cycle was assessed by flow cytometry using a Beckman Coulter Epics XL and analyzed by ModFit LT software (Verity Software Inc.). Cell doublets were identified using fluorescence pulse height versus area measurements and excluded from cell cycle analysis.

2.4.6 Microarray analysis

RNA was extracted from M0505 and STOSE cells (n=3) using RNAeasy Mini Kit (Qiagen) and cDNA was made using the OneStep RT-PCR kit (Qiagen). Whole genome expression

was determined using Affymetrix GeneChip Mouse Gene 1.0 ST arrays. Genes were annotated using T4-MEV software (Dana Farber Cancer Institute, Boston) and linear fold change was determined from robust multi-array average (RMA) normalized expression values. Ingenuity Pathway Analysis software (Ingenuity Systems, Qiagen) was used to determine functionally relevant clusters of differential gene expression. Microarray data are publically accessible from the GEO database at record GSE54633.

2.4.7 Quantitative RT-PCR

RNA was extracted using the RNAeasy Mini Kit (Qiagen) and cDNA was made using the OneStep RT-PCR kit (Qiagen). Quantitative-PCR was then performed on an ABI 7500 FAST qRT-PCR machine (Applied Biosystems) using the Taqman Gene Expression assay (Life Technologies) and SsoFast Gene Expression Assay (Bio-rad). Probe (2.5 nmol) and primer (5 nmol) sequences are listed in Table 2-1. The level of *Tbp* was used as an endogenous control in the Taqman assay and *Ppia* was used as an endogenous control in the SsoFast assay.

Table 2-1. Quantitative RT-PCR probe and primer sequences.

Gene	Assay	Probe/primer sequence
Cdkn2a	Taqman	Probe: 5′-/56-FAM/AGCAGAGCT/ZEN/AAATCCGG CCTCAG/3IABkFQ/-3′ Primers: forward, 5′-GCTTCAATCTGTTCCTGGCA-3′, reverse, 5′-CAACAACTTCCTCTCCTGCTAC-3′
Sfrp1	SsoFast	Primers: forward, 5′-CAGTTGTGGCTTTTGCATTG-3′, reverse, 5′-GAGGGAAGGGAGAGGGTTC-3′
Frzb	SsoFast	Primers: forward, 5′-GGACGGAGCGGATTTTCCTAT-3′, reverse, 5′-TGACAGGCTTACATTTGCAACG-3′
Sfrp4	SsoFast	Primers: forward, 5′-TGGAGAGATCAACTCAGTAGA AGG-3′, reverse, 5′-GGCTGGCTATCTGCTTCTTG-3′
Ccnd1	Taqman	Probe: 5′-/56-FAM/ATCAAGTGT/ZEN/GACCCGGA CTGCC/3IABkFQ/-3′ Primers: forward, 5′-CGCTAGAAGTGAAGCTAAG AAGA-3′, reverse, 5′-CTTTGTGTACCGCTGGGAA-3′
Ikbkε	SsoFast	Primers: forward, 5′-GGGAGAGTCTTTGCCTGATTC-3′, reverse, 5′-ATCTCCTGGGCTTGGCTATC-3′
S100a4	SsoFast	Primers: forward, 5′-GGAGCTGCCTAGCTTCCTG-3′, reverse, 5′-TCCTGGAAGTCAACTTCATTGTC-3′
Spp1	SsoFast	Primers: forward, 5′-GGAGGAAACCAGCCAAGG-3′, reverse, 5′-TGCCAGAATCAGTCACTTTCAC-3′
Ppia	SsoFast	Primers: forward, 5′-AGGGTGGTGACTTTACACGC-3′, reverse, 5′-GATGCCAGGACCTGTATGCT-3′
Tbp	Taqman	Probe: 5′-/56-FAM/ACTTGACCT/ZEN/AAAGACCATTGC ACTTCGT/3IABkFQ/-3′ Primers: forward, 5′-CCAGAACTGAAAATCAACG CAG-3′, reverse, 5′-TGTATCTACCGTGAATCTTGGC-3′

2.4.8 Intraperitoneal (IP) and intrabursal (IB) injections of STOSE cells

M0505 and STOSE cells were released from adherent cultures using trypsin (0.05% Trypsin/0.53 mM EDTA), washed with PBS, and resuspended in PBS. 1 x 10^7 M0505 cells in 500 µL of PBS were injected into the peritoneal cavity of FVB/N mice. 1 x 10^7 STOSE cells in 500 µL of PBS were injected into the peritoneal cavity of both SCID and FVB/N mice using a 25-gauge needle (Beckton Dickinson). Disease progression was monitored until humane endpoint was reached, which included 15% weight gain and/or abdominal distension. Necropsies were performed at endpoint and tumors were fixed in 10% buffered formalin for 24 h and then paraffin embedded and sectioned at 5 µm for immunohistochemical analysis.

To perform intrabursal injections of STOSE cells, FVB/N mice were anesthetized using 3% isoflurane gas and 1% oxygen**.** A dorsal incision was made and ovaries were externalized. STOSE cells (4 x 10^4) were resuspended in 2 µL of PBS and injected under the bursal membrane using a 33-gauge needle and dispensing repeater (Hamilton). Tumor initiation was monitored every 2 days by palpation of the ovaries by someone blinded to the experimental groups. Disease progression was monitored until humane endpoint was reached, at which point tumors were fixed, embedded in paraffin blocks and 5 µm sections were made for immunohistochemistry.

2.4.9 Immunohistochemistry

Assessment of the histopathology of IP and IB STOSE tumors was performed by staining sections with hematoxylin and eosin and by immunohistochemical analysis. Following

deparaffinization in xylenes and rehydration in an ethanol gradient, antigen unmasking (Antigen unmasking solution, Dako) was performed, followed by blocking endogenous peroxidase activity using 3% hydrogen peroxide in dH_2O. Sections were then rinsed in PBS. Immunostaining for mouse pan-cytokeratin (pan-CK; pre-diluted, Abcam), mouse WT1 (1:100, Dako), and mouse inhibin (1:100, Dako) was performed according to the mouse-on-mouse kit (Vector). Immunostaining for rabbit PAX8 (1:400, Santa Cruz Biotechnology) was done by incubating sections with the PAX8 antibody overnight at 4 ^{o}C, followed by anti-rabbit horseradish peroxidase-labeled polymer (Dako) for 30min at room temperature. All sections were counterstained using hematoxylin and developed using diaminobenzidine. Following dehydration in an ethanol gradient, sections were mounted using Permount (Fischer Scientific). Images were acquired using the ScanScope CS2 (Aperio).

2.4.10 DNA sequencing

Genomic DNA was extracted from STOSE cells using QIAamp DNA Blood Mini Kit (QIAGEN) and PCR amplified using custom primers designed to cover each of the 11 exons in the mouse p53 gene. Following electrophoresis on a 1% agarose gel, bands pertaining to each exon were individually excised under UV light. DNA was extracted from the agarose gel pieces using the QIAquick Gel Extraction Kit (QIAGEN). Extracted DNA was then diluted to a concentration of 1 ng/μL and mixed with the appropriate custom primer (2 μM) mapping to each exon. Individual exons were sequenced using the 3730 DNA analyzer (Applied Biosystems). Sequences were aligned using the DNA Dynamo program (BlueTractorSoftware).

2.4.11 Flow cytometry for SCA1 expression

M0505 and STOSE cells were trypsinized and a single-cell suspension was made using a 40 μm cell strainer. Cells were resuspended in a flow buffer (4% fetal calf serum in 1X PBS) and incubated with anti-SCA1 allophycocyanin fluorophore conjugated antibody (Miltenyi Biotech) for 15 min at 4 ^{o}C. Following washing and resuspension in flow buffer, cells were sorted for SCA1 expression using the MoFlo cell sorter (Beckman Coulter).

2.4.12 Colony formation in soft agar

Cells were released from adherent cultures using trypsin, washed with PBS and a single cell suspension was achieved by passing cells through a 40 μm cell strainer. A base layer 1:1 mix of 2x Ham's F-12 (Sigma Aldrich):MOSE medium and Ultrapure LMP Agarose (Life Technologies) was solidified at 4 ^{o}C for 30 min and then warmed to 37 ^{o}C prior to the addition of the top layer. The top layer consisting of a 1:1:1 mix of $2.5x10^4$ cells from single cell suspension, 2x Ham's F-12:MOSE medium, and Ultrapure LMP agarose was added. The top layer was solidified at 4^{o}C for 30min and then incubated at 37 ^{o}C for 7 days. Colonies were visualized using the EVOS XL imaging system (Life Technologies) and counted using ImageJ software.

2.4.13 Western blot analysis

Protein was extracted from M0505 and STOSE cells using M-PER Mammalian Protein Extraction Reagent (GE Healthcare). Tumor tissue from SCA1+ and SCA1- tumors was homogenized and protein was extracted using M-PER Mammalian Protein Extraction Reagent. Protein extracts were run on a precast Nupage 4-12% Bis-Tris gradient gel (Life Technologies) and transferred to a nitrocellulose membrane. Following 1 hour blocking in

5% non-fat milk, membranes were incubated with mouse monoclonal PAX8 (1:500, Santa Cruz Biotechnology) or mouse monoclonal P53 (1:1000, Cell Signaling) overnight at 4 ^{o}C. Following washing, the membranes were incubated with rabbit anti-mouse IgG- HRP (1:5000, Abcam) for 1 h and developed using Select^{TM} Western Blotting Detection Reagent (GE Healthcare). The same protocol was used for β-ACTIN using mouse monoclonal anti-β-ACTIN (1:40000, Sigma Aldrich) and rabbit anti-mouse IgG-HRP (1:15000, Abcam).

2.4.14 Statistical analysis

All experiments were performed at least three times. A student t-test was used to determine significant differences between two experimental conditions. Analysis of variance (ANOVA) with Tukey's posttest was used to identify significant differences between more than two experimental groups. Statistical significance was assumed at $p<0.05$.

2.5 Results

2.5.1 Characterization of M0505 and STOSE cell lines

Early passage M0505 cells grow slowly, having a doubling time of 48 hours. The growth rate increases as M0505 cells reach >35 passages and cells begin to lose the epithelial 'cobblestone' morphology that is characteristic of early passage M0505 cells (data not shown), and has been reported by others studying spontaneous transformation of epithelial cells (Padilla-Nash et al., 2013). Continual passage of late passage M0505 cells led to the establishment of the spontaneously transformed OSE (STOSE) cell line. STOSE cells have lost the epithelial 'cobblestone' morphology and have transitioned to a more mesenchymal morphology (Fig. 2-1A). To determine the malignant potential of STOSE cells *in vitro*,

STOSE cells were assessed for colony forming efficiency in soft agar, a measure of anchorage independent growth that is characteristic of transformed cells (Hanahan and Weinberg, 2011). STOSE cells formed colonies while early passage M0505 cells did not (Fig. 2-1B). Another characteristic of transformed cells is rapid growth (Hanahan and Weinberg, 2011). STOSE cells have a doubling time of 13 hours, almost four times faster than their untransformed M0505 counterpart. The growth rate of STOSE cells in comparison to early passage (passage 18-20) M0505 cells over 72 hours is shown in Fig. 2-1C. Since a greatly increased growth rate might be explained by aberrant cell cycle regulation, cell cycle analysis was used to determine if there were differences in the percentage of M0505 and STOSE cells in each phase of the cell cycle. Cell cycle analysis of the M0505 cells (monomers) revealed a large G1 peak (59.6±1.0%), a minor S-phase population (10.1±0.3%) and a surprisingly prominent, putative G2/M peak (28.8±0.8%) (Fig. 2-1D). Interestingly, the presence of a small percentage (1.5%) of hyperploid cells was detected in the analysis by the Modfit program. The presence of a small population of cells with abnormal DNA content was then confirmed by karyotype analysis that identified near-tetraploid M0505 cells (Fig. 2-2B). In addition, the small number of diploid cells in S phase was consistent with the observed slow proliferation of this cell line. In contrast, STOSE cells have a significantly increased proportion of cells in S-phase (45.2±0.7%) and, a reduced proportion in the G1 phase (46.7±0.7%). The small G2/M population and greatly increased S-phase population suggests that STOSE cell cycle checkpoints may be compromised which could lead to the observed acceleration in the rate of proliferation.

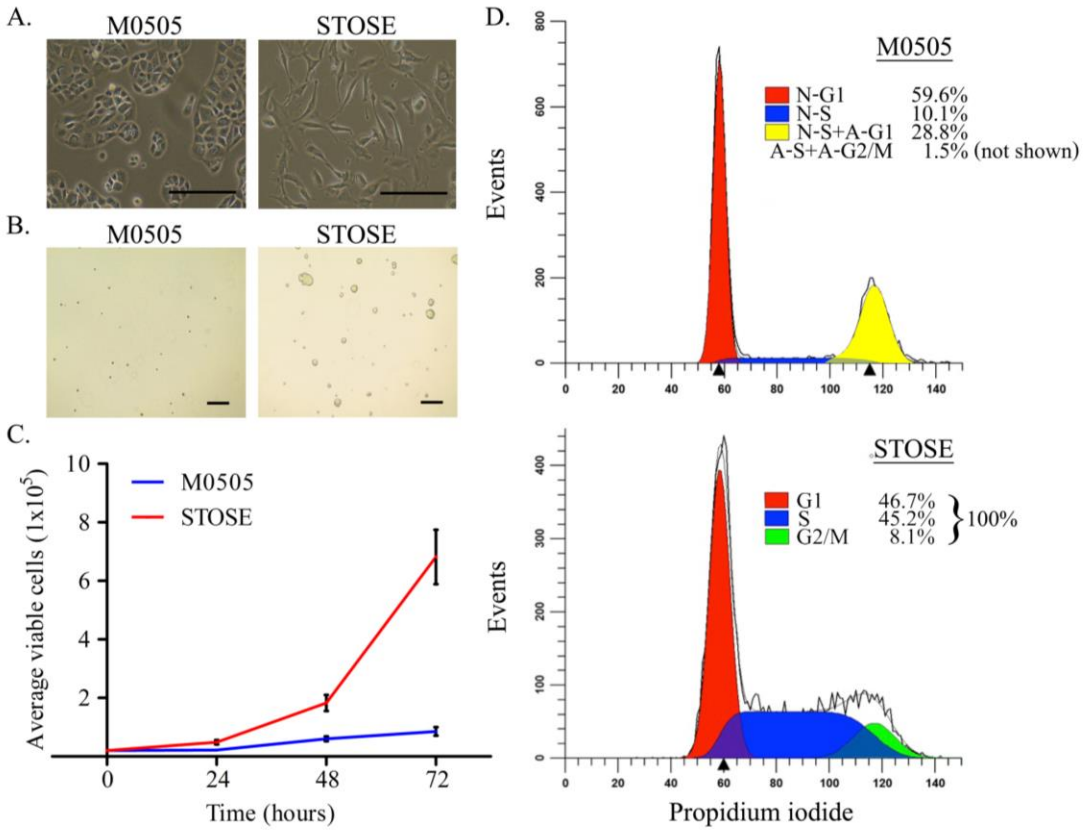

Figure 2-1. STOSE cells exhibit classic characteristics of transformed cells. (**A**) Bright-field microscopy of M0505 and STOSE cells. Scale bar = 200 µm. (**B**) Colony forming assay in soft agar comparing M0505 and STOSE cells. Colonies were visualized after 7 days using bright-field microscopy. Scale bar = 200 µm. (**C**) Growth curve of M0505 and STOSE cells over 3 days. Error bars represent standard error of the mean (SEM). $p<0.001$, two-way analysis of variance. (**D**) Cell cycle analysis of M0505 and STOSE cells. Cells were incubated with the fluorescent dye propidium iodide and analyzed by flow cytometry. The average percentage of cells in G1, S, and G2/M for STOSE cells and M0505 cells is shown (n=6).

Due to the role of aneuploidy in transformation and cancer, and the abnormalities found in the cell cycle analysis, chromosomal analysis was performed on M0505 and STOSE cells to determine if aneuploidy is present. G-band karyotyping of five metaphase spreads revealed aneuploidy in both M0505 and STOSE cell lines; two representative karyotypes are shown for each cell line (Fig. 2-2). STOSE cells have a high degree of aneuploidy with the majority of the population near-triploid (Fig. 2-2C) and a smaller polyploid population (Fig. 2-2D). All STOSE cells analyzed have an addition at the terminal end of chromosome 4. All near-triploid cases have a loss of chromosome 3, 5, and 8, and all polyploid cases are also hypoploid for chromosomes 3, 5, and 8 (Fig. 2-2C,D). Surprisingly, chromosomal analysis of early passage (passage 15) M0505 cells also revealed some degree of aneuploidy with 2/5 near-tetraploid M0505 cells (Fig. 2-2B), while 3/5 M0505 cells were near-diploid (Fig. 2-2A). This presence of a near-tetraploid subset of M0505 cells is in agreement with the presence of M0505 cells with increased DNA content seen in the cell cycle analysis (Fig. 2-1D). All M0505 cells analyzed have terminal deletions in chromosomes 1 and 4. All near-diploid cases have a loss of one chromosome 3, 8, and 12, and all near-tetraploid M0505 cells are hypoploid for chromosomes 3, 8, and 12 (Fig. 2-2A,B).

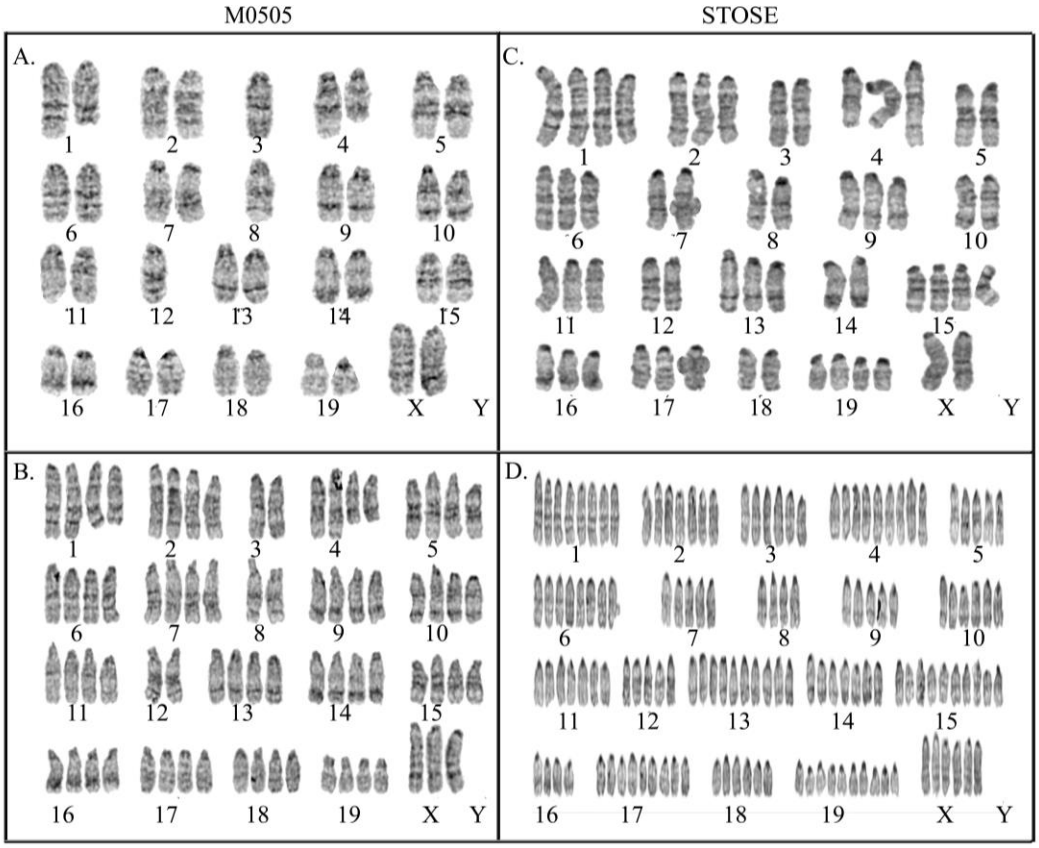

Figure 2-2. Chromosomal analysis of M0505 and STOSE cell lines. G-band karyotyping of five metaphase spreads was performed for both M0505 and STOSE cell lines and representative karyotypes are presented. (**A**) Near-diploid M0505 cell with 37 chromosomes. (**B**) Near-tetraploid M0505 cell with 75 chromosomes. (**A,B**) Terminal deletion of chromosomes 1 and 4 as well as loss of a chromosome 3, 8, and 12 was evident in all M0505 cells analyzed. (**C**) Near-triploid STOSE cell with 54 chromosomes. (**D**) Polyploid STOSE cell with 143 chromosomes. (**C,D**) An addition at the terminal end of chromosome 4 as well as a loss of chromosome 3, 5, and 8 was evident in all STOSE cells analyzed.

2.5.2 Microarray analysis of STOSE cells

To determine the molecular mechanisms by which M0505 cells transformed into the STOSE cells, whole genome microarray analysis was performed on M0505 and STOSE cells and linear fold changes were calculated for STOSE cells relative to M0505 cells. The top 10 up- and down-regulated genes in STOSE compared to M0505 cells are presented in Table 2-2. Interestingly, *Ddr2*, *Ereg*, *Glipr1*, *Calcr*, and *Ankrd1*, all upregulated in STOSE cells, have been shown to be upregulated in primary tumors and ovarian cancer cells (Amsterdam, 2011; Quinn et al., 2009; Scurr et al., 2008; Zhao et al., 2011). *Igfbp4* has been shown to be downregulated in primary tumors (Deng et al., 2012; Walker et al., 2007). The other upregulated genes in STOSE cells: *Serpinb2*, *Epb41l4a*, *Aif1l*, and *Mgll* have no known links to ovarian cancer. Five of the 10 most downregulated genes, *Aldh1a2*, *Enpp2*, *Lgfbp5*, *Thbd*, and *Uchl1*, have been previously implicated in ovarian cancer (Auersperg, 2013b; L.-M. Chen et al., 2013; Nakamura et al., 2012; Okochi-Takada et al., 2006; Rho et al., 2008; Urzúa et al., 2006; Vidot et al., 2010; Walker et al., 2007; Wang et al., 2006). The remaining genes among these downregulated candidates have no previous association with ovarian cancer: *Gpr64*, *Gpr126*, *Cybrd1*, *Star*, *Ncf2*. In accord with the more rapid proliferation of STOSE cells, two negative regulators of Cdk4, *Cdkn2b* and *Cdkn2a*, are downregulated in STOSE cells 13.4 and 5.8-fold, respectively, and both *Ccna2* and *Ccnd1* are up-regulated (2.02 and 6.2-fold).

Table 2-2. Differential gene expression in STOSE cells as compared to early passage M0505 cells

Gene symbol	Gene name	Linear fold change	Publications relating these genes to ovarian cancer
Serpinb2	serine (or cysteine) peptidase inhibitor, clade B, member 2	90.7	unknown
Epb4.1l4a	erythrocyte protein band 4.1-like 4a	64.7	unknown
Ddr2	discoidin domain receptor family, member 2	46.4	Zhao et al., 2011
Aif1l	allograft inflammatory factor 1-like	37.8	unknown
Ereg	epiregulin	35.1	Amsterdam, 2011
Glipr1	GLI pathogenesis-related 1 (glioma)	34.6	Quinn et al., 2009
Igfbp4	insulin-like growth factor binding protein 4	33.6	Walker et al., 2007
Calcrl	calcitonin receptor-like	33.1	Deng et al., 2012
Ankrd1	ankyrin repeat domain 1 (cardiac muscle)	30.4	Scurr et al., 2008
Mgll	monoglyceride lipase	29.8	unknown
Ncf2	neutrophil cytosolic factor 2	-61.7	unknown
Star	steroidogenic acute regulatory protein	-62.7	unknown
Uchl1	ubiquitin carboxy-terminal hydrolase L1	-70.5	Okochi-Takada et al., 2006; Urzúa et al., 2006
Thbd	thrombomodulin	-76.2	L.-M. Chen et al., 2013
Cybrd1	cytochrome b reductase 1	-83.0	unknown
Igfbp5	insulin-like growth factor binding protein 5	-96.1	Rho et al., 2008; Urzúa et al., 2006; Walker et al., 2007; Wang et al., 2006
Gpr126	G protein-coupled receptor 126	-96.6	unknown
Gpr64	G protein-coupled receptor 64	-101.3	unknown
Enpp2	ectonucleotide pyrophosphatase/phosphodiesterase 2	-147.3	Nakamura et al., 2012; Vidot et al., 2010
Aldh1a2	aldehyde dehydrogenase family 1, subfamily A2	-170.6	Auersperg, 2013b

The Cancer Genome Atlas (TCGA) ovarian carcinoma array is a whole genome array database with analysis of 570 human HGSC tumors. The TCGA array dataset was analyzed by the Cancer Genome Research Analysis Network and two of the top genes changes in the STOSE cell microarray were among those reported in the pathways most frequently altered in ovarian carcinomas (Bell et al., 2011): downregulation of *Cdkn2a* (-5.8) and overexpression of *Ccnd1* (+6.2). Overexpression of *Ccnd1* is strongly correlated to decreased progression free survival (Hashimoto et al., 2011) and loss of *Cdkn2a* through mutation or hypermethylation has also been shown in human ovarian carcinomas (Bell et al., 2011; Birch et al., 2011; Hunter et al., 2012; Ozdemir et al., 2012). Ingenuity pathway analysis (IPA) was used to identify functionally related clusters of gene expression differences from the microarray data. IPA analysis revealed possible aberrant Wnt/β-Catenin and Nf-κB signaling in STOSE cells. The expression of multiple genes associated with Wnt signaling are significantly altered including *Cdkn2a* and downregulation of Wnt signaling inhibitors *Sfrp1* and *Frzb*. Genes differentially expressed in the Nf-κB pathway include *Spp1*, *S100a4*, *IkBkε*, and *Ccnd1*. Interestingly, *Ccdn1* is associated with both Wnt/β-Catenin and Nf-κB signaling. Validation of *Cdkn2a* and *Ccnd1*, as well as Wnt/β-Catenin and Nf-κB related genes were performed by quantitative RT-PCR on three microarray-independent samples of M0505 and STOSE cells (Fig. 2-3).

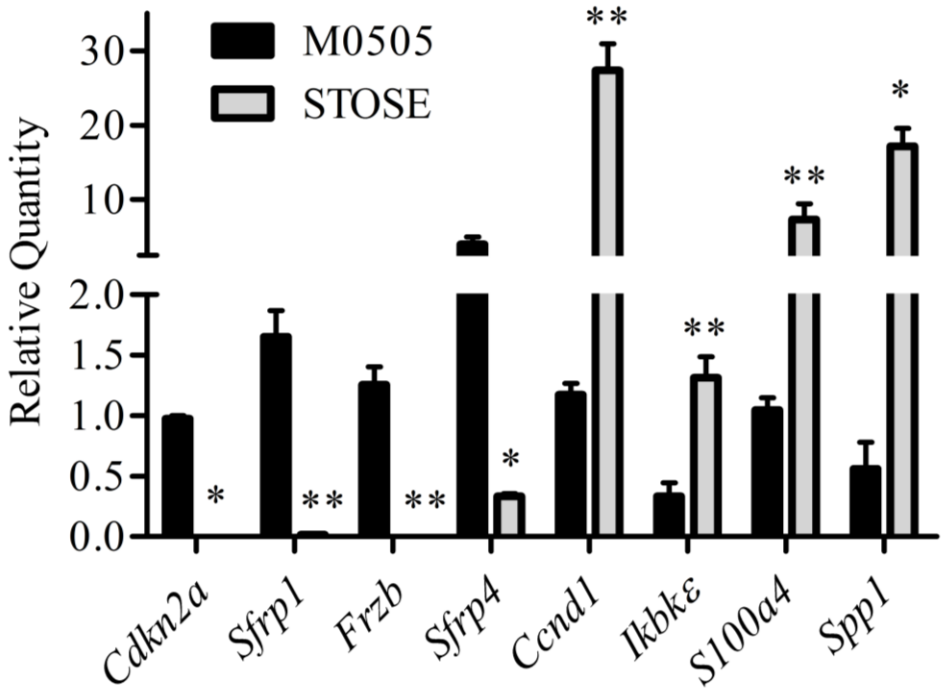

Figure 2-3. Validation of genes differentially expressed in STOSE cells related to Wnt/β-Catenin and Nf-κB signaling or in common with TCGA ovarian carcinoma arrays. Quantitative RT-PCR analysis for *Cdkn2a, Sfrp1, Frzb, Sfrp4, Ccnd1, Ikbkε, S100a4, and Spp1* expression is presented for M0505 and STOSE cells (n=3). Samples used for validation are independent of those used for microarray analysis. Error bars represent SEM and *p<0.05, **p<0.01 by student's t-test.

2.5.3 STOSE cells produce HGSC tumors in both SCID and syngeneic FVB/N mice

Given that STOSE cells exhibit transformed characteristics *in vitro*, their *in vivo* tumorigenicity was assessed using immunocompromised SCID mice and the syngeneic strain of mice, FBV/N. When STOSE cells ($1x10^7$) were injected IP into 4 SCID mice, tumors formed in all mice (4/4) with a median endpoint of 47 days. Tumors were collected from most organs within the peritoneal cavity and the average total tumor burden was 2.22 ± 0.21 g per mouse. All SCID mice had ascites with an average volume of 5.25 ± 0.63 mL. Following IP injection of STOSE cells into immunocompetent syngeneic hosts, STOSE cells were tumorigenic in all FVB/N mice (4/4) with a median endpoint of 48 days. Necropsy revealed tumors throughout the peritoneal cavity and an average total tumor burden of 3.06 ± 0.21 g per mouse, not different from the tumors in SCID mice. All STOSE injected FVB/N mice had ascites with an average volume of 3.08 ± 0.92 mL, also not significantly different from SCID mice (n = 4, p=0.98). Intraperitoneal injection of $1x10^7$ M0505 cells into FVB/N mice did not result in tumor formation in 107 days (0/6 mice).

STOSE-derived tumors from both SCID and FVB/N mice were analyzed by hematoxylin and eosin staining for morphological classification (Fig. 2-4A) and immunohistochemistry for expression of markers commonly found in human ovarian cancers (Fig. 2-4B). Tumor morphology was mixed including regions of mucinous, undifferentiated, and papillary serous structures. The most common morphologies are presented in Figure 2-4A. To confirm an epithelial origin, tumors were stained for epithelial cytokeratins using a pan-CK antibody. Both SCID and FVB/N tumors have strong positive pan-CK staining. Wilms tumor-1 (WT1) positivity is a hallmark of HGSC (Soslow, 2008), and all STOSE tumors

stained strongly for WT1. Given the WT1 positivity, the tumors were examined for expression of another marker of HGSC, PAX8. All STOSE tumors had strong PAX8 expression. To exclude a granulosa cell origin of STOSE tumors, the expression of the granulosa cell marker inhibin was determined. No tumors expressed inhibin. Thus, STOSE derived tumors have a pan-CK+, WT1+, inhibin-, PAX8+ profile, indicating that the STOSE tumors resemble HGSC. Since almost 100% of HGSC cases present with p53 mutations (Jones and Drapkin, 2013), DNA sequencing was performed on all 11 exons of the p53 gene in STOSE cells and no mutations were found (data not shown).

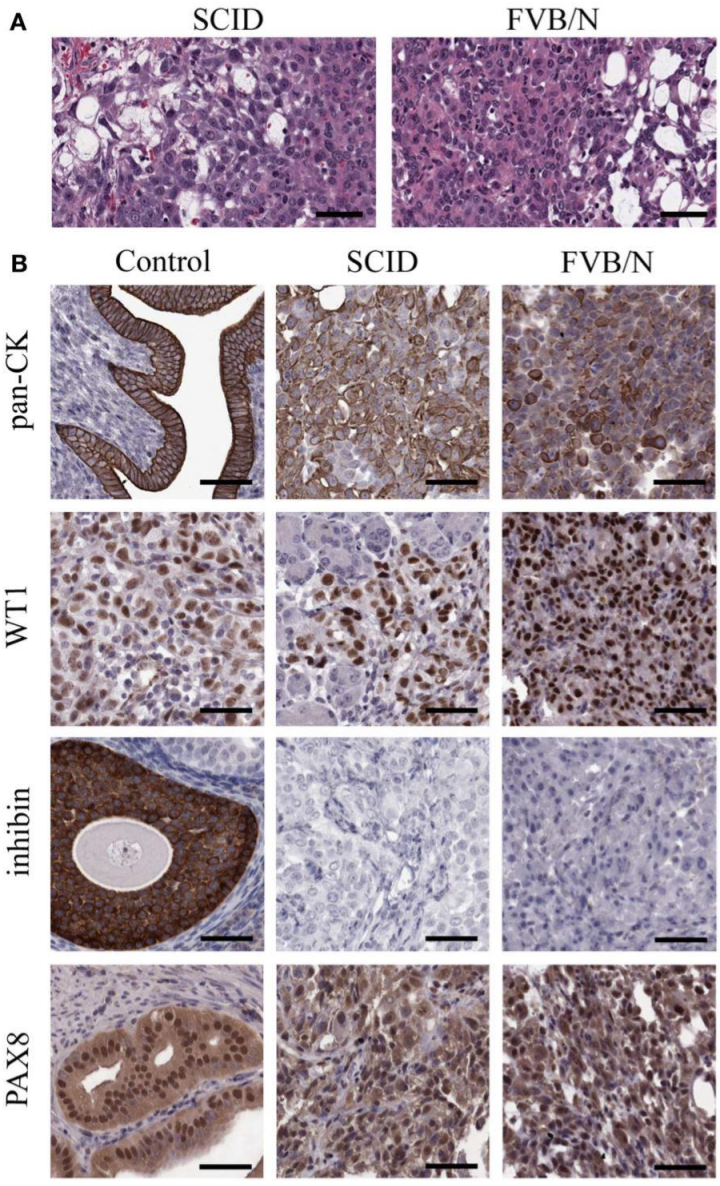

Figure 2-4. STOSE produce high-grade serous epithelial tumors in both SCID and syngeneic FVB/N mice. Tumors were fixed in formalin and set in paraffin blocks; 5 µm sections were used for immunohistochemistry on SCID and FVB/N STOSE cell-derived tumors. (**A**) Hematoxylin and eosin staining of STOSE-cell derived tumors. (**B**) Detection of the epithelial tumor marker, cytokeratin is presented with uterus as a positive control. Wilms tumor-1 (WT1) is a marker of HGSC and is shown with a human high-grade serous ovarian carcinoma as a control. Detection of the granulosa cell and sex-cord stromal tumor marker, inhibin, is shown with granulosa cells as a positive control. PAX8 expression is shown with a fallopian tube (oviduct) positive control. Scale bars = 50 µm.

2.5.4 STOSE cells retained a population of SCA1+ cells that exhibit greater malignant potential

We have recently identified SCA1 as a marker of a defined stem-like population in the OSE (Gamwell et al., 2012). Flow cytometry confirmed that the parental M0505 cell line contains an average SCA1+ population of 14.5 ± 1.4% (n=6). Interestingly, STOSE cells have retained a smaller SCA1+ population, on average 5.8 ± 0.8% (n=11, Fig. 2-5A). To determine if SCA1+ and SCA1- cells exhibit a difference in malignant potential *in vitro*, M0505 and STOSE cells were sorted for SCA1 expression and assayed for colony forming efficiency in soft agar. Sca1+ STOSE cells formed significantly more colonies than Sca1- STOSE cells ($p<0.05$, Fig. 2-5B).

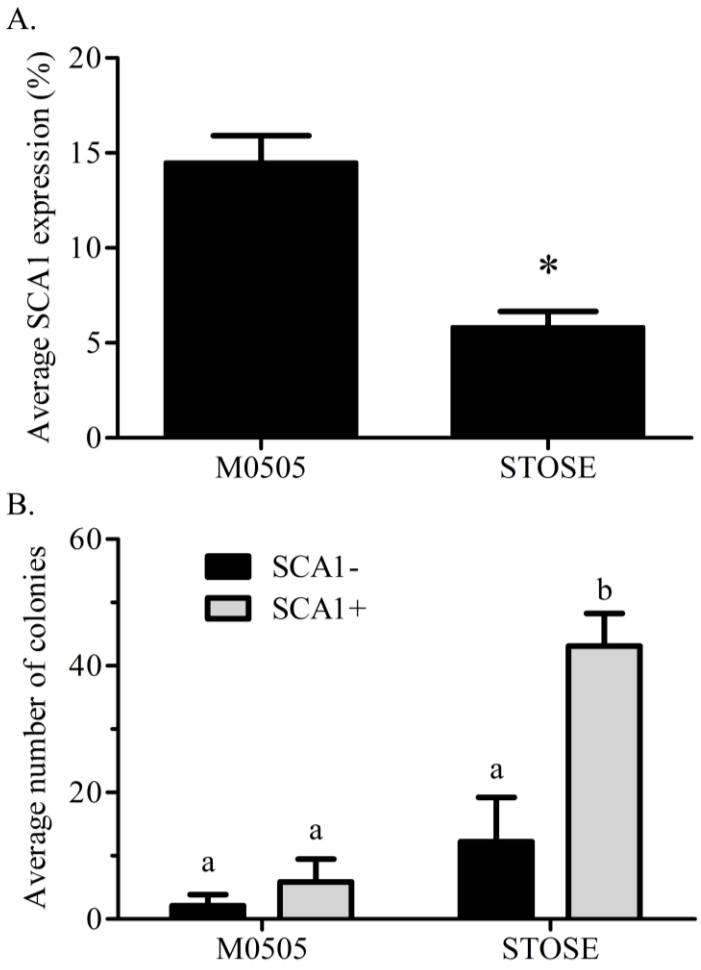

Figure 2-5. A SCA1+ population is present in STOSE cells. (A) Percentage of SCA1+ cells in M0505 (n=6) and STOSE (n=11) cells as assessed by flow cytometry. *$p<0.01$, student's t-test. **(B)** Quantification of colony formation in soft agar by SCA1+ and SCA1- M0505 and STOSE cells. Colonies were counted using ImageJ software 7 days after seeding $2.5x10^4$ cells in soft agar. The average number of colonies in 5 fields of view is presented (n=3). ANOVA was used to determine significance; bars with different letters are significantly different.

Since SCA1+ STOSE cells exhibit a more malignant phenotype *in vitro*, SCA1+ STOSE cell malignancy was tested *in vivo*. To determine if SCA1 marks cells with enhanced ability to initiate tumors, SCA1+ and SCA1- STOSE cells ($4x10^4$) were injected IB into 29 FVB/N mouse ovaries, 15 with SCA1- cells and 14 with SCA1+ cells. SCA1+ STOSE cells initiated tumorigenesis faster than SCA1- STOSE cells with the median times to a palpable tumor of 19 (n=15) and 27 days (n=14), respectively ($p<0.01$, Fig. 2-6A). There was no difference in total tumor burden between the two groups when the mice were euthanized 116 days after STOSE cell injection, with mice having a tumor burden of 2.70±0.53 g (n=7) for SCA1- tumors vs. 2.72±0.32 g (n=6) for SCA1+ tumors. At that time point, SCA1+ and SCA1- STOSE tumors also showed a similar degree of tumor dissemination, metastasizing consistently to the uterus, stomach, diaphragm, small and large intestines, spleen, and pancreas.

To determine if the increased initiation rate in SCA1+ compared to SCA1- STOSE tumors resulted in different histological presentation, immunohistochemistry was performed using markers of HGSC. Both SCA1+ and SCA1- STOSE tumors are pan-CK+, WT1+, inhibin-, and PAX8+ (Fig. 2-6B), with no gross histological differences evident between SCA1+ and SCA1- tumors. Western blot analysis confirmed strong PAX8 positivity in both SCA1+ and SCA1- STOSE tumors (Fig. 2-6C), relative to the positive control, normal uterine tissue, and to the low level of expression seen in M0505 and STOSE cells cultured *in vitro*. An independent non-tumorigenic normal OSE cell line, M1102, was used as a negative control. Expression of p53 in SCA1+ and SCA1- STOSE-derived tumors was

determined using western blot analysis. SCA1+ and SCA1- tumors were positive for p53 expression (Fig. 2-6D).

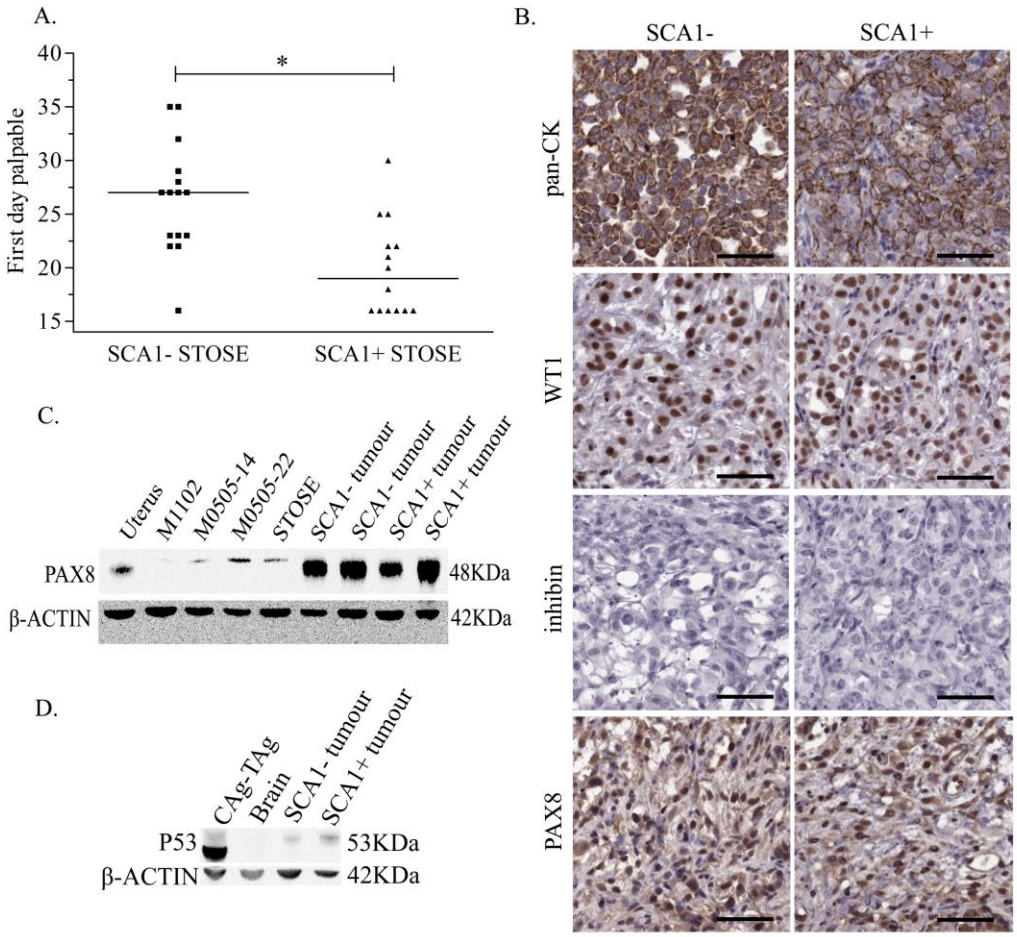

Figure 2-6. SCA1+ STOSE cells initiate HGSC tumorigenesis faster than SCA1- STOSE cells. Flow cytometric sorting was used to separate Sca1+ and Sca1- STOSE cells. SCA1+ (n=14) and Sca1- (n=15) STOSE cells were injected intrabursally into FVB/N mouse ovaries ($4x10^4$ cells/ovary). **(A)** The first day ovarian tumors were palpable after day of injection (day 0) is presented and represents the initiation of tumorigenesis. Black lines represent median values. *$p<0.01$, student's t-test. **(B)** Hematoxylin and eosin (H&E) staining and immunohistochemical staining of pan-cytokeratin (CK), WT1, inhibin, and PAX8, all commonly used markers to subtype ovarian carcinoma. Scale bars = 50 µm. **(C)** PAX8 (48 KDa) expression in cell lines and STOSE-derived SCA1+ and SCA1- tumors. Lane 1 is uterus from a wild-type FVB/N mouse as a positive control. Lane 2 is the normal M1102 OSE cell line as a negative control. Lanes 3-4 are passage 14 and 22 M0505 cells

and lane 5 is STOSE cells. Lanes 6-7 and 8-9 represent tumors derived from SCA1- and SCA1+ STOSE cells, respectively. β-ACTIN (42 KDa) was used as a loading control. **(D)** P53 (53 KDa) expression in STOSE-derived SCA1+ and SCA1- tumors. Lane 1 is a T-antigen expressing CAG-TAg tumor as a positive control. Lane 2 is brain from a wild-type FVB/N as a negative control. Lane 3-4 represents STOSE-derived SCA1- and SCA1+ tumors, respectively.

2.6 Discussion

There is substantial need for new models of HGSC that have similar expression profiles, chromosomal aberrations, and histological features characteristic of human HGSC. These models should also account for the multiple origins of HGSC in order to effectively narrow down screening targets based on the tissue of origin. The body of work presented here describes the production and characterization of a spontaneously transformed OSE cell line. STOSE cells have lost characteristic epithelial 'cobblestone' morphology, have a greatly increased proliferation rate and, form colonies in soft agar. Interestingly, there is aneuploidy in both M0505 and STOSE cells, suggesting that aneuploidy may have preceded transformation. Linear fold changes calculated from M0505 and STOSE cell microarray data revealed that STOSE cells have differentially expressed genes that are consistent with human HGSC tumor samples and previous studies on ovarian cancer cell lines. Tumors with an immunohistochemical profile of HGSC formed in all immunocompromised SCID and syngeneic FVB/N mice following IP STOSE cell injections, confirming the potential for STOSE cells to be used as a syngeneic model of HGSC. Finally, STOSE cells that express SCA1 appear to be more aggressive, with increased colony forming efficiency *in vitro* and faster tumor initiation *in vivo*.

Recent reviews have discussed the pros and cons of current models of HGSC (Garson et al., 2012; Jones and Drapkin, 2013; Lengyel et al., 2014). Current models have focused on the use of transgenics, xenografts of human cancer cells, and OSE cells transformed by genetic engineering in attempts to model HGSC. These models have had some success in modeling HGSC as well as low-grade serous, endometrioid, and granulosa cell-derived tumors, although results of these studies are highly variable and commonly have strain-dependent phenotypes (Garson et al., 2012). Most transgenics have focused on the use of the Anti-Mullerian Hormone Type II Receptor (*Amhr2* or MISIIR) promoter to drive tumor suppressor knockout or oncogene activation, but its expression in granulosa cells as well as both ovarian epithelium and fimbria can confound the results and make the origins of such cancers unclear (Garson et al., 2012). Human xenografts into immune-compromised mice have provided much knowledge on the metastasis and chemoresistance of human tumors. The lack of an immune system can limit some uses of these models, which do not accurately represent the human tumor microenvironment in which the immune system has a critical role in tumor progression and response to treatment (Jones and Drapkin, 2013; Lengyel et al., 2014). Genetically engineered OSE cells have provided much insight into genes that are sufficient to transform OSE cells (Orsulic et al., 2002; Xing and Orsulic, 2006), but their involvement in HGSC initiation or progression is unknown and manipulating such genes may not represent the natural progression of disease.

The STOSE cells reported here join a number of other spontaneously transformed rat (ROSE) (Rose et al., 1996; Testa et al., 1994) and mouse OSE cell lines that have been previously reported. Syngeneic mouse models include ID8, IF5, IG10, L-MOSE and,

MOSEC cells (Lv et al., 2012; Roberts et al., 2005; Roby et al., 2000; Urzúa et al., 2010). These models are all tumorigenic in immunocompetent mice and allow the study of immunologic parameters as well as serve as a resource to test immunotherapies in ovarian cancer (Roberts et al., 2005). Spontaneous models are beneficial since they arise from specific cell types, so their origins are clear (Ricci et al., 2013). All of the models derived from spontaneously transformed OSE cells have yielded poorly differentiated epithelial carcinomas, but have not been examined further to confirm their histologic identity as it compares with human tumors. Those lines tested have shown gene expression profiles similar to human (X. Chen et al., 2013; Foster et al., 2013).

The STOSE model is the first spontaneous HGSC model, as confirmed by the expression of immunohistochemical markers (pan-CK+, WT1+, inhibin-, PAX8+), consistent with human ovarian carcinomas (Auersperg, 2013a; Soslow, 2008). The expression of WT1 and PAX8, commonly used to diagnose HGSC, help to confirm that OSE cells have the ability to spontaneously transform into HGSC. PAX8 positivity in human HGSC is one of the characteristics used to support a fimbrial origin of HGSC (Auersperg, 2013a). It is well-established as a marker of fimbrial epithelium and, due to its expression in HGSC, much research has now focused on the fimbrial epithelium (Auersperg, 2013a; Flesken-Nikitin et al., 2013). Recently, a report has shown that PAX8+ tumors can be produced from transformed hilum cells that originate in the ovary, providing additional evidence that the OSE cells can be an origin of HGSC (Flesken-Nikitin et al., 2013). Although OSE cells have little to no PAX8 expression, our results show that both the untransformed M0505 cells as well as the STOSE cells had a low level of expression of PAX8+ (Fig. 2-6C),

suggesting that early acquisition of PAX8 expression in the M0505 cells may have facilitated the transformation of these cells. Further study of PAX8 and its function in M0505 and STOSE cells will help delineate its role in the transformation process.

The STOSE model is also the first syngeneic ovarian cancer model in the FVB/N strain of mice. All previous spontaneously transformed mouse OSE cells have been derived from C57Bl/6 mice (Lv et al., 2012; Roberts et al., 2005; Roby et al., 2000; Urzúa et al., 2006). Most spontaneous models have been produced by IP injection into syngeneic hosts, abrogating the ability to study metastasis from a specific site. The ovarian bursa is a controlled and distinct microenvironment and we have previously shown that, while tumor histology is not different when cells are injected into this location, it is an effective means to identify more invasive cells, as only aggressive cells can invade the ovary and/or breach the bursal membrane (Shaw et al., 2004). Injecting cells under the bursal membrane also provides the ability to study the immune parameters associated with metastasis that could enable the production of immune therapies to prevent metastasis. The spontaneous ID8 model has produced peritoneal metastases following IB injection into their syngeneic C57Bl/6 strain of origin (Greenaway et al., 2008). The STOSE model also forms extensive peritoneal metastases following IB injection, making STOSE the first metastatic HGSC model in the FVB/N strain. Having spontaneous models in multiple strains is an important resource to enable investigators to show that the efficacy of a therapeutic strategy is independent of strain background, greatly improving the translation of therapeutic strategies.

STOSE cells are aneuploid and have gene expression changes consistent with human ovarian cancer. Aneuploidy is common in many cancers including ovarian cancers (Birch et al., 2011; Lv et al., 2012; Padilla-Nash et al., 2013; Roby et al., 2000; Weberpals et al., 2008). Aneuploidy is a prognostic determinant in HGSC since severe aneuploidy is associated with poor outcome (Weberpals et al., 2008). STOSE cells have a high degree of aneuploidy, characterized by triploid and polyploid cells. Furthermore, the loss of genomic stability in both M0505 and STOSE cells as seen by aneuploidy may have been an early event leading to transformation that may explain the tumorigenic capacity of STOSE cells. Loss of chromosome 3, which contains many tumor suppressors, is seen in both M0505 and STOSE cells. Haploinsufficiency of chromosome 3 tumor suppressors such as *Lrrc3b* (fold change of -2.69 in STOSE cells) may underlie transformation (Haraldson et al., 2012). Similarly, chromosome 8 is lost in M0505 and STOSE cells and it has been shown to contain ovarian cancer susceptibility loci, allelic loss of which may have contributed to transformation (Australian Cancer Study et al., 2013; The Wellcome Trust Case-Control Consortium et al., 2010). Three downregulated genes in STOSE cells, *Enpp2, Sfrp1,* and *Star* are all located on chromosome 8. Loss of chromosome 8 in M0505 cells may have been an early event in transformation (Locke et al., 2012; Vidot et al., 2010).

Ingenuity pathway analysis of microarray data revealed gene expression changes related to Wnt/β-Catenin signaling in STOSE cells suggesting signaling in the Wnt pathway might be aberrant. Many of the downregulated genes in STOSE cells are associated with Wnt/β-Catenin signaling and have been associated with loss of heterozygosity or promoter methylation in ovarian cancer, including *Fzd4, Sfrp1* and, *Axin2* (Dai et al., 2011;

Notaridou et al., 2011; Takada et al., 2004; Teodoridis et al., 2005). Interestingly, *Cdkn2a* is downregulated in 30% of HGSC cases and *Ccnd1* is amplified in 4% of the cases, according to TCGA ovarian carcinoma array (Bell et al., 2011). STOSE cells have a similar expression pattern of *Cdkn2a* and *Ccnd1*. *Cdkn2a* and *Ccnd1* are both associated with Wnt/β-Catenin signaling. *Ccnd1* is a well-established target gene of β-Catenin signaling and has a role in promoting cell cycle progression, while *Cdkn2a* encodes a cell cycle inhibitor that is suppressed by β-Catenin (Bell et al., 2011; Curley and Bosenberg, 2008; Tapper et al., 2001). Due to the association of these two genes with human HGSC and aberrant Wnt signaling in STOSE cells, further study of the role of *Cdkn2a*, *Ccnd1* and Wnt/β-Catenin signaling is needed to understand the role Wnt/β-Catenin signaling in the transformation of M0505 cells into STOSE cells or in the tumorigenic capacity of STOSE cells. A greater understanding of this pathway may translate to greater knowledge on the initiation and progression of HGSC.

Interestingly, *Aldh1a2* is the most downregulated gene in STOSE cells (-170.58 fold). *Aldh1a2* is involved in retinoic acid (RA) biosynthesis and has been shown to have ubiquitous expression in the human ovarian surface epithelium (Auersperg, 2013a, 2013b). The RA-receptor β (*Rarβ*) is also downregulated in STOSE cells (-10.80 fold) suggesting multiple aspects of RA signaling are lost. RA signaling has been shown to crosstalk with Wnt/β-Catenin signaling and *Aldh1a2* has also been identified as a tumor suppressor in prostate cancer, loss of which is an early event in the disease (Kim et al., 2005; Touma et al., 2009). Further study of *Alhd1a2*, RA signaling and the crosstalk between RA and

Wnt/B-Catenin signaling may help determine the mechanisms leading to transformation and tumorigenesis in HGSC.

Investigation of a potential tumor-initiating cell population in the STOSE revealed that STOSE cells have retained a SCA1+ population that appears to have a more malignant phenotype than SCA1- STOSE cells. Tumor-initiating cells have been thought to be key contributors to HGSC etiology based on the heterogeneity and recurrence that are characteristic of the disease (X. Chen et al., 2013; Foster et al., 2013; Kulkarni-Datar et al., 2013). TICs have been identified in both human and murine ovarian cancers by sorting for CD44, CD133, CD117, CD24, ALDH1 and SCA1 expression alone or in combination (Foster et al., 2013; Kulkarni-Datar et al., 2013). SCA1 has also been used for the enrichment of a stem cell population in leukemia, prostate, and breast cancers (Kulkarni-Datar et al., 2013). STOSE cells were found to contain a SCA1+ stem cell-like population that exhibits increased malignancy both *in vitro* as assessed by colony formation and *in vivo* as assessed by initiation of tumorigenesis. Interestingly, SCA1+ and SCA1- STOSE-derived tumors were positive for p53 expression by western blot analysis. DNA sequencing showed no mutations in the p53 gene, suggesting pathways that lead to p53 stabilization might also be aberrant in STOSE cells. Our findings that the SCA1+ population exhibits TIC characteristics is in line with a recent study on SCA1+ cells in the T2 mouse model of ovarian cancer, which showed that these cells have TIC characteristics that allow them to escape chemotherapy and produce heterogeneous tumors following treatment (Kulkarni-Datar et al., 2013). The retention of a SCA1+ population with TIC characteristics allows

us to compare tumorigenic SCA1+ STOSE cells with non-tumorigenic SCA1+ M0505 cells.

In summary, this study has led to the development of a spontaneously transformed syngeneic model of HGSC in the FVB/N mouse, the first spontaneous murine model with defined features of HGSC. The STOSE model has characteristics of human disease such as aneuploidy, gene expression, and the presence of a TIC population. This model also produces extensive metastases in the peritoneal cavity following IB injection allowing for the study of tumor dissemination. Further investigation is required to understand the contribution of Wnt/β-catenin signaling in STOSE cells. The STOSE model offers vast potential for testing of novel therapeutics, including immune therapies. This model will also allow for the discovery of new screening targets that are involved in the transition of normal cells to HGSC.

2.7 Acknowledgements

This work was supported by grants from the Cancer Research Society, the Canadian Institutes of Health Research (#111194) and the Canadian Cancer Society Research Institute (#2011-700869).

2.8 Correction

Since the publication of Chapter 2 in 2014, we have noticed an error in the chromosome numbers indicated for the genes *Lrrc3b* and *Enpp2* that appear on page 60 of this thesis. In mice, *Lrrc3b* is located on chromosome 14, and *Enpp2* is located on chromosome 15. All statements made in relation to *Lrrc3b* and *Enpp2* in the context of STOSE cell transformation should be disregarded.

3 CHAPTER 3: DEEP LEARNING CLASSIFICATION OF OVARIAN CANCER

The publication of the STOSE model (Chapter 2) has opened up numerous research avenues and collaborations for our laboratory. We have begun collaborations that aim to develop novel immunotherapies for ovarian cancer, including oncolytic viruses and a novel antibody therapy. In addition to developing therapeutics, the STOSE model offers a resource for optimizing diagnostic imaging techniques that could accelerate diagnostics or resolve histologically challenging problems such as chemoresistance. Recent imaging techniques including second-harmonic generation (SHG), two-photon excitation fluorescence (TPEF), and Raman spectroscopy can resolve tissue structure at a submicron resolution (Keikhosravi et al., 2014; Strupler et al., 2007). This allows for the development of advanced algorithms, particularly using machine and deep learning, that aim to determine whether structural differences in tissues can provide information on benign vs. malignant disease, cancer type, subtype, prognosis, and also project treatment efficacy (Watson et al., 2014; Wen et al., 2016, 2014; Williams et al., 2010). The use of Raman imaging was recently shown to stratify chemoresistant and chemosensitive cells (Moradi et al., 2017). Two recent studies have combined multiphoton microscopy with SHG and were able to determine the difference between normal and cancerous tissues in unstained, fixed, human ovarian cancer samples, and in live tumor-bearing mice (Watson et al., 2014; Williams et al., 2010). However, this approach still requires advanced training to analyze the resulting images. Further, trained pathologists are already extremely adept at determining if tissue is malignant. Thus, to complement a pathologist's diagnostic arsenal, the next paper details a proof-of-principle approach that uses deep learning, a type of artificial intelligence, to classify SHG and TPEF images.

This paper is published:

Huttunen, M.J., Hassan, A., McCloskey, C.W., Fasih, S., Upham, J., Vanderhyden, B.C., Boyd, R.W., Murugkar, S., 2018. Automated classification of multiphoton microscopy images of ovarian tissue using deep learning. J Biomed Opt 23, 1–7. https://doi.org/10.1117/1.JBO.23.6.066002

Automated classification of multiphoton microscopy images of ovarian tissue using deep learning

Mikko J. Huttunen,[a,b,*] Abdurahman Hassan,[a] Curtis W. McCloskey,[c,d] Sijyl Fasih,[a] Jeremy Upham,[a] Barbara C. Vanderhyden,[c,d] Robert W. Boyd,[a,e] and Sangeeta Murugkar[f]

[a]University of Ottawa, Department of Physics, 25 Templeton Street, Ottawa, Canada, ON K1N 6N5
[b]Tampere University of Technology, Laboratory of Photonics, Korkeakoulunkatu 3, Tampere, Finland, FI-33101
[c]University of Ottawa, Department of Cellular and Molecular Medicine, 451 Smyth Road, Ottawa, Canada, ON K1H 8M5
[d]Ottawa Hospital Research Institute, Centre for Cancer Therapeutics, 501 Smyth Road, Ottawa, Canada, ON K1H 8L6
[e]University of Rochester, Institute of Optics and Department of Physics and Astronomy, 480 Intercampus Drive, Rochester, USA, NY 14627
[f]Carleton University, Department of Physics, 1125 Colonel By Drive, Ottawa, Canada, ON K1S 5B6

Keywords: Medical and biological imaging; Ovarian cancer; Optical pathology; Tissue characterization; Nonlinear microscopy, convolutional neural networks.

*Mikko J. Huttunen, E-mail: mikkojhuttunen@gmail.com

3.1 Author contributions

This project was a collaborative effort between Dr. Mikko Huttunen, a post-doctoral fellow in the lab of Dr. Robert Boyd, and our lab. Dr. Vanderhyden and I contributed theoretically in the experimental design and helped develop a biologically relevant question. I generated the STOSE tumors through IB injections, processed the tissue and stained them with picrosirius red stain leading to my place as third author on the publication. All SHG and TPEF images were acquired by Abdurahman Hassan and Sijyl Fasih. Dr. Huttunen performed all deep learning analysis and wrote the manuscript. Dr. Vanderhyden and I were heavily involved in editing the manuscript where ovarian cancer and models are discussed.

3.2 Abstract

Histopathological image analysis of stained tissue slides is routinely used in tumor detection and classification. However, diagnosis requires a highly trained pathologist and can thus be time-consuming, labor-intensive and potentially risks bias. Here, we demonstrate a potential complementary approach for diagnosis. We show that multiphoton microscopy images from unstained, reproductive tissues can be robustly classified using deep learning techniques. We fine-train four pre-trained convolutional neural networks by using over 200 murine tissue images based on combined second-harmonic generation and two-photon excitation fluorescence contrast, to classify the tissues either as healthy or associated with high-grade serous carcinoma with over 95% sensitivity and 97% specificity. Our approach shows promise for applications involving automated disease diagnosis. It could also be readily applied to other tissues, diseases and related classification problems.

3.3 Introduction

Ovarian cancer is the most lethal gynecological malignancy with an estimated 22,280 new cases and 14,240 deaths in 2016 in the US alone (Siegel et al., 2016). High-grade serous carcinoma (HGSC) is the most common type of epithelial ovarian cancer accounting for 70% of the cases and associated with a low 5-year survival rate of only 40% (McCloskey et al., 2014). Due to the lack of effective screening and diagnostic imaging techniques, the disease is normally detected at a late stage after wide-spread dissemination. Furthermore, the existing techniques do not permit the detection of microscopic residual disease at the time of surgery. There is thus an urgent need for developing a high resolution imaging

technique that permits the rapid and automated detection of early and recurrent ovarian cancer from tissue biopsies with high accuracy.

Multiphoton microscopy is a high-resolution optical imaging technique that is becoming an indispensable tool in cancer research and diagnosis (Campagnola, 2011; Denk et al., 1990; Kirkpatrick et al., 2007; Nadiarnykh et al., 2010; Prat, 2012; Watson et al., 2014; Williams et al., 2010). In this imaging paradigm, the nonlinear optical signals are generated only at the focal point of the excitation beam, providing intrinsic 3D optical sectioning and permitting non-destructive, label-free imaging. In particular, second-harmonic generation (SHG) imaging provides intrinsic contrast to visualize the organization of collagen fibers and elastin, which are major constituents of the extracellular matrix (ECM), the distribution of which can be a key identifier for several diseases (Kirkpatrick et al., 2007; Nadiarnykh et al., 2010). Another example is two-photon excitation fluorescence (TPEF) imaging of intrinsic tissue fluorescence, which enables the identification of changes in cellular morphology and organization. SHG and TPEF imaging have been utilized to demonstrate that remodeling of the ECM is associated with cancer progression (Bonnans et al., 2014; Cox and Erler, 2011; Kirkpatrick et al., 2007; Nadiarnykh et al., 2010; Provenzano et al., 2008; Williams et al., 2010). Wen *et al.* (Wen et al., 2014) implemented 2D texture analysis of SHG images from unstained ovarian tissue to quantify the remodeling of the ECM. Recently, the approach was generalized to 3D texture analysis and to classify SHG images from six different ovarian tissue types (Wen et al., 2016). These studies demonstrate the potential of machine learning based evaluation of SHG images for improved diagnostic accuracy of ovarian cancer detection.

In machine learning the computer programs learn to perform data analysis tasks, such as image classification, that are hard to perform algorithmically due to the complexity of the data set. Image classification is often achieved using supervised learning, where the task is learned by using labeled training images. In general, the labeled images are used to learn a more optimal representation of the image data, which facilitates clustering of the images into clearly separated sets and thus enables their classification. Several supervised learning approaches exist for classification tasks; support vector machines (SVMs) and logistic regression are among the most commonly used due to their relative simplicity and performance (Chapelle et al., 1999). However, these classification approaches require extensive image processing and hand-crafted feature extraction procedures. In contrast, deep learning is a rapidly growing area of machine learning, in which data are analyzed using multilayered artificial neural networks that avoid extensive human intervention (Krizhevsky et al., 2012). In particular, convolutional neural networks (CNNs) have been applied also for classifying images of stained tissue biopsy slides (Donahue et al., 2013; "grand-challenges - Home," n.d.; He et al., 2015; Krizhevsky et al., 2012; Simonyan and Zisserman, 2014; Szegedy et al., 2014; D. Wang et al., 2016). In these studies, the CNNs have been trained using large amounts of data consisting of millions of images (Deng et al., 2009; Russakovsky et al., 2014). But so far, the use of CNNs in the classification of multiphoton images has been remarkably limited (Weng et al., 2017), mainly because of the small size of the typically available data set. However, with the development of deep learning techniques for high-accuracy classification that require fewer training images, its application to multiphoton image data sets has become more viable, which could lead to rapid and reliable automated diagnostic tools.

In this paper, we demonstrate the use of deep neural networks for robust and real-time classification of multiphoton microscopy images of unstained tissues. We acquire SHG and TPEF images of ovarian and upper reproductive tract tissue from healthy mice and tumor tissue from orthotopic syngeneic HGSC murine models. We construct binary image classifiers (healthy versus HGSC) by fine-tuning pre-trained CNNs using a relatively small acquired data set consisting of ~200 multiphoton images. We study the performance of four pre-trained CNNs (AlexNet, VGG-16, VGG-19 and GoogLeNet), and examine the role of data augmentation on the results. We demonstrate classification of the acquired images with over 95% sensitivity and 97% specificity. In particular, we show that best classification performance is achieved when the combined TPEF and SHG data are used compared to using only the SHG or TPEF data. The trained classifiers are also shown to outperform more traditional classifiers based on SVMs. Because the demonstrated approach is minimally invasive, operates in real-time and requires very little sample preparation, it has potential for clinical applications and for computer-aided diagnosis.

Image classification using pre-trained convolutional neural networks

Deep learning and CNNs have recently proved useful for various computer vision tasks (Donahue et al., 2013; "grand-challenges - Home," n.d.; He et al., 2015; Krizhevsky et al., 2012; Simonyan and Zisserman, 2014; Szegedy et al., 2014; D. Wang et al., 2016). Although several CNNs with different architectures and configurations exist, their overall working principles are similar. The input image is passed through the CNN consisting of different layers, such as convolutional, pooling, activation and fully-connected, where each layer performs specific types of data operations. The layers are made of artificial neurons,

which calculate a weighted sum of the inputs and transform it, often with a bias, to an output using a transfer function. During the training process of the CNN, the weights and biases of the artificial neurons are optimized leading to the desired performance of the network, such as distinguishing between healthy and diseased tissue samples.

In convolutional layers, the input data is convolved using various filters into a more useful representation, which can be used for example in feature detection/extraction. The number of sequential convolutional layers, i.e. the depth of the CNN, varies from a few layers to hundreds of layers where the deeper CNNs are computationally more expensive but often outperform shallower ones (Krizhevsky et al., 2012; Simonyan and Zisserman, 2014). Pooling layers down-sample the input to reduce its dimensionality. Activation layers, such as rectified linear units, provide nonlinearity to the signal processing allowing faster and more effective training of the network (Krizhevsky et al., 2012). At the end of the CNN, fully-connected (FC) layers are used to compute the output, in our case the binary class scores (healthy vs. HGSC) for each input image. Alternatively, the FC layers can be replaced by other classifiers, for example based on logistic regression or SVMs, which are optimized for the task of classification (Mostaço-Guidolin et al., 2013).

After the CNN is designed, it needs to be trained for the particular task. For the case of supervised learning this is done by forming a cost function for the network and using it to compare the calculated output of the network with the desired output. The network is then trained by iteratively optimizing its weights and biases to minimize the cost function. This process utilizes gradient descent method and a procedure known as backpropagation

(Rumelhart et al., 1988). First and foremost, a large data set is needed to successfully train a network from scratch and to overcome problems related to overfitting. For example the well-known AlexNet was trained using ~1.2 million images divided into 1000 categories (Deng et al., 2009; Krizhevsky et al., 2012).

For our task of binary classification of multiphoton images from ovarian and surrounding reproductive tract tissues no extensive data sets yet existed, and neither was it feasible to generate a vast amount of data. Therefore, instead of training a CNN from scratch, we used four pre-trained CNNs (AlexNet, VGG-16, VGG-19 and GoogLeNet). These CNNs were chosen as they are openly available and due to their success in the ImageNet Large Scale Visual Recognition Challenges (Deng et al., 2009; Russakovsky et al., 2014). AlexNet was the first successful CNN winning the 2012 challenge outperforming thus the more conventional approaches. The more sophisticated VGG-16 and VGG-19 networks were the winners of the following year and were again superseded by the GoogLeNet in the 2014 competition. Since we had no prior knowledge on how well each of these CNNs could perform on our classification task, we fine-trained all of them.

We replaced their last few FC layers, originally responsible for the 1000-way classification of ImageNet data (Deng et al., 2009; Russakovsky et al., 2014), with a binary classifier enabling fine-training of the modified CNN using a considerably smaller data set consisting of ~200 images. Since it was not a priori clear what kind of classifier would result in the best classification performance, we used two different approaches. In the first, we replaced the final FC layers by a linear SVM, since SVMs are often used for binary image

classification. In the second approach, we replaced the final FC layers by new layers (sequential FC, Softmax and classification layers) more suitable for binary classification. Figure 3-1 shows a layout illustrating the two chosen approaches. Since in these approaches we were fine-training the modified CNNs using smaller amounts of data, overfitting could cause problems, but such problems were mitigated by data augmentation and dropout as shown in earlier reports focusing on medical image analysis (Bar et al., 2015; Mostaço-Guidolin et al., 2013; Srivastava et al., 2014; Tajbakhsh et al., 2016; D. Wang et al., 2016).

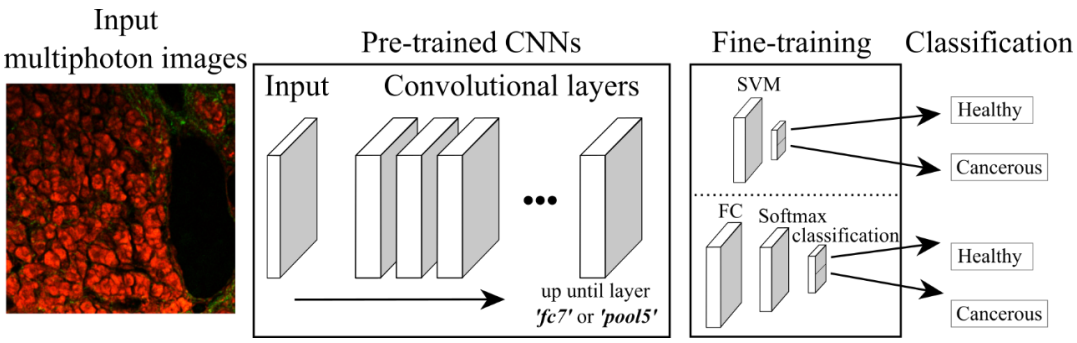

Figure 3-1. Schematic of the two transfer learning approaches used in this study for classifying the input multiphoton images either as healthy or cancerous (HGSC). In both cases, the input images are fed to the pre-trained CNNs, which transform the data into a more optimal representation enabling robust classification. In the first approach, the output of the pre-trained CNN is fed to a trained SVM classifier. In the second approach, the final FC layers of the pre-trained CNNs are replaced by new FC layers more suitable for binary classification.

3.4 Results

Animal experiments were performed in accordance with the Canadian Council on Animal Care's *Guidelines for the Care and Use of Animals* under a protocol approved by the University of Ottawa's Animal Care Committee. Samples were acquired from five healthy FVB/n mice and five syngeneic mice with HGSC-like ovarian cancer generated by injection of spontaneously transformed ovarian surface epithelial (STOSE) cells under the ovarian bursa (McCloskey et al., 2014). Five 6 μm thick sections were prepared both from the upper reproductive tract of healthy mice (n = 5) and from STOSE ovarian tumors (n = 5). Four sections from each sample were left unstained and imaged using a multiphoton microscope. One section per sample was stained with picrosirius red and was used for overall inspection of the tissues.

All samples were imaged by measuring back-scattered TPEF and SHG signals. In order to ensure that the trained classifiers could correctly classify images where parts of surrounding non-ovarian tissues are present, tissues from the upper part of the reproductive tract were also imaged. A Ti:Sapphire femtosecond laser (Mai Tai HP, Spectra Physics) with 80 MHz repetition rate and ~150 fs pulses at the incident wavelength of 840 nm was used for excitation in conjunction with a laser-scanning microscope (Fluoview FVMPE-RS, Olympus). All measurements were taken with a 40× (NA = 0.8) water-immersion objective (LUMPlanFL, Olympus). The average incident power at the sample plane was 5-10 mW, which was adjusted using a polarizer and a rotating half-wave plate along the beam line. A quarter-wave plate and a Soleil-Babinet compensator were used to ensure that the incident polarization at the sample plane was circular. Circular polarization was used to

make sure that anisotropic structures, in our case mainly the collagen fibers, were evenly excited and imaged. The back-scattered nonlinear signals were separated from the fundamental beam using a dichroic mirror (DM690, Olympus). The TPEF signal was separated from the SHG signal using another dichroic mirror (FF452-Di01, Semrock) and the SHG signal was further filtered using a band-pass filter (FF01-420/10, Semrock).

Both SHG and TPEF images consisting of 800×800 pixels were simultaneously acquired with a field of view of ~250×250 μm². A pixel dwell time of 8 μs was used and each image pixel was averaged 16 times to improve the signal-to-noise ratio, resulting in an imaging speed of 82 s per image. The raw data were transformed into RGB images, where the red (green) channel corresponded to TPEF (SHG) signal and the blue channel was set to zero. Representative multiphoton images from healthy and cancerous reproductive tissues alongside with the corresponding bright-field images from adjacent stained sections are shown in Fig. 3-2. Remodeling of the ECM is visible as an increase in the amount of collagen and thus SHG signal in the cancerous tissue, while changes in the overall tissue morphology are seen in the TPEF signal [compare Figs. 3-2(c) and 3-2(f)].

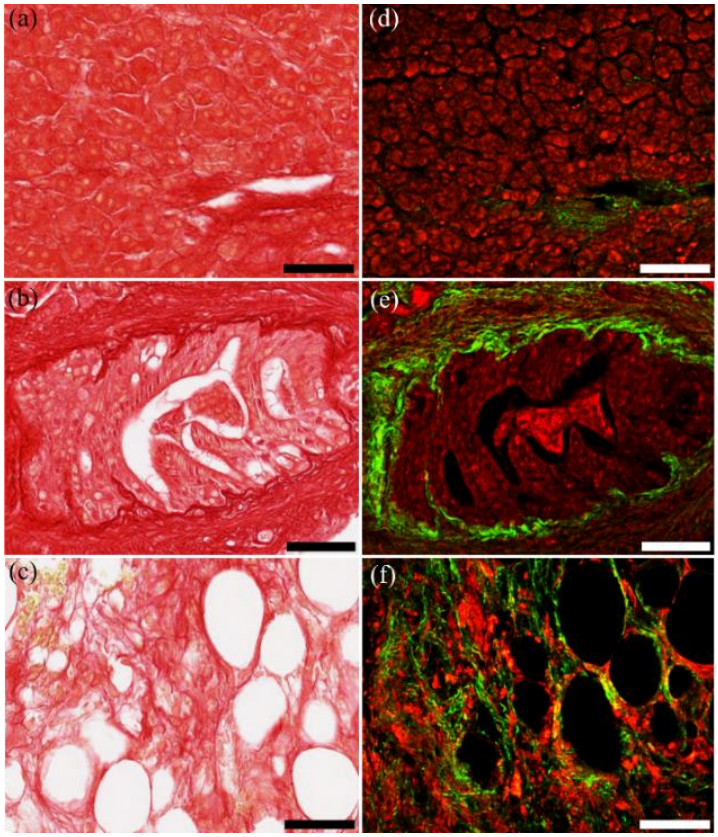

Figure 3-2. SHG and TPEF imaging of murine tissues. Left: Representative bright-field images from stained murine model (**a**) healthy ovarian tissue, (**b**) healthy reproductive tract tissue and (**c**) HGSC tissue. Collagen appears dark red in the stained tissue images. Right: (**d**)-(**f**) Corresponding multiphoton images from adjacent unstained sections, respectively. Relative to healthy ovary (**a**) and (**d**), remodeling of ECM is visible in cases of HGSC (**c**) and (**f**) as an increase in the amount of collagen and consequent SHG signal (green). In addition, the overall tissue morphology becomes less organized which is visible in the intrinsic TPEF signal (red). Scale bars are 50 μm.

As the data set of ~200 images was relatively small for our purposes, we first augmented the data using patch extraction. The original RGB images were divided into N evenly spaced patches (see Fig. 3-3) consisting of 227×227 (224×224) pixels, to match the input size requirements of the pre-trained CNN AlexNet (VGG-16, VGG-19 and GoogLeNet). This choice also maintained the same field-of-view in the patches, as varying field-of-view might affect the results. To minimize the amount of overlapping data we only considered cases N = 1, 4, 9, 16 and 25. The performed patch extraction for one example image for the case of N = 25 is illustrated in Fig. 3-3. Due to the reduced field-of-view some of the image patches were found to be very dark, containing only minimal image features. As such patches could compromise the training, patches with mean pixel values below 3% of the maximum pixel count value were excluded from the analysis. Data sets processed in this way were further augmented using horizontal and vertical reflections together resulting in further threefold increase in the data set size. Therefore, the overall data augmentation scheme, consisting of patch extraction along with horizontal and vertical reflections, led up to a 75-fold increase in the training set size.

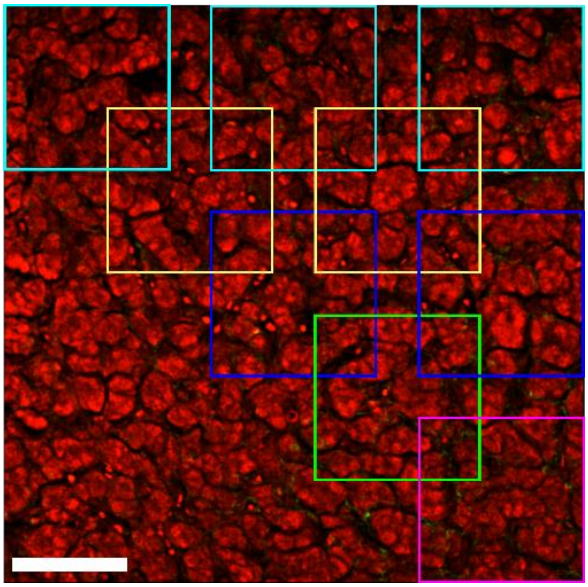

Figure 3-3. Schematic illustrating the overlap between the extracted patches (colored squares) for the case of N = 25. For clarity, only every second patch in each row on the upper triangle of the image is shown. Scale bar is 50 μm.

The whole data set was randomly divided into training and validation sets using a ratio of 60/40 respectively. The classifiers were then trained using the training data set and validated using the validation set by calculating the classification sensitivity (true positive rate), specificity (true negative rate) and accuracy (number of correct classifications divided by the total number of cases). The classification performance of the two studied approaches as discussed in Section 2 (using SVMs with learned features from pre-trained CNNs versus fine-trained modified CNNs), was quantified in this way. Since the training and validation sets were randomly chosen, the calculated accuracies varied slightly for each training event. Therefore, training events were repeated 25 times and the mean sensitivities, specificities and accuracies (along with their standard deviations) are reported for better representation of the results. The results for all the studied classifiers are shown in Fig. 3-4.

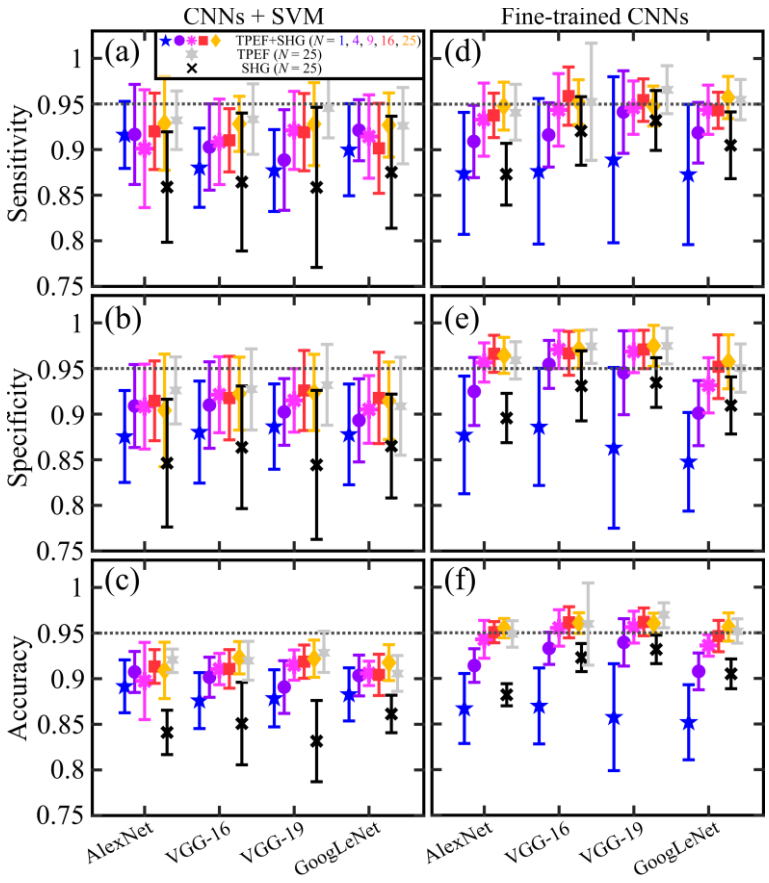

Figure 3-4. Pre-trained CNNs stratify STOSE tumors and healthy reproductive tract. Left: Calculated (**a**)-(**c**) sensitivity, specificity and accuracy for the classifiers using SMVs with learned features from the pre-trained CNNs, respectively. Right: Calculated (**d**)-(**f**) sensitivity, specificity and accuracy for the classifiers formed by fine-training the CNNs. In general, increasing number of image patches *N* improves the results (see colored markers). Each data point is the mean result of 25 separately trained classifiers with the error bars corresponding to the respective standard deviation. Classification performance using only the SHG (TPEF) data are shown with black crosses (gray stars), on average resulting in ~5 % (~0.3 %) decrease in the classification performance compared to classifiers trained using both the TPEF and the SHG data.

As a second step, we estimated how well the approach generalizes to independent data sets by performing leave-two-mice-out cross-validation, where the classifiers are trained using image data taken from eight mice and validated using the two remaining independent ones. This better represents a realistic scenario in which the classifier is first trained on known samples, and then used to diagnose a sample being observed for the first time. Because the approach of fine-training CNNs resulted in better classification performance compared to using SVMs with learned features from the pre-trained CNNs, only the approach based on fine-training CNNs was used for this validation test. During this test, the CNNs were independently trained on sets from eight samples before being validated on the remaining two samples, which they were seeing for the first time. The training process was repeated for all the 25 possible data set permutations and the results for the calculated sensitivities, specificities and accuracies with their standard deviations are shown in Fig. 3-5.

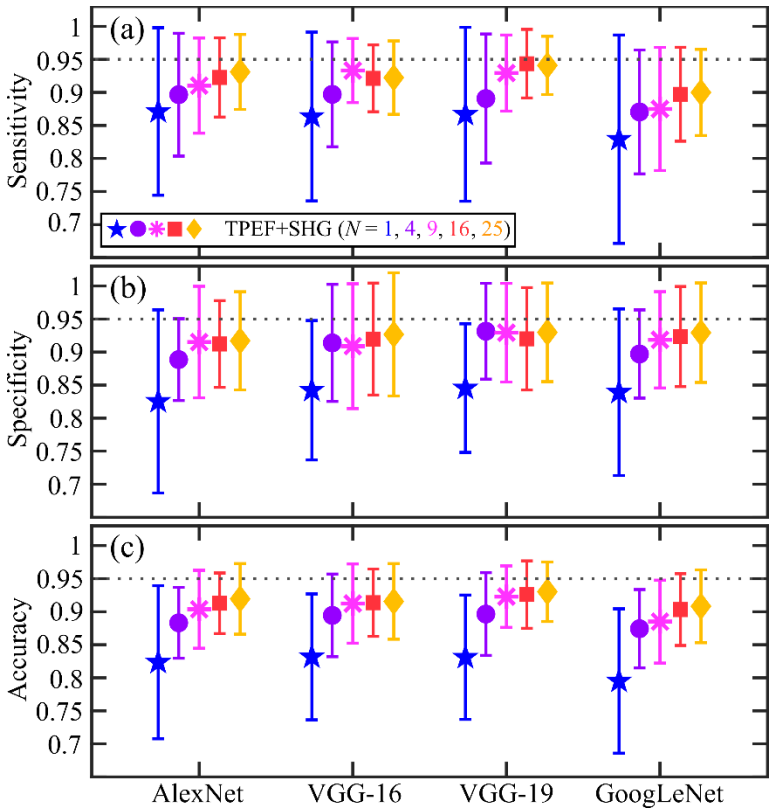

Figure 3-5. Calculated (a) sensitivity, (b) specificity and (c) accuracy for the four fine-trained CNN classifiers using leave-2-mice-out cross-validation with the error bars corresponding to the respective standard deviation. Both TPEF and SHG data were used in the training and analysis. The fine-trained VGG-19 network showed the best classification sensitivity (94.1±4.4 %), specificity (93±7.5 %) and accuracy (93±4.5 %) for the case of N = 25 (marked as yellow diamonds), respectively.

3.5 Discussion

In general, three trends are visible in our results. First, it is clear that the patch extraction improves the results, since increasing N systematically improves the classification performance (see the colored markers in Fig. 3-4). Second, more conventional classifiers based on SVMs [see Fig. 3-4(a)] are clearly outperformed by the classifiers based on fine-trained CNNs [see Fig. 3-4(b)]. When fine-trained CNNs are used, the classification sensitivity, specificity and accuracy all increase on average by ~3 %, which is a marked improvement. Third, classification performance (sensitivity, specificity and accuracy) increase by ~5 % when the classifiers are trained using both the TPEF and the SHG data (see the colored markers in Fig. 3-4), compared to training using only the SHG data (see the black crosses in Fig. 3-4). However, when the classifiers were trained by using only the TPEF data, the classification performance decreased only marginally (~0.3 %) compared to training with both TPEF and SHG data. This is a somewhat surprising result, because one intuitively expects a clear increase in classification performance when more data is used. Further investigation would be necessary to determine whether this performance difference is typical. Therefore, combined TPEF and SHG microscopy seems beneficial over solely SHG (or TPEF) microscopy. This is somewhat expected since the data set is twice as big, and since the TPEF+SHG images can support additional features not visible in bare SHG or TPEF images.

The highest mean sensitivity (95.2±2.5 %), specificity (97.1±2.1 %) and accuracy (96.1±1.1 %) were found by fine-training the VGG-16 network using $N = 25$ image patches while using the training/validation scheme (see Fig. 3-4). But we note that all the studied

CNNs performed almost equally well, implying that the choice of which pre-trained CNN to use is not crucial. We believe that this is mostly because the studied CNNs were originally designed and trained to classify images into 1000 of different classes, which is a considerably more challenging computer vision task than the binary classification performed in this work. Therefore, it seems plausible that all of the studied CNNs exhibited adequately complex network structures to allow their successful training for the simpler task of binary classification. However, the size of the training data set was found important and should be maximized, for example using data augmentation, as done in this work.

Then we discuss the leave-two-mice-out cross-validation results (see Fig 3-5). In general, the calculated sensitivities, specificities and accuracies were slightly lower (~3-4%) than what we achieved using the randomized training/validation scheme (see Fig. 3-4). However, the best performing classifier (fine-trained modified VGG-19) still resulted in very high classification sensitivity (94.1±4.4%), specificity (93±7.5%) and accuracy (93±4.5%) for the case of N = 25 (marked as yellow diamonds). Therefore, the results suggest that the studied approach could provide automated and reliable ovarian tissue classification based on label-free multiphoton microscopy images.

Label-free images based on contrast from intrinsic multiphoton SHG and TPEF processes were used to demonstrate the deep learning technique in this study. Among the many advantages of the demonstrated approach is that it scales very favorably with the increasing amount of data. This is not necessarily the case for more conventional approaches based on user-defined filters and data analysis (Mostaço-Guidolin et al., 2013; Wen et al., 2016).

The amount of training data could be increased further using a multimodal approach based on other label-free nonlinear modalities, such as third-harmonic generation (Débarre et al., 2006; Weigelin et al., 2016), coherent anti-Stokes Raman scattering (Weng et al., 2017), or polarized SHG (Golaraei et al., 2014; Lee et al., 2013; Rouède et al., 2017; Strupler et al., 2007). In addition, considerably larger data sets could be generated for example, by switching to 3D volumetric imaging. Recent work suggests that such a switch could improve the classification accuracy (Wen et al., 2016).

The method demonstrated in this study is quite general, and could be readily extended to other tasks, such as multi-class classification of tissues between known cancer types or stage classification of malignant tumors (Brierley JD., Gospodarowicz MK., Wittekind C., 2017; Wen et al., 2016). We also believe that this approach is not restricted only to cancerous tissues, but could be straightforwardly extended to study and classify other diseases/disorders known to correlate with ECM remodeling, such as many fibrotic diseases (Bonnans et al., 2014; Cox and Erler, 2011; Rouède et al., 2017; Strupler et al., 2007).

Finally, we discuss the speed of the approach. The complexity of the used CNN and the amount of data defines the training time along with the used training parameters. Training was performed using stochastic gradient method with a batch size of 50, initial learning rate of 0.0001 for up to four epochs (Krizhevsky et al., 2012). Fine-tuning the simplest CNN (AlexNet) using 25 image patches took around 300 s, whereas the same training took ~1 hour for the computationally most demanding CNN (VGG-19). A graphics processing

unit (NVIDIA GeForce GTX 1080 Ti) was used to speed-up the training. We note that the training times were considerably shorter when the learned features of pre-trained CNNs were used to train a SVM classifier. But we emphasize that irrespective of the training time, which in general could be long, the actual classification process using the learned classifiers is quite fast (8-50 ms/image). Therefore, the computationally demanding training process does not compromise potential applications, since real-time image classification is perfectly feasible.

3.6 Conclusion

We have performed combined second-harmonic generation (SHG) and two-photon excitation fluorescence (TPEF) microscopy on normal and cancerous murine ovarian and surrounding reproductive tissues. We demonstrated that already with a relatively small data set consisting of ~200 images, pre-trained convolutional neural networks can be fine-trained into binary image classifiers to correctly classify the images with over sensitivity 95 % and 97 % specificity. We compared four pre-trained networks (AlexNet, VGG-16, VGG-19 and GoogLeNet), and investigated how data augmentation improves the classification performance. We also showed that training the classifiers using both the TPEF and SHG data is beneficial compared to using only the SHG data.

Histopathological image analysis of stained tissue slides is routinely used in tumor detection and classification. Diagnosis requires a highly trained pathologist and can thus be time-consuming, labor-intensive and potentially risks bias. The trained classifiers demonstrated in this paper perform in real-time and could thus be potentially useful for

clinical applications, such as for computer-aided diagnosis. The technique demonstrated here will also be valuable for investigating the etiology of ovarian cancer. Since the approach is very general, it could be easily extended to other nonlinear optical imaging modalities and to various biomedical applications.

3.7 Disclosures

The authors have no relevant financial interests in this article and no potential conflicts of interest to disclose.

3.8 Acknowledgments

The Canada Excellence Research Chairs and Natural Sciences and Engineering Research Council of Canada (NSERC) (RGPin-418389-2012 - RWB); NSERC-Discovery Grant (SM); Finnish Cultural Foundation (00160028 - MJH); Academy of Finland (310428 - MJH); Vanier Canada graduate scholarship (CM).

4 CHAPTER 4: METFORMIN USE ABROGATES AGE-ASSOCIATED OVARIAN FIBROSIS – A POSSIBLE STRATEGY FOR OVARIAN CANCER PREVENTION.

Our ongoing collaborations with the STOSE model led us to appreciate the role of the tumor microenvironment, both structural and cellular features, in mediating treatment resistance for both chemotherapy and immunotherapy. The tumor stroma has characteristic changes in collagen structure commonly referred to as desmoplasia (DeClerck, 2012). These structural changes are known to induce inflammation and provide mechanosensory cues to tumor cells that facilitate their invasion and migration (reviewed in Harper et al., 2018). Interestingly, the changes in structure and cellular composition seen in the tumor stroma is consistent with features of a pre-metastatic niche, particularly in fibrotic organs (Cox and Erler, 2014). Given that the ovary is a common site of metastasis and the recent identification of age-associated murine ovarian fibrosis (Bigorie et al., 2010; Briley et al., 2016; Li et al., 2012; Loughran et al., 2018), we next aimed to determine if the primary non-hereditary ovarian cancer risk factors of age and ovulation contribute to the formation of a pre-metastatic fibrotic niche within the aging human ovary. The paper below delves into our findings.

This paper has been submitted to Science Translational Medicine in September 2018.

Metformin use abrogates age-associated ovarian fibrosis – a possible strategy for ovarian cancer prevention

Authors:

Curtis W. McCloskey[1,2], Brendan S. Kelly[1,2], David P Cook[1,2], Christian H. Allen[3], Amanda Forsyth[4], Jer Upham[5], Katey J. Rayner[6], Douglas A. Gray[1], Robert W. Boyd[5], Sangeeta Murugkhar[3], Bryan Lo[1,7,8], Mary K. Senterman[4,8], Barbara C. Vanderhyden[1,2*].

Affiliations:

[1]Cancer Therapeutics Program, Ottawa Hospital Research Institute, 501 Smyth Road, Ottawa, ON K1H 8L6, Canada.

[2]Department of Cellular and Molecular Medicine, University of Ottawa, 451 Smyth Road, Ottawa, ON K1H 8M5, Canada.

[3]Carleton University, Department of Physics, 1125 Colonel By Drive, Ottawa, ON, K1S 5B6, Canada.

[4]Department of Obstetrics and Gynecology, University of Ottawa, Ottawa, ON, K1H 8L6, Canada.

[5]University of Ottawa, Department of Physics, 25 Templeton Street, Ottawa, ON, K1N 6N5, Canada.

[6]University of Ottawa Heart Institute, Department of Biochemistry, Microbiology and Immunology, Faculty of Medicine, Canada

[7]Molecular Oncology Diagnostics Laboratory, Division of Anatomical Pathology, The Ottawa Hospital, Ottawa, ON, Canada.

[8]Department of Pathology and Laboratory Medicine, University of Ottawa, Ottawa, ON, K1H 1C4, Canada.

*To whom correspondence should be addressed: bvanderhyden@ohri.ca; Tel.: 613-737-7700 (ext. 70330).

One Sentence Summary: Metformin use abrogates age-associated ovarian fibrosis to reduce tumor-permissivity, offering support for metformin use as a strategy for ovarian cancer prevention.

4.1 Author contributions

All experiments were designed by Dr. Barbara Vanderhyden and me.

Brendan Kelly performed much of the murine IHC and quantification with my guidance and supervision. Human ovaries and patient histories were acquired by Dr. Mary Senterman and Dr. Amanda Forsyth. I performed all human IHC staining and quantification, microdissection, Nanostring and GO term analysis. David Cook performed unsupervised clustering and visualization of clustering data. Christian Allen and Jeremy Upham acquired the SHG images and I performed the image quantification. I wrote the manuscript with editing done by Dr. Vanderhyden and feedback from all authors.

4.2 Abstract

Age and the number of life-time ovulations are the primary non-hereditary risk factors for ovarian cancer, but reasons for this remain largely unknown. Ovulatory risk is especially curious since ovarian cancer incidence increases in postmenopausal women, after ovulations have ceased. Recent evidence has shown age-associated ovarian fibrosis develops in murine ovaries and correlates with enhanced inflammatory signaling. To determine how age and the accumulation of ovulatory events underlies ovarian cancer risk, we validated the development of age-associated ovarian fibrosis and provide further support for the development of a chronic inflammation with age in murine ovaries. Using Masson's trichrome staining and second harmonic imaging, we provide novel evidence that ovarian fibrosis also develops in post-menopausal women. RNA was isolated from the human ovarian cortex using automated microdissection, and subsequent gene expression analyses and immunohistochemical validation showed that fibrotic ovaries have enhanced inflammation with an increased CD206:CD68 ratio, increased abundance of CD8+ T cells and pro-fibrotic DPP+αSMA+ fibroblasts. These results provide support for a novel hypothesis that unifies the age and ovulatory ovarian cancer risk factors through the development of ovarian fibrosis that generates a premetastatic niche. Fibrosis, fibroblast activation, CD8+ T cell infiltration, and macrophage polarization were reversed or inhibited in the ovaries of post-menopausal women taking metformin, providing a novel mechanism to explain its ability to reduce ovarian cancer risk and supporting metformin use as a strategy for ovarian cancer prophylaxis.

4.3 Introduction

Ovarian cancers are the fifth leading cause of cancer-associated death in women and the most lethal among gynecological malignancies (Auersperg, 2013c). Five-year survival is estimated at 47.4% in part due to a lack of sensitive screening methods to detect early disease and a lack of treatments for chemotherapy-refractive patients (National Cancer Institute, 2018). Given the difficulty in detecting and treating ovarian cancer, the development of novel prevention methods is a sought-after public health goal.

In seeking novel ovarian cancer prevention strategies, much can be learned by studying established risk factors. Age and the number of lifetime ovulations are the primary non-hereditary risk factors and are proportional to risk (Auersperg, 2013c; Fathalla, 2013; Fleming et al., 2006), and *BRCA* mutations are the primary hereditary risk factors with differential risk conferred by the site of mutation (Rebbeck et al., 2015). Two prevention methods currently exist that aim to attenuate these risk factors, each with noteworthy shortcomings. First, the removal of both sites of ovarian cancer origin, the ovary and fallopian tubes, by salpingo-oophorectomy (RRSO) is the most effective ovarian cancer risk reduction method, however it is only available to high-risk women due to the consequential induction of early menopause (Marchetti et al., 2014), and RRSO is too extreme and costly for global risk reduction strategies. Second, hormonal oral contraceptive use is widely established to reduce ovarian cancer risk both in the general population and in high-risk women, conferring an approximate 35% reduction in risk after 5-9 years of use (Torre et al., 2018). Unfortunately, access to oral contraceptives can be limited globally due to socioeconomic and cultural barriers, and uptake has been

suboptimal due to the increased risk of thrombosis and breast cancers with oral contraceptive use (Brynhildsen, 2014; Grindlay et al., 2013). Additionally, the mechanisms of oral contraceptive-mediated risk reduction remain elusive. Numerous mechanisms have been explored in the context of the incessant ovulation hypothesis first posited by Fathalla in 1971 (Fathalla, 2013). These include blocking ovulation-associated wound-repair, reducing inflammation and preventing the engraftment of opportunistic fallopian tube precursor lesions into the ovary during ovulatory wound-repair (Fathalla, 2013; George et al., 2016; Kurman and Shih, 2010; Savant et al., 2018).

Curiously, ovarian cancer incidence increases with age with a median age at diagnosis of 63 years old, numerous years after ovulations have normally ceased at menopause (National Cancer Institute, 2018). This led us to explore if age and ovulations could transform the ovarian microenvironment into a niche that is permissive to ovarian cancer growth. In fact, ovulation requires extensive architectural remodeling of the extracellular matrix (ECM) that was recently shown to result in age-associated stromal ovarian fibrosis in mice (Briley et al., 2016). This fibrosis correlated with a pro-inflammatory cascade with increased F4/80+ macrophage infiltration and proinflammatory chemokines postulated to reduce gamete quality with age (Briley et al., 2016). Over a century ago in 1889, Paget established the ‘seed and soil’ hypothesis upon the observation that some tissues are more prone to cancer metastasis (Langley and Fidler, 2011). Fibrosis has since been established as a fertile ‘soil’ or premetastatic niche (PMN) for cancer metastasis in models of cancer cell colonization of fibrotic lungs, and in fibrotic breast disease (Jacobs et al., 1999; Olaso et al., 1997).

Fibrotic niches provide mechanosensory signals and have a characteristic chronic inflammatory response that provides a cytokine milieu that aids in metastatic invasion and colonization (Cox et al., 2013; Cox and Erler, 2014; Nielsen et al., 2016). Despite long-standing interest in pathological conditions such as polycystic ovarian syndrome (PCOS) where ovarian fibrosis is a hallmark (reviewed in Zhou et al., 2017), the extension of Briley and colleagues' (2016) findings of murine ovarian fibrosis into human aging has yet to be described. Additionally, the ovary is an established pro-tumor niche with up to 30% of cancers discovered in the ovary later found to be metastases from other primary malignancies, commonly from breast, colon, or gastric origin (Bigorie et al., 2010; Li et al., 2012). The reasons why the ovary provides fertile 'soil' for cancer growth remain unknown.

Metformin has been demonstrated to treat and prevent fibrosis in preclinical models of lung, kidney, liver, skin, and heart fibrosis (Choi et al., 2016; Kita et al., 2012; Ursini et al., 2016; M. Wang et al., 2016; Xiao et al., 2010). Metformin activates AMPK that in turn attenuates fibroblast activity largely by suppressing TGF-β production (Cufí et al., 2010; Sato et al., 2016). Interestingly, in a robust retrospective analysis of type 2 diabetic (T2D) women using metformin compared to non-users, metformin users had up to an astonishing 82% reduction in ovarian cancer incidence (Tseng, 2015). This was suggested to be due to the metabolic and possible antiangiogenic activity of metformin, yet no mechanistic studies for this risk-reduction have been explored (Tseng, 2015). This led us to hypothesize that metformin use prevents age-associated ovarian fibrosis, thereby preventing the development of a tumor-permissive PMN and decreasing the risk of ovarian cancer. In this

study we validate the presence of age-associated fibrosis in murine ovaries and extend these findings into a cohort of pre-menopausal and post-menopausal human ovaries with and without metformin use, providing support for a novel hypothesis that mechanistically unifies the non-hereditary ovarian cancer risk factors of age and ovulation.

4.4 Results

4.4.1 Murine age- and ovulation-associated ovarian fibrosis leads to chronic inflammation

We first set out to validate the presence of ovarian fibrosis in aged murine ovaries (Briley et al., 2016). Using a cohort of mice aged from 3-33 months, ovarian stromal collagen content was determined using Masson's trichrome staining (MTS). Ages were batched from 0-12, 12-20, and >20 months old based on histological similarity, with no follicles present in samples >20 months old. Ovarian fibrosis was present in 6/10 ovaries >20 months old (Fig 4-1A,B, 4-2A-C). Interestingly, 4/10 ovaries >20 months old did not exhibit fibrosis, instead exhibiting a collapsed structure with tubular adenomas similar to the *Wv/Wv* model of ovarian aging (Fig. 4-2D) (Smith et al., 2012). To accelerate and model ovarian aging, 4-vinylcyclohexene diepoxide (VCD) was used to induce age-associated changes by destroying ovarian follicles over a 60-day period (Laviolette et al., 2011). No ovarian fibrosis was present in VCD-treated ovaries, and the ovarian stroma exhibited a homogenous phenotype lacking the stromal complexity of naturally aged ovaries (Fig. 4-1A,B, 4-2E), suggesting that ovulations are required to achieve this complexity.

To assess the effect of fibrosis on the ovarian microenvironment, we focused on the >20-month-old ovaries with ovarian fibrosis as assessed by MTS, excluding from further analysis the VCD-treated ovaries and aged ovaries >20 months old with tubular adenomas. To determine if ovarian fibrosis correlates with the infiltration of immune subtypes commonly found in sites of chronic inflammation, immunohistochemical (IHC) detection of CD8, CD4, and FOXP3 was performed (Hou et al., 2017; Lee and Kalluri, 2010; Wang and DuBois, 2015). Enhanced populations of CD8, CD4, and FOXP3+ T cells are present in fibrotic ovaries >20 months old compared to ovaries aged 0-20 months (Fig. 4-1C-H). IDO1 promotes fibrogenesis and immune dysfunction in the tumor microenvironment due to its ability to metabolize tryptophan, an essential mediator of T cell function (Matheus et al., 2017; Munn and Mellor, 2016; Zhong et al., 2017). IDO1 exhibited low ubiquitous expression in ovaries 0-20 months of age, whereas IDO1 stained strongly positive in regions of fibrosis in ovaries >20 months old.

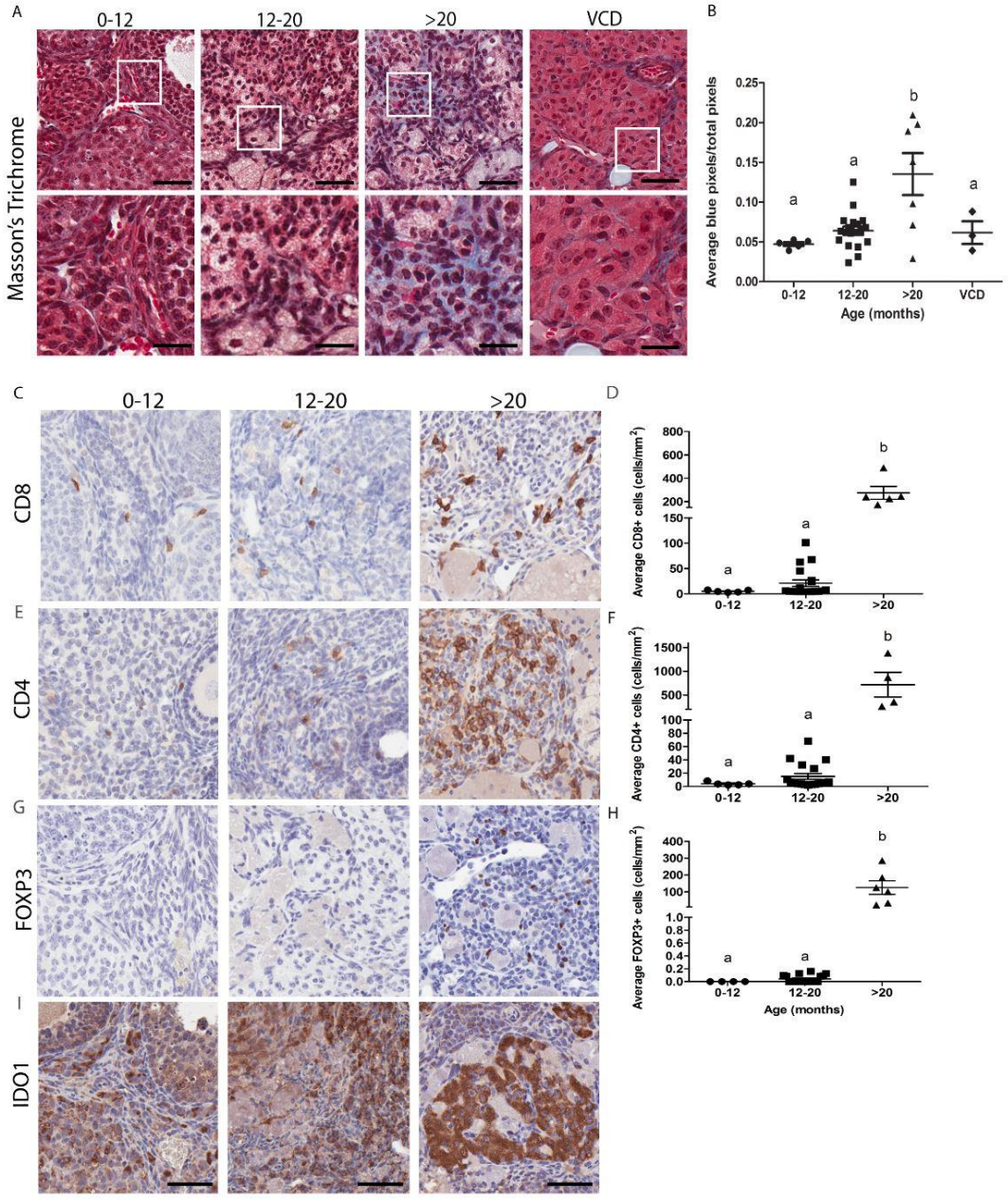

Figure 4-1. Age- and ovulation-associated murine ovarian fibrosis correlates with chronic inflammation. Ovaries were isolated from C57Bl/6 mice over an aging time-course. Ages were batched from 0-12 (N=5), 12-20 (N=19), and >20 (N=7) months. Five-week-old mice were given intraperitoneal injection of 4-vinylcyclohexene diepoxide (VCD, 240 mg/kg) daily for 5 days (N=3) and ovaries collected after two months. (**A**) Representative images of Masson's trichrome staining for each age batch and VCD-treated ovaries. Collagens - blue, erythrocytes and fibrin – red, nuclei – purple. White box indicates region of ovary presented in the lower panel. Upper panel scale bars = 50 µm, lower panel scale bars = 25 µm. (**B**) Quantification of collagen deposition. Total blue pixels (hue value 0.64) were normalized to total pixel counts and averaged within groups. (**C,E,G,I**). Representative images of immunohistochemical detection of CD8, CD4, FOXP3, and IDO1 is presented. Scale bars = 50 µm. (**D,F,H**) Quantification of CD8, CD4, and FOXP3+ cell number normalized to ovarian area. All data represent the average of 3 sections (50 µm apart). One-way ANOVA was used to determine significance with a,b indicating significance between groups.

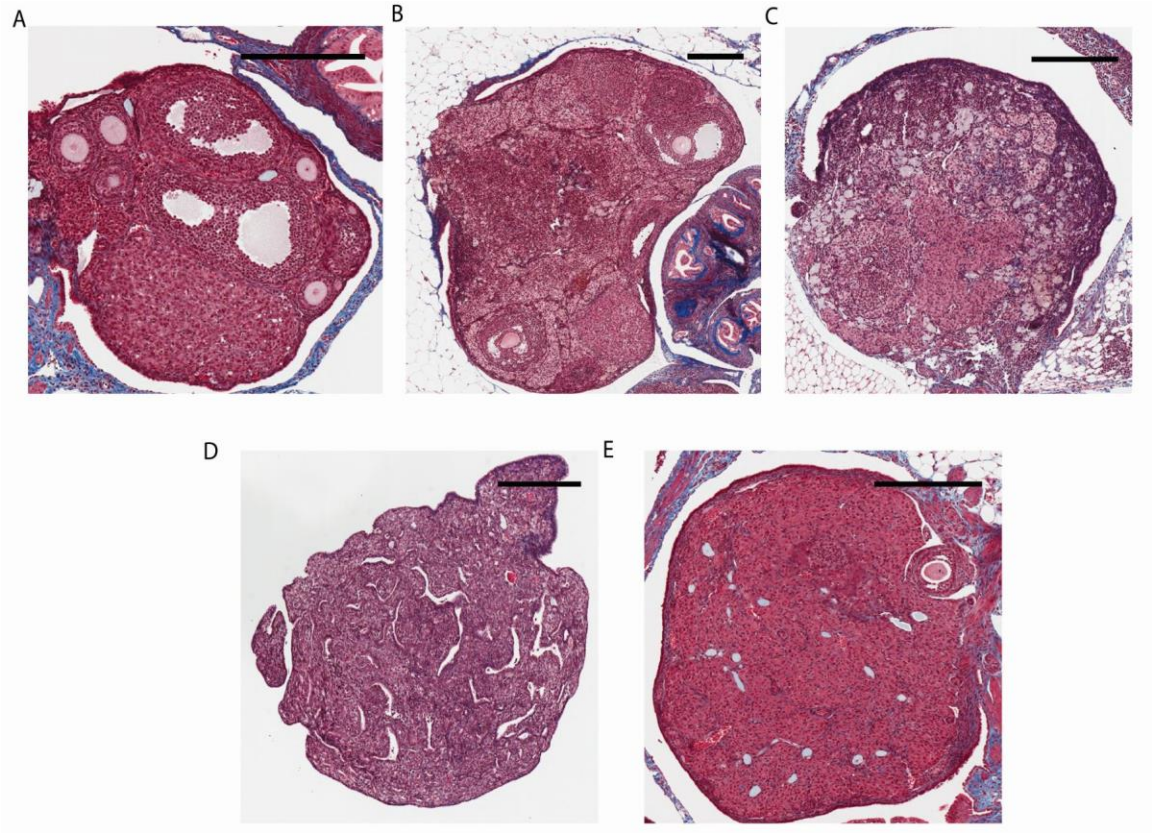

Figure 4-2. Ovarian aging heterogeneity is not replicated by VCD treatment. Representative images of ovarian histology by Masson's trichrome staining of (**A**) 0-12 months, (**B**) 12-20 months, (**C**) >20 months with ovarian fibrosis, (**D**) >20 months without ovarian fibrosis, and (**E**) 60 days post-VCD treated ovaries. Collagens – blue, erythrocytes and fibrin – red, nuclei – purple. All scale bars = 300 μm.

4.4.2 Metformin attenuates age-associated ovarian fibrosis in post-menopausal human ovaries

To determine if ovarian fibrosis also develops during human aging, we obtained a cohort of human ovaries ranging in age from 21-75 years old (Table 4-1). Given the ovarian cancer risk reduction observed with metformin use in T2D women and the role of metformin in regulating fibrosis through AMPK activation (Sato et al., 2016; Tseng, 2015), we also accrued post-menopausal ovaries from patients who were taking metformin for T2D treatment at the time of oophorectomy. Among patients taking metformin, 2/5 patients were also prescribed gliptins that inhibits the enzymatic function of dipeptidyl-peptidase-4 (DPP4) and promotes the action of incretin hormones to improve glycemic control in T2D (Table 4-1) (Sharma et al., 2017; St. Onge et al., 2012).

The analysis focused on the ovarian cortex region underlying the ovarian surface epithelium and tunica albuginea as this region is where epithelial inclusion cysts form (putative sites of cancer origin), and is the likely site of serous-tubal intraepithelial carcinoma (STIC) migration into the ovary in the early stages of ovarian cancer. Classic hematoxylin and eosin (H&E) staining has low resolution for delineating collagen organization with no obvious differences among groups (Fig. 4-3A). Collagen architecture is commonly assessed by the orientation of collagen fibers in relation the each other; when fibers share a similar direction (linearized) they are called anisotropic, a feature of fibrosis. In contrast, collagen fibers in normal tissue form a mesh-like pattern with no discernable shared direction among fibers and are referred to as having isotropic collagen structure. MTS that specifically stains collagens revealed isotropic collagen organization in pre-menopausal ovaries and in post-menopausal ovaries with metformin use (hereafter referred

to as metformin ovaries), characteristic of normal tissue collagen organization (Fig. 4-3B). In contrast, post-menopausal ovaries without metformin use exhibited anisotropic (linearized) collagen architecture (Fig. 4-3B) consistent with both age-related changes in collagen organization that are also characteristic of organ fibrosis (reviewed in (Harper et al., 2018; Ricard-Blum et al., 2018, p.)). Second-harmonic generation (SHG) imaging is a highly sensitive modality to quantify collagen structure at a submicron resolution based on the noncentrosymmetric (a substance lacking symmetrical points of inversion) nature of collagen fibers based on their lack of a symmetrical center (Keikhosravi et al., 2014; Strupler et al., 2007).

To quantify collagen organization, SHG images of the ovarian cortex were used to calculate the coherence of collagen fiber orientation, with increased coherence representing more anisotropic collagen structure while less coherence represents isotropic collagen (Fig. 4-3D). Consistent with the structure revealed by MTS (Fig. 4-3B), pre-menopausal and metformin ovaries have less coherence while post-menopausal ovaries have increased collagen coherence (Fig. 4-3D). These data show that age-associated ovarian fibrosis develops in human ovaries similar to that seen in aged murine ovaries (Fig. 4-1A), which can be remedied by metformin use.

Table 4-1. Human ovary cohort

Group	Patient Number	Age	Number of ovarian samples[a]	OC use[b]	Metformin use	Gliptin use	T2D status
Pre-menopausal	1	45	1	N/A	-	-	-
	2	38	1	N/A	-	-	-
	3	37	2	N/A	-	-	-
	4	48	2	N/A	-	-	-
	5	43	2	N/A	-	-	-
	6	21	1	N/A	-	-	-
	7	28	1	N/A	-	-	-
	8	32	1	+	-	-	-
Post-menopausal	9	58	1	N/A	-	-	-
	10	75	2	N/A	-	-	-
	11	60	1	N/A	-	-	-
	12	54	1	N/A	-	-	-
	13	55	1	N/A	-	-	-
Post-menopausal + metformin use	14	68	2	N/A	+	-	+
	15	69	3	N/A	+	+	+
	16	67	2	N/A	+	-	+
	17	71	2	N/A	+	+	+
	18	53	4	N/A	+	-	+

[a]Cases with ≥ 2 samples indicate normal ovarian tissue from both right and left ovaries was profiled.
[b]'N/A' indicates information not available

4.4.3 Fibrosis, menopause, and metformin use stratifies ovarian cortex gene expression

We next determined if ovarian fibrosis correlates with altered gene expression in the ovarian cortex. RNA was isolated from the human ovarian cortex using automated microdissection (Fig. 4-4). Isolated RNA was run on Nanostring PanCancer Immune Profiling arrays that contain 770 immune regulatory genes, including genes that are involved in regulating the stromal microenvironment such as *TGFβ* and fibronectin (*FN1).* Unsupervised hierarchical clustering stratified pre-menopausal and post-menopausal ovaries almost entirely (Fig. 4-5). All but one pair of samples derived from contralateral ovaries within the same patient clustered together, highlighting low intra-patient variability in immune-related RNA expression. Interestingly, within the post-menopausal cluster, metformin ovaries clustered independently from post-menopausal ovaries not using metformin. These clusters were also consistent with fibrotic status as determined by MTS and SHG imaging (Fig. 4-3), with metformin ovaries and 7/9 pre-menopausal ovaries lacking fibrosis. In contrast, 5/6 post-menopausal ovaries were fibrotic and clustered independently of both pre-menopausal and metformin ovaries (Fig. 4-5). Among the two pre-menopausal ovaries that clustered with post-menopausal ovaries, both exhibited linearized collagen by SHG (patient 1 and 2).

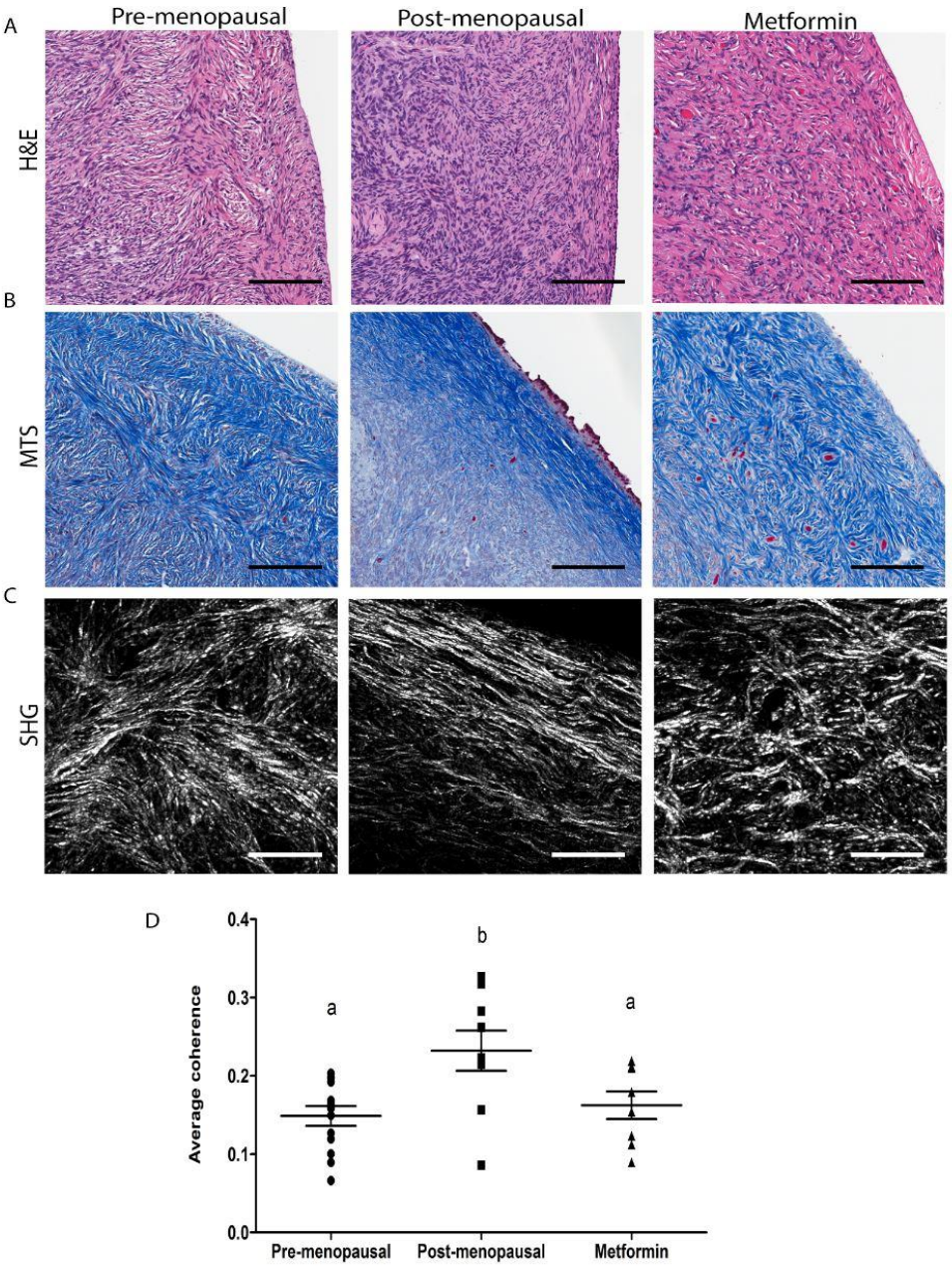

Figure 4-3. Metformin use abrogates age-associated fibrosis. All images presented are representative of each group. (**A**) Hematoxylin and eosin (H&E) staining of human ovarian cortex among groups. (**B**) Masson's trichrome staining of human ovarian cortex with collagens - blue, erythrocytes and fibrin – red, and nuclei – purple. (**A,B**) Scale bars = 125 µm. (**C**) Second-harmonic generation microscopy of human ovarian cortex in serially sectioned tissue. Scale bars = 63.5 µm. (**D**) Quantification of collagen anisotropy. Coherence of collagen fiber directionality was determined using the OrientationJ plugin on ImageJ software. Two SHG images per sample were averaged and groups averages are presented, pre-menopausal (N = 13), post-menopausal (N = 9), and metformin (N = 8). One-way ANOVA with Tukey's posttest was used to determine significance with a,b indicating significance between groups.

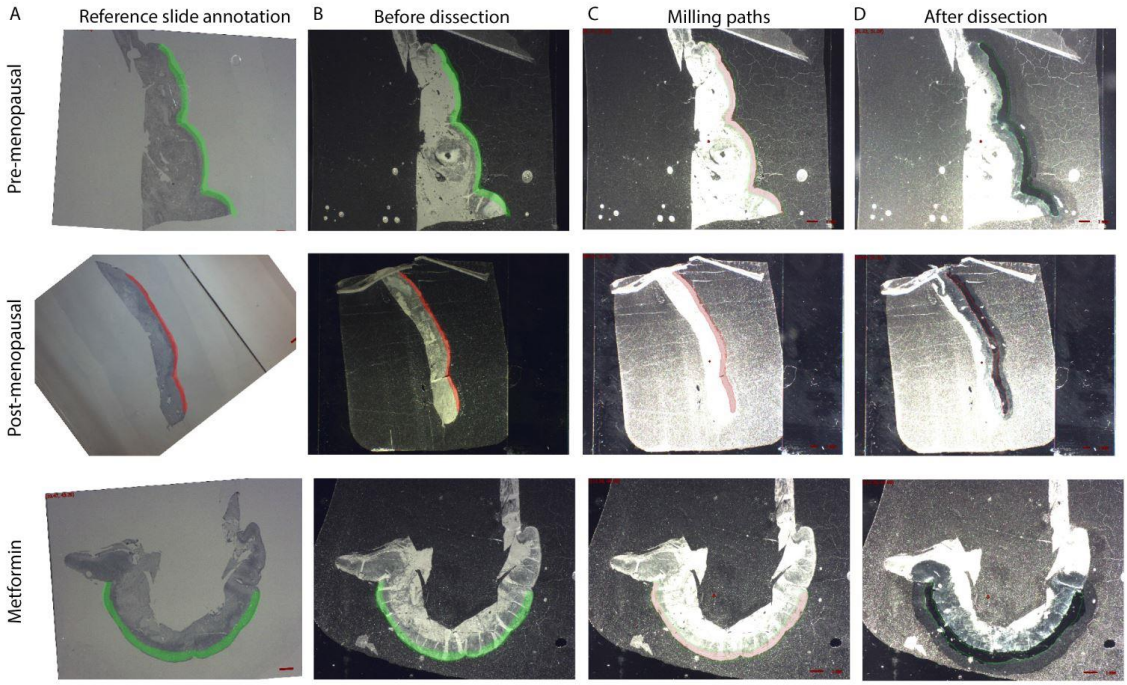

Figure 4-4. Automated microdissection of the human ovarian cortex. Representative images of ovarian cortex microdissection among groups. (**A**) Annotated hematoxylin stained reference slide. (**B**) Annotated unstained serial section before microdissection. (**C**) Automated milling path during tissue collection. (**D**) Tissue remaining following sample collection.

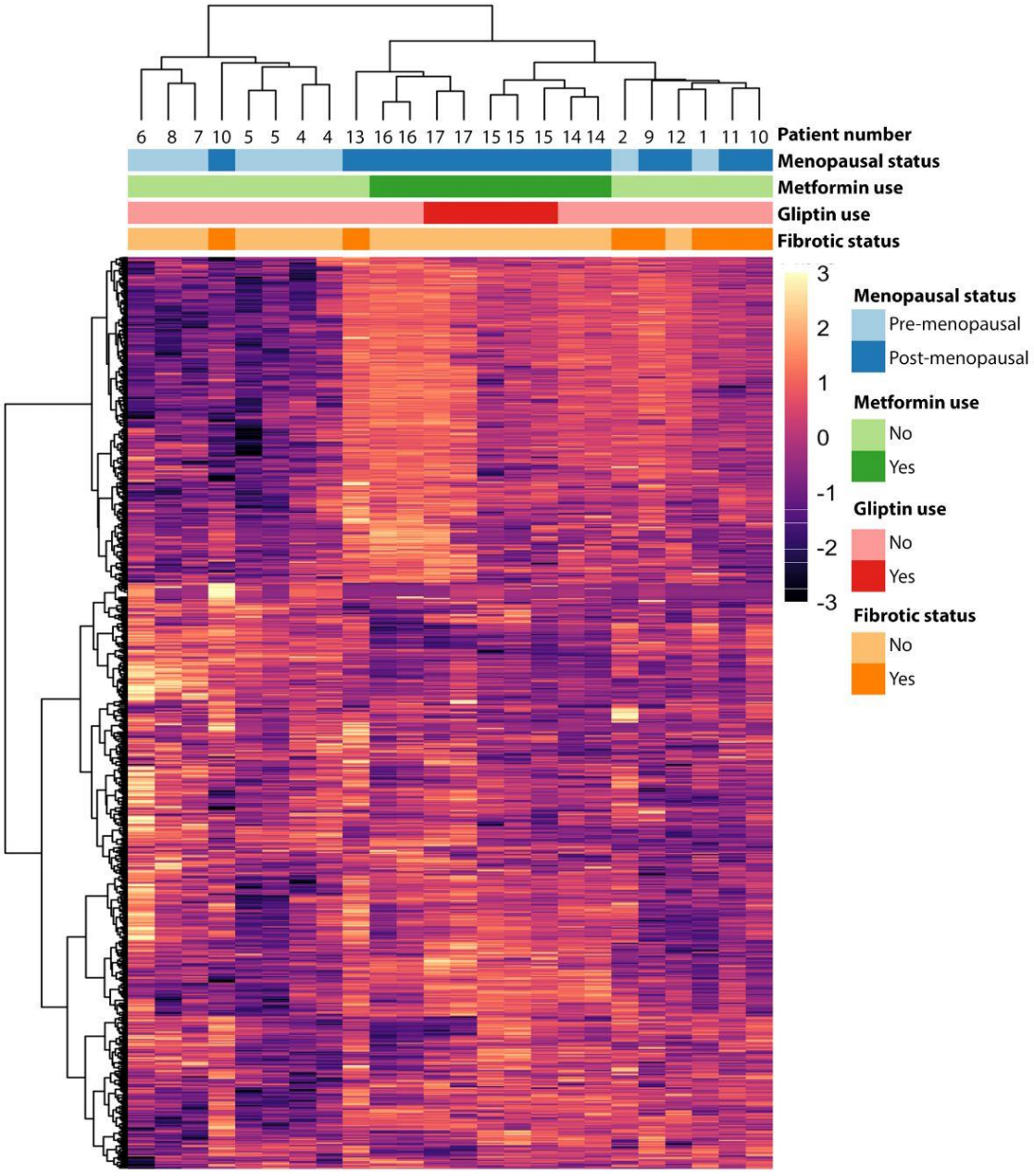

Figure 4-5. Menopausal status, metformin use, and fibrosis stratify ovarian cortex gene expression profiles. Unsupervised hierarchical clustering of individual patient samples of pre-menopausal (N=11), post-menopausal (N=6), and metformin (N=9) ovaries is presented. Normalized RNA expression values were log2 transformed and housekeeping genes omitted. Patients numbers and annotations for menopausal status, metformin use, and gliptin use correspond to Table 1. Fibrotic status was determined histologically by Masson's trichrome staining and collagen fiber coherence by SHG imaging.

4.4.4 Metformin use regulates pro-fibrotic and complement pathway gene expression

We next aimed to determine if ovarian fibrosis leads to inflammation and tumor-permissive gene expression signatures characteristic of PMNs. For differential gene expression analysis of the Nanostring Immune Signaling array dataset, samples were grouped according to fibrotic status and metformin use as indicated in Figure 4-5, with non-fibrotic referring to 7/9 pre-menopausal and 1/6 post-menopausal samples (N=8), fibrotic referring to 2/9 pre-menopausal samples and 5/6 post-menopausal samples (N=7), and metformin referring to all nine metformin ovaries lacking fibrosis (N=9). The top 30 up- and downregulated genes in all pairwise comparisons are presented in (Fig. 4-6). In metformin ovaries compared to either fibrotic or non-fibrotic ovaries, *DPP4* was the most downregulated gene while *ARG2* was the most upregulated gene, suggesting these genes are key targets of metformin activity. Interestingly, 5/9 ovarian samples in the metformin group were from patients also taking DPP4 inhibitors (gliptins). In addition to the effect of DPP4 inhibition on incretin hormones, DPP4 has also been identified as a marker of a hyperactive pro-fibrotic fibroblasts (Rinkevich et al., 2015) suggesting gliptin use may inhibit pro-fibrotic processes. Gliptins function to inhibit the enzymatic function of DPP4 and not transcription (Demuth et al., 2005). Consistent with this, when differential gene expression analysis was performed omitting samples with gliptin use, DPP4 was still among the most downregulated gene in metformin ovaries (Fig. 4-7) suggesting DPP4 downregulation is an effect of metformin and not solely an effect of gliptin, though synergy may occur.

Venn diagrams representing uniquely or shared up- and downregulated genes among all pairwise comparisons are presented with 144 upregulated and 30 downregulated genes in fibrotic vs. non-fibrotic ovaries, 262 upregulated and 55 downregulated genes in metformin vs. non-fibrotic ovaries, and 67 upregulated and 49 downregulated genes in metformin vs. fibrotic ovaries (Fig. 4-8A). Up to 10 significant GO terms among all pairwise comparisons are presented (Fig. 4-8B,C) with genes called for each GO term presented in Tables 4-2, 4-3, 4-4. Cellular response to IFNγ, lymphocyte chemotaxis, and negative regulation of IL10 production are upregulated in fibrotic ovaries (Fig. 4-8B), while downregulated terms in fibrotic ovaries include regulation of signal transduction by p53, stress-activation of MAPK cascade and DNA-templated transcription, in comparison to non-fibrotic ovaries (Fig. 4-8C). Similar to fibrotic ovaries, immune response, inflammatory response, chemotaxis, and negative regulation of IL10 production are upregulated in metformin compared to non-fibrotic ovaries suggesting a similar inflammatory environment is present in both fibrotic and metformin ovaries which largely encompass all post-menopausal samples (Fig. 4-8B). Downregulated GO terms in metformin vs. non-fibrotic ovaries include peptide cross-linking, sprouting angiogenesis, platelet degranulation, and complement activation (Fig. 4-8C). Compared to fibrotic ovaries, metformin ovaries have elevated expression of genes associated with bacterial response and cytokine secretion, as well as reduced expression of wound response and cysteine-type endopeptidase activity genes (Fig. 4-8B,C). Intriguingly, among genes downregulated in both pairwise comparisons with metformin use, *FN1, DPP4*, and *TGFβ2* are known to promote fibrosis and contribute to PMN formation (Cox and Erler, 2014; Rinkevich et al., 2015). In addition, numerous complement pathway proteins are downregulated in metformin ovaries

including *C2 and C3* that have been implicated in promoting both fibrosis and PMN formation (Boire et al., 2017; Danobeitia et al., 2014; Fisher et al., 2017; Tang et al., 2009). These data are suggestive of pro-inflammatory signaling in both fibrotic and metformin ovaries in comparison to non-fibrotic ovaries, yet there is a downregulation of genes implicated in fibrosis and premetastatic niche formation with metformin use.

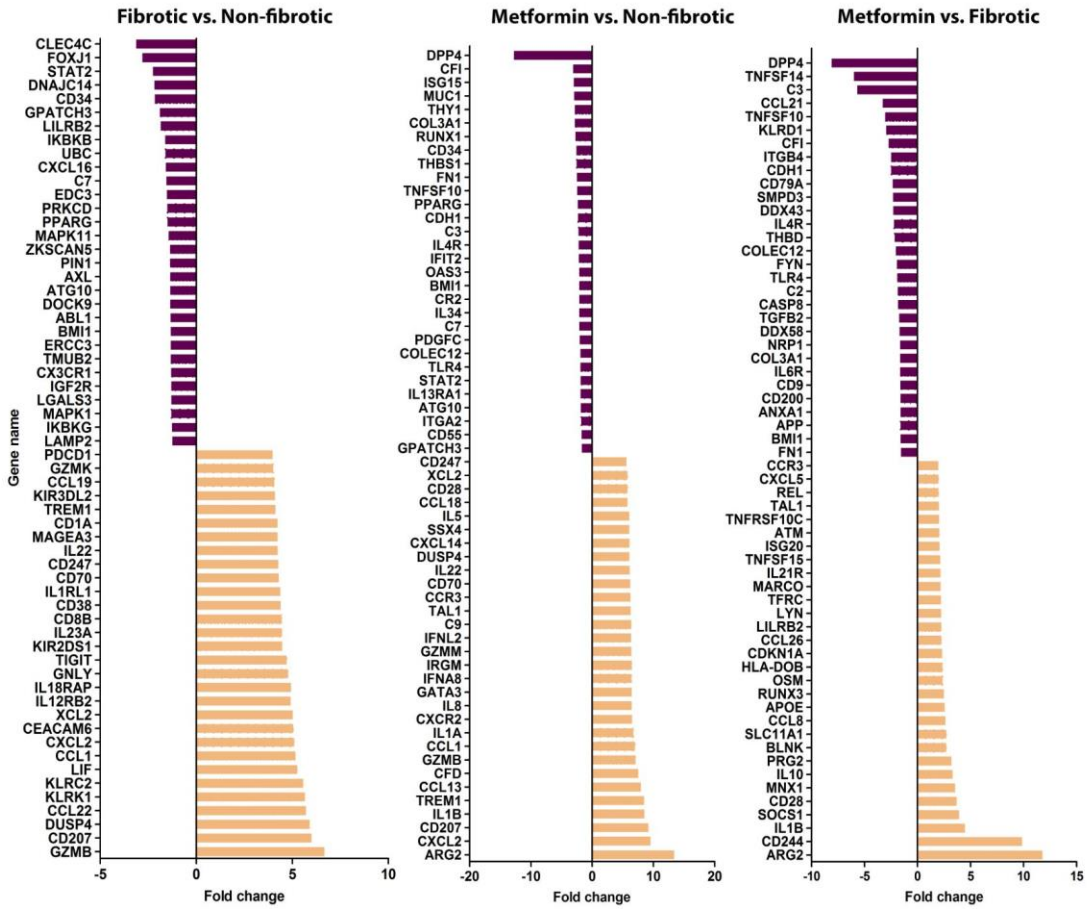

Figure 4-6. Differential gene expression in the non-fibrotic, fibrotic, and metformin ovarian cortex. Fold changes of the top 30 upregulated and downregulated genes among all pairwise comparisons are presented. All fold changes reach statistical significance with $p<0.05$ by student's t-test.

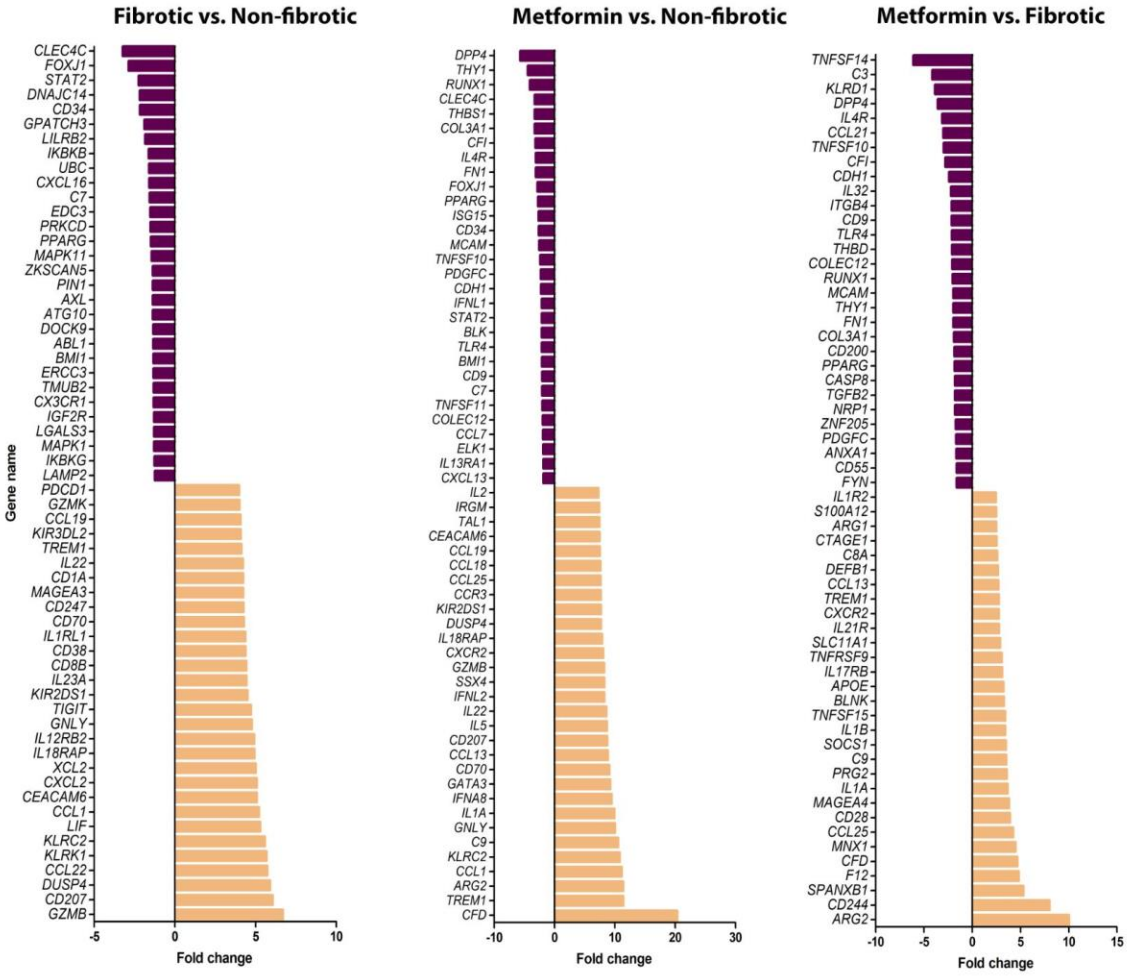

Figure 4-7. Differential gene expression in non-fibrotic, fibrotic, and metformin ovaries with samples having noted gliptin use omitted. Fold changes of the top 30 upregulated and downregulated genes among all pairwise comparisons are presented. All fold changes reach statistical significance with $p<0.05$ by student's t-test.

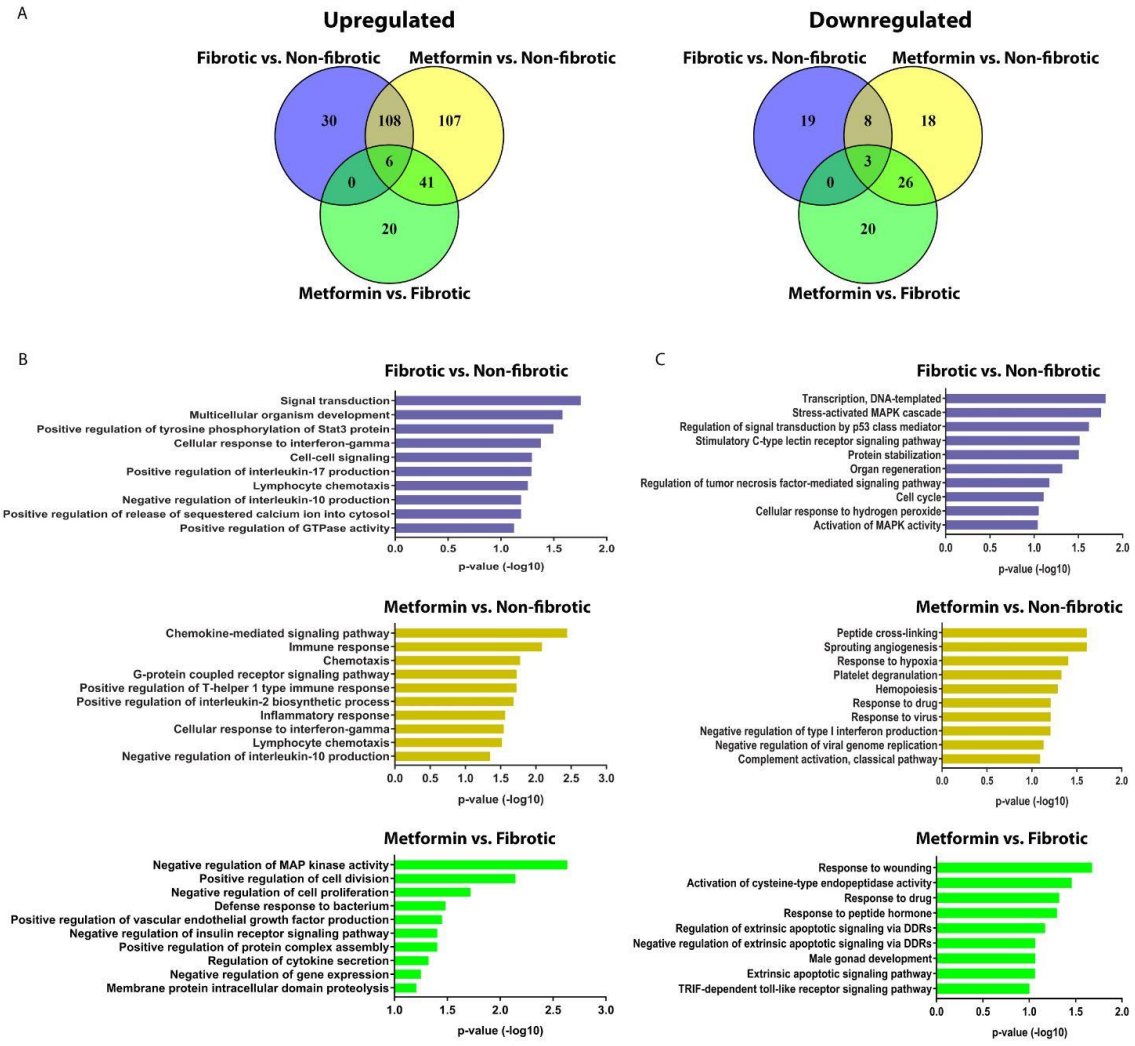

Figure 4-8. GO term analysis of differential gene expression in the non-fibrotic, fibrotic and metformin ovarian cortex.(**A**) Venn diagrams depicting the number of shared or uniquely up- and downregulated regulated genes in all pairwise comparisons. (**B**) Upregulated and (**C**) downregulated GO terms in all pairwise comparisons.

Table 4-2. Gene ontology features in fibrotic vs. non-fibrotic human ovaries

Gene expression	GO reference	Term	Genes called for GO term	p-Value (-log10)
Upregulated	GO:0007165	Signal transduction	*CCL1, CCL11,CCL13, CCL18, CCL22, CCR6, CD274, CD38, CD48, CD70, CD79B, CD83, CEACAM6, CREBP, CSF1R, CSF2RB, CXCL10, CXCL14, CXCL9, FAS, GATA3, IL13, IL15, IL1RL1, IL2RB, IL5RA, ISOCLG, ITGAL, KLRC2, KLRK1, MAP2L1, MST1R, PDCD1, SH2B2, TNFRSF10B, TNFRSF17, TNFRSR18, TNFSF8, TPTE, XCL2*	1.75642
	GO:0007275	Multicellular organism development	*CCL17, CSF1R, CSF3, LIF, PDCD1, PMCH, TBX21, TNFRSF10B, TNFRSF17, TNFRSF18*	1.582858
	GO:0042517	Positive regulation of tyrosine phosphorylation of Stat3 protein	*CSF1R, IL6R, IL12B, IL15, IL23A, IL23R, IL24, LIF*	1.495848
	GO:0071346	Cellular response to interferon-gamma	*CCL1, CCL11, CCL13, CCL16, CCL17, CCL18, CCL19, CCL22, CD58, IL12B, XCL2*	1.379461
	GO:0007267	Cell-cell signaling	*CCL13, CCL16, CCL17, CCL18, CCL22, CCL27, CD70, CD80, CEACAM6, CXCL10, CXCL14, CXCL9, IL13, IL15, IL2, IL22, IL3, TNFSF8*	1.293574
	GO:0032740	Positive regulation of interleukin-17 production	*IL2, IL12B, IL15, IL23A, IL23, SLAMF6*	1.290533
	GO:0048247	Lymphocyte chemotaxis	*CCL1, CCL13, CCL11, CCL16, CCL17, CCL18, CCL19, CCL2, XCL2*	1.255956
	GO:0032693	Negative regulation of interleukin-10 production	*CD274, FOXP3, IL12B, IL23A, IL23R*	1.191897
	GO:0051281	Positive regulation of release of sequestered calcium ion into cytosol	*BAX, CXCR3, CXCL9, CXCL10, IL13*	1.191897
	GO:0043547	Positive regulation of GTPase activity	*CCL1, CCL11, CCL13, CCL16, CCL17, CCL18, CCL19, CCL22, CSF2RB, IL2, IL2RB, IL3, IL5, IL5RA, XCL2*	1.124605
Downregulated	GO:0006351	Transcription, DNA-templated	*BMI1, IKBKG, MAPK1, MAPK11, PPARG, STAT2, ZKSCAN5*	1.807456
	GO:0051403	Stress-activated MAPK cascade	*IKBKG, IKBKB, UBC*	1.756135
	GO:1901796	Regulation of signal transduction by p53 class mediator	*MAPK11, PIN1, UBC*	1.619837

	GO:0002223	Stimulatory C-type lectin receptor signaling pathway	*CLEC4C, IKBKB, IKBKG, PRKCD, UBC*	1.514197
	GO:0050821	Protein stabilization	*LAMP2, PIN1, PRKCD*	1.504708
	GO:0031100	Organ regeneration	*AXL, IGF2R, PPARG*	1.318213
	GO:0010803	Regulation of tumor necrosis factor-mediated signaling pathway	*IKBKB, IKBKG, UBC*	1.171359
	GO:0007049	Cell cycle	*MAPK1, PIN1, PRKCD*	1.108516
	GO:0070301	Cellular response to hydrogen peroxide	*ABL1, AXL, PRKCD*	1.051255
	GO:0000187	Activation of MAPK activity	*IKBKG, MAPK1, MAPK11, UBC*	1.04166

Table 4-3. Gene ontology features in metformin vs. non-fibrotic human ovaries

	GO reference	Term	Genes called for GO term	p-Value (-log10)
Upregulated	GO:0070098	Chemokine-mediated signaling pathway	*CCL1, CCL13, CCL16, CCL17, CCL18, CCL19, CCL22, CCL23, CCL25, CCL26, CCL3, CCL3L1, CCL8, CCR1, CCR2, CCR3, CCR9, CXCL2, CXCL3, CXCL5, CXCL8, CXCL9, CXCR1, CXCR2, CXCR4, CXCR6, XCL2, XCR1*	2.444758
	GO:0006955	Immune response	*AIRE, C8A, C8B, C9, CCL13, CCL16, CCL18, CCL19, CCL22, CCL23, CCL25, CCL26, CCL3, CCL8, CCR1, CCR2, CCR9, CD1A, CD1E, CD27, CD274, CD36, CD70, CD79B, CD86, CD8A, CD8B, CEACAM8, CEBPB, CFP, CSF2, CSF3, CTSG, CTSW, CXCL14, CXCL2, CXCL3, CXCL5, CXCL8, CXCL9, DEFB1, FCGR1A, GZMA, HLA-A, HLA-dob, ICOS, IFITIM2, IGLL1, IL10, IL13, IL15, IL18RAP,IL1A, IL1B, IL1R2, IL1RL1, IL1RN, IL2, IL21, IL22, IL24, IL3, IL5, IL7, IL7R, ILR10, LTA, LTB, MR1, NOTCH1, OSM, PRG2, PTGDR2, SLC11A1, TCF7, TNFRSF10B, TNFRSF18, TNFRSF4, TNFRSF9, TNFSF15, TNFSF8, ZAP70*	2.0882
	GO:0006935	Chemotaxis	*C5, CCL1, CCL16, CCL17, CCL18, CCL22, CCL23, CCL25, CCL26, CCL3, CCL8, CCR1, CCR2, CCR3, CCR9, CXCL14, CXCL2, CXCL5, CXCL8, CXCL9, CXCR1, CXCR3, CXCR4, CXCR6, DEFB1, FPR2, MAP2K1, PTGDR2, XCR1*	1.776891
	GO:0007186	G-protein coupled receptor signaling pathway	*APOE, C5, CCL1, CCL16, CCL18, CCL19, CCL22, CCL23, CCL25, CCL26, CCL3, CCL3L1, CCL8, CCR2, CCR9, CD3E, CXCL2, CXCL3, CXCL5, CXCL8, CXCL9, CXCR1, CXCR3, CXCR4, CXCR6, DEFB1, FPR2, PTGDR2, XCL2, XCR1*	1.727537
	GO:0002827	Positive regulation of T-helper 1 type immune response	*CCR2, IL12B, IL12RB1, IL23A, IL23R, SLC11A1*	1.725889
	GO:0045086	Positive regulation of interleukin-2 biosynthetic process	*CD28, CD3E, CD80, CD86, CARD11, IL1A, IL1B, IRF4*	1.681017

	GO:0006954	Inflammatory response	*C5, CCL1, CCL13, CCL16, CCL17, CCL18, CCL19, CCL22, CCL23, CCL25, CCL26, CCL3, CCL3L1, CCL8, CCR1, CCR2, CCR3, CD27, CEBPB, CRP, CSF1, CSF1R, CXCL2, CXCL3, CXCL5, CXCL8, CXCL9, CXCR1, CXCR2, CXCR3, CXCR4, CXCR6, FPR2, HAVCR2, IL10, IL13, IL15, IL17F, IL18RAP, IL1A, IL1B, IL22, IL23A, IL23R, IL24, IL25, IL27, IL5, IRGM, ITGAL, MAPKAPK2, MEFV, REL, RIPK2, SLC11A1, S100A12, TGFB1, TICAM2, TLR10, TLR5, TLR7, TLR9, TNFAIP3, TNFRSF10B, TNFRSF4, TNFRSF18, TNFRSF9, XCL2, XCR1, ZAP70*	1.563413
	GO:0071346	Cellular response to interferon-gamma	*CCL1, CCL13, CCL16, CCL17, CCL18, CCL19, CCL22, CCL23, CCL25, CCL26, CCL3, CCL3L1, CCL8, CD58, IL12B, IL12RB1, XCL2*	1.543504
	GO:0048247	Lymphocyte chemotaxis	*CCL1, CCL13, CCL16, CCL17, CCL18, CCL19, CCL22, CCL23, CCL25, CCL26, CCL3, CCL3L1, CCL8, XCL2*	1.519449
	GO:0032693	Negative regulation of interleukin-10 production	*CD274, FOXP3, IL12B, IL23A, IL23R, JAK3, PRG2*	1.348443
Downregulated	GO:0018149	Peptide cross-linking	*ANXA1, FN1, THBS1*	1.610091
	GO:0002040	Sprouting angiogenesis	*ENG, NRP1, THBS1*	1.610091
	GO:0001666	Response to hypoxia	*DPP4, ENG, ITGA2, MUC1, TGFB2, THBS1*	1.404744
	GO:0002576	Platelet degranulation	*APP, CD9, FN1, TGFB2, THBS1*	1.330462
	GO:0030097	Hemopoiesis	*BMI1, CD34, IFI6, TGFB2*	1.291107
	GO:0042493	Response to drug	*ANXA1, CDH1, FYN, ITGA2, PPARG, TGFB2, THBS1*	1.210507
	GO:0009615	Response to virus	*DDX58, IFIH1, IFIT1, IFIT2, IKBKG, OAS3, TNFSF4*	1.210507
	GO:0032480	Negative regulation of type I interferon production	*DDX58, IFIH1, IKBKG, ISG15*	1.207079
	GO:0045071	Negative regulation of viral genome replication	*IFI16, IFIT1, ISG15, OAS3*	1.130815
	GO:0006958	complement activation, classical pathway	*C3, C7, CD55, CF1, CR2*	1.092056

Table 4-4. Gene ontology features in metformin vs. fibrotic human ovaries

Gene expression	GO reference	Term	Genes called for GO term	p-Value (-log10)
Upregulated	GO:0043407	Negative regulation of MAP kinase activity	*APOE, IL1B, LYN, PRKCD*	2.635516
	GO:0051781	Positive regulation of cell division	*IL1B, OSN, TAL1, TGFB1, VEGFA*	2.144932
	GO:0008285	Negative regulation of cell proliferation	*ADORA2A, CDKN1A, IL1B, IL10, IFITM1, LYN, OSM, NOTCH1, TGFB1*	1.720519
	GO:0042742	Defense response to bacterium	*IL10, IRF8, MICA, PRG2, PRKCD, SLC11A1, TLR5, TLR9*	1.482619
	GO:0010575	Positive regulation of vascular endothelial growth factor production	*C5, IL1, RORA, TGFB1*	1.450775
	GO:0046627	Negative regulation of insulin receptor signaling pathway	*IL1B, PRKC, SOCS1,*	1.405206
	GO:0031334	Positive regulation of protein complex assembly	*TAL1, TGFB1, VEGFA*	1.405206
	GO:0050707	Regulation of cytokine secretion	*LYN, SOCS1, TLR, TLR9,*	1.323055
	GO:0010629	Negative regulation of gene expression	*CD28, CDKN1A, NFKB1, REL, TBK1, TGFB1*	1.250236
	GO:0031293	Membrane protein intracellular domain proteolysis	*NFKB1, PSEN2, TGFB1*	1.20802
Downregulated	GO:0009611	Response to wounding	*FN1, ITGB4, NRP1, TGFB2*	1.678606
	GO:0097202	Activation of cysteine-type endopeptidase activity	*CASP8, CYFIP2, IFI16*	1.457951
	GO:0042493	Response to drug	*ANXA1, BCL2, CDH1, FYN, PPARG, STAT1, TGFB2*	1.323371
	GO:0043434	Response to peptide hormone	*AXNA1, CD55, STAT1*	1.299618
	GO:1902041	Regulation of extrinsic apoptotic signaling pathway via death domain receptors	*CASP8, FAS, TNFSF10*	1.171165
	GO:1902042	Negative regulation of extrinsic apoptotic signaling pathway via death domain receptors	*CASP8, FAS, TNFSF10*	1.063818
	GO:0008584	Male gonad development	*BCL2, TGFB2, TNFSF10*	1.063818
	GO:0097191	Extrinsic apoptotic signaling pathway	*CASP8, FAS, IL6R, TGFB2*	1.061114
	GO:0035666	TRIF-dependent toll-like receptor signaling pathway	*CASP8, IRF7, IKBKE, TLR4*	1.001128

4.4.5 Metformin alters the ovarian immune landscape

Given the increase in pro-inflammatory gene expression in both fibrotic and metformin ovaries, we next sought to profile the immune landscape of the ovarian cortex and validate gene expression signatures related to fibrotic signaling. Estimation of immune cell type abundance was performed using the Nanostring nSolver cell type prediction algorithm that assigns gene sets to specific immune subsets (annotations provided in Table 4-5). Cell types predicted to significantly change among non-fibrotic, fibrotic, and metformin ovaries include CD8 T cells, regulatory T cell (Tregs), γδ T cells, B cells, aDCs, NK CD56 bright cells, M1 macrophages, and Eosinophils (Fig 4-9A), while CD45, total T cells, T helper, Th1, Th2, effector memory T cells (Tem), central memory T cells (Tcm), Th17, total dendritic cells (DCs), induced DCs, total natural killer (NK) cells, CD56dim NK cells, M2 macrophages, neutrophils, and mast cells were predicted to be unchanged in abundance (Fig. 4-10).

Due to the role of macrophages in promoting tissue remodeling and repair (reviewed in (Lech and Anders, 2013)), along with metformin ovaries predicted to have increased M1 macrophage abundance (Fig. 4-9A) we sought the validate the ratio of M2:M1 macrophages. M1 macrophages promote early inflammation during a wound healing response and contribute to functional immunosurveillance, while alternatively activated immunosuppressive M2 macrophages promote wound healing and resolution, but can also promote PMN formation (Lech and Anders, 2013; Quatromoni and Eruslanov, 2012; Sousa and Määttä, 2016). Additionally, chronic inflammation and unhealed wounding can stabilize M2 polarization leading to enhanced fibrogenesis (Braga et al., 2015). Using IHC

detection of M2 marker CD206 (MRC1) and pan-macrophage marker CD68, fibrotic ovaries were found to have an increased CD206:CD68 ratio compared to both non-fibrotic and metformin ovaries, showing ovarian fibrosis correlates with enhanced M2 polarization (Fig. 4-9A-C). In contrast, metformin promoted M1 polarization as shown by a decrease in the CD206:CD68 ratio (Fig. 4-9A-C). To parallel murine aging, we next validated the abundance of CD8+ T cells as they were predicted to increase in fibrotic and metformin ovaries. Surprisingly, fibrotic ovaries had increased CD8+ T cell infiltration while metformin ovaries had similar levels to non-fibrotic ovaries (Fig. 4-9D,E), showing that metformin use abrogates features of chronic inflammation in post-menopausal ovaries. In contrast, FOXP3+ Tregs were predicted to be upregulated in fibrotic and metformin ovaries, though no significant differences were found among groups (Fig. 4-10).

4.4.6 Metformin and gliptin use abrogates fibroblast activation in post-menopausal ovaries

Given the downregulation of *DPP4* in metformin ovaries (Fig. 4-6) and recent evidence that DPP4+ fibroblasts are pro-fibrotic (Rinkevich et al., 2015), we sought to determine the effect of metformin use on DPP4+ fibroblasts in the ovarian cortex. Using double IHC detection of DPP4 and fibroblast marker αSMA, fibrotic ovaries have increased DPP4+αSMA+ fibroblasts compared to non-fibrotic ovaries (Fig. 4-9F,G). There was no decrease in DPP4+αSMA+ fibroblasts in metformin ovaries compared to fibrotic ovaries (p-value = 0.15 by one-way ANOVA, Fig. 4-9F,G). However, within the metformin group, samples from patients with combined metformin and gliptin use (Table 4-1, patients 15 and 17) had a significant reduction in DPP4+αSMA+ fibroblasts when compared to fibrotic ovaries (Fig. 4-9F,G). This data further supports the development of ovarian fibrosis in

post-menopausal ovaries and suggests that combined metformin and gliptin use may synergistically abrogate ovarian fibrosis.

Table 4-5. Gene annotations used to generate cell type scores

Cell Type	Gene
aDC	LAMP3
	CCL1
	OAS3
	EBI3
	IDO1
B-cells	CR2
	TNFRSF17
	MS4A1
	BLK
	HLA-DOB
	CD19
CD45	PTPRC
CD8 T cells	GZMM
	FLT3LG
	PRF1
	CD8B
	CD8A
DC	CCL17
	CCL22
	CCL13
	CD209
	HSD11B1
Eosinophils	SMPD3
	IL5RA
	PTGDR2
	CCR3
	THBS1
GammaDelta T	FEZ1
	CD160
	TARP
iDC	SYT17
	CD1B
	CD1A
	CD1E
	F13A1
M1	APOE
	SOCS1
	NOS2
	MARCO
	CD68
M2	MRC1
	TGFB1
	IL10
	IRF5
	TGFB2
	ARG1
Mast cells	CTSG
	PRG2
	CMA1
	MS4A2
	TPSAB1
	KIT
Neutrophils	CSF3R
	FPR2
	MME
NK CD56bright	PLA2G6
	MPPED1
	FOXJ1
	RRAD
NK CD56dim	GZMB
	GTF3C1
	IL21R
NK cells	NCR1
	ZNF205
	BCL2
	FUT5
T helper cell	CD28
	BATF
	NUP107
	ANP32B
	ICOS
T-cells	CD3E
	CD2
	CD3G
	CD6
Tcm	ATM
	REPS1
	USP9Y
	NEFL
	DOCK9
Tem	NFATC4
	AKT3
	LTK
	EWSR1
	CCR2
Th1 cells	CD38
	IFNG
	STAT4
	CTLA4
	LTA
	CSF2
	TBX21
	IL12RB2
Th17 cells	IL17RA
	RORC
	IL17A
Th2 cells	LAIR2
	STAT6
	IL26
	CXCR6
	GATA3
	SMAD2
	PMCH
Treg	FOXP3

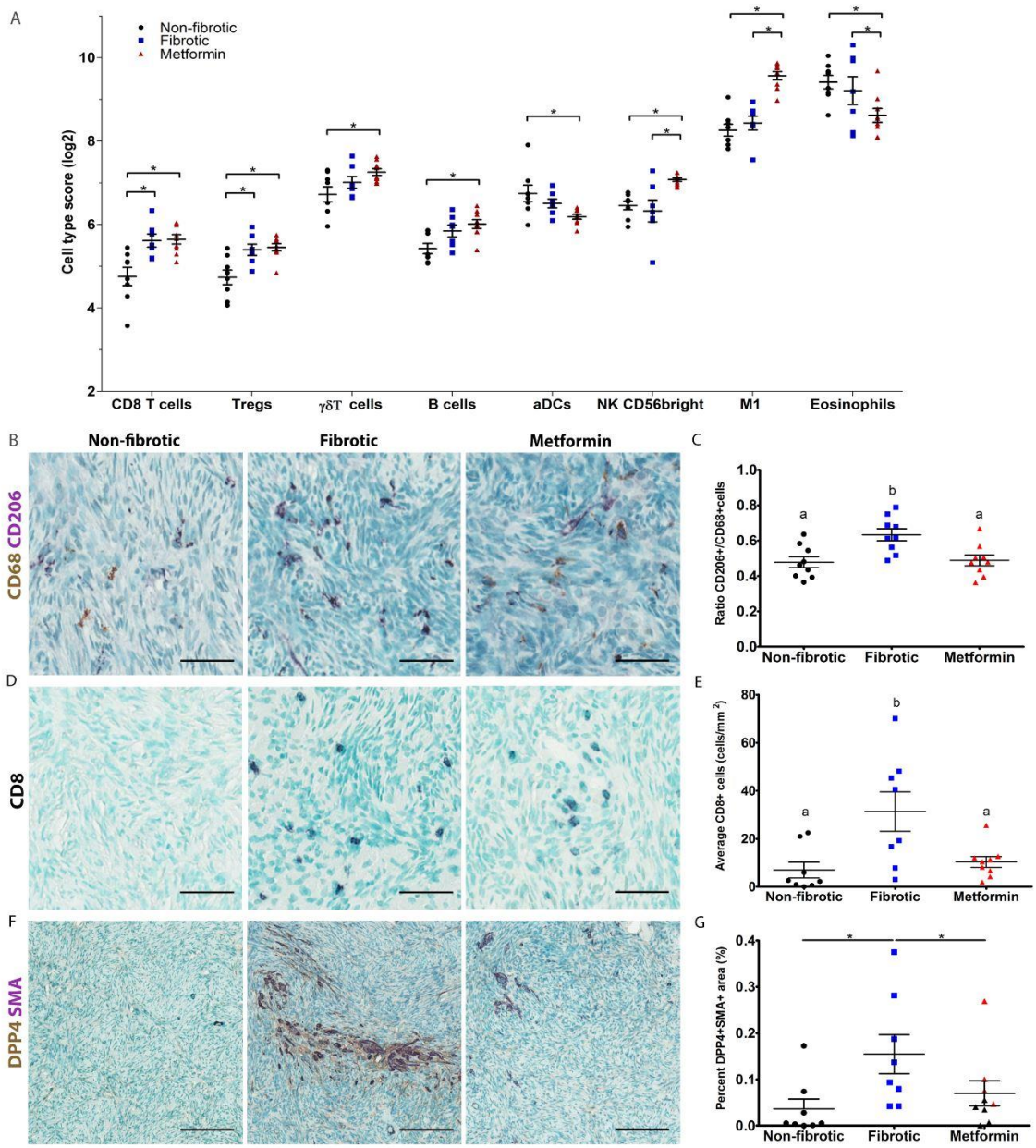

Figure 4-9. Metformin use alters the immune and stromal landscape of the ovarian cortex. (**A**) Immune cell type prediction. Cell type scores were derived using the cell type profiling algorithm on Nanostring nSolver software for non-fibrotic (N=8), fibrotic (N=7), and metformin (N=9) ovaries. Average log-scale expression based on a modified Pearson's correlation coefficient of cell type-specific gene sets is presented. Two-way ANOVA with Tukey's posttest was used to determine significance with *p<0.05. (**B**) Double immunohistochemical detection of pan-macrophage marker CD68 (brown), and M2 macrophage marker CD206 (purple). (**C**) Quantification of the ratio of CD206+ cells/CD68+ cells. Total cell counts for CD206 and CD68 were normalized to tissue area (mm^2) and the ratio of CD206+/CD68+ cells is presented. (**D**) Immunohistochemical detection of CD8. (**E**) Quantification of CD8+ cells. Total CD8+ cells counts were

normalized to tissue area (mm^2) and averaged among groups. (**F**) Double immunohistochemical detection of DPP4 (brown) and αSMA (SMA, purple). (**G**) Quantification of DPP+SMA+ fibroblasts. Percentage of DPP4+SMA+ area (μm^2) normalized to tissue area (μm^2) was averaged among groups. All sections were counterstained with methyl green, and all images are representative of each sample and group. Black triangles indicate sample with combined metformin and gliptin use, while red triangles indicate metformin use alone. *significance noted only between samples with combined metformin and gliptin use compared to fibrotic samples. Analyses were performed using ImagePro Premier software. (**B, D, F)** Representative images of non-fibrotic (N=8-9), fibrotic (N=8-9), and metformin (N=9) ovaries are shown. One-way ANOVA with Tukey's posttest was used to determine significance with (**C, E**) a,b or (**G**) * indicating significance ($p<0.05$) between groups. (**B,D**) Scale bars = 50 μm. (**F**) Scale bars = 125 μm.

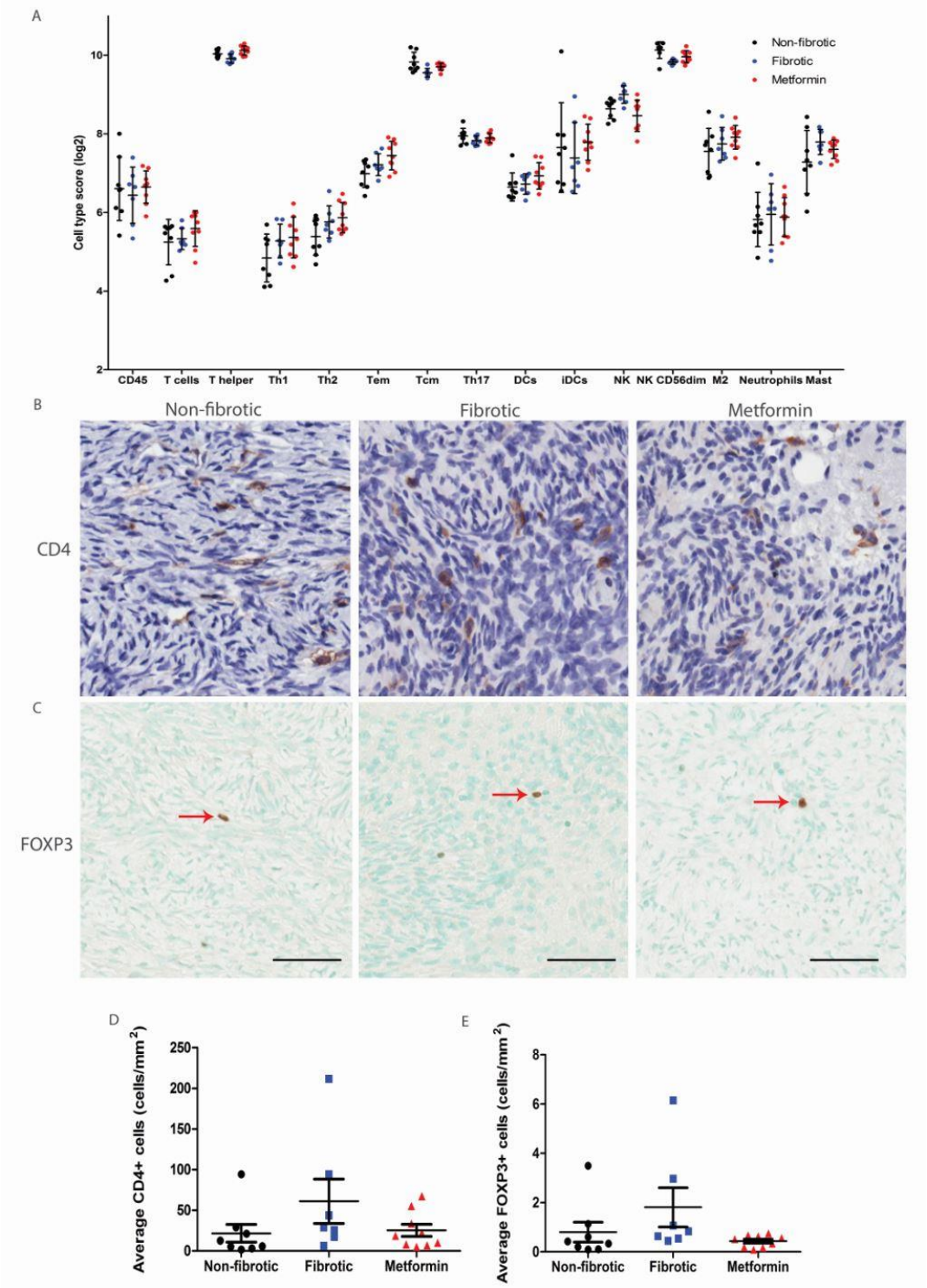

Figure 4-10. Non-significant alterations in the immune and stromal landscape of the ovarian cortex with metformin use. (**A**) Non-significant changes with immune cell type prediction. Cell type scores were derived using the cell type profiling algorithm on Nanostring nSolver software. Average log-scale expression based on a modified Pearson's correlation coefficient of cell type-specific gene sets is presented. (**B**)

Immunohistochemical detection of CD4 (brown) counterstained with hematoxylin. (**C**) Immunohistochemical detection of FOXP3 (brown) counterstained with methyl green. Quantification of (**D**) CD4+ and (**E**) FOXP3+ cells with total positive cell counts normalized to tissue area (mm^2) and averaged among groups. (**A-C)** Analysis was performed on non-fibrotic (N=8), fibrotic (N=7), and metformin (N=9) ovaries. (**B,C)** Image quantification was performed using ImagePro Premier software. One-way ANOVA with Tukey's posttest was used to determine significance with 'a,b' indicating significance ($p<0.05$) between groups. Scale bars = 50 μm.

4.5 Discussion

Organ fibrosis has become an established fertile 'soil' that is permissive to tumorigenesis and metastasis (Cox and Erler, 2014; Jacobs et al., 1999; Olaso et al., 1997). The restructuring of ECM components in fibrosis such as collagens and fibronectin provide mechanosensory cues that facilitate cancer cell invasion (Harper et al., 2018; Provenzano et al., 2008). In addition, chronic inflammation that is characteristic of fibrosis, provides cytokines that enhance fibroblast activation and establish a microenvironment that promotes metastases (Harper et al., 2018; Langley and Fidler, 2011; Weiskirchen et al., 2018). Ovarian cancers are age-associated cancers with the median age of diagnosis of 63 years old, and many of the changes found in fibrosis are characteristic of normal aging tissues, though the reasons for this have been largely understudied. A recent study by Loughran and colleagues (2018) has shown that aging promotes enhanced metastasis within the peritoneal cavity following IP injection of ID8-*Trp53*$^{-/-}$*-RFP*, including enhanced metastasis to the ovary. In addition, age-associated fibrosis was shown to occur in murine ovaries (Briley et al., 2016). Here we validated the presence of age-associated murine ovarian fibrosis with fibrosis present in 60% of mice >20 months old, and this fibrosis correlated with chronic inflammation through T cell recruitment and IDO1 expression. In contrast, 40% of mice >20 months old had no signs of ovarian fibrosis and exhibited loss of follicles and tubular adenomas similar to the *Wv/Wv* model, a phenotype previously suggested to increase cancer risk (Smith et al., 2012; Vanderhyden, 2005). This highlights the possibility of multiple forms of ovarian aging, which may have differential cancer risk based on the resultant microenvironment. Interestingly, no fibrosis was present in VCD-treated ovaries suggesting that the fibrotic phenotype is due to cumulative

ovulations instead of a direct effect of follicle loss. Our study translates these findings and provides novel evidence of age-associated ovarian fibrosis occurring in post-menopausal human ovaries using MTS and SHG imaging.

The first link between metformin use and cancer risk reduction was found in 2005 by Evans and colleagues (2005). Multiple studies have built on Evans' findings and shown a protective effect of metformin use on ovarian cancer incidence in T2D women (Bodmer et al., 2011; Tseng, 2015); however there has been conflicting evidence in the literature with studies profiling different patient cohorts (Urpilainen et al., 2018). Interestingly, in the study done by Tseng and colleagues (2015) that profiled 640,193 Taiwanese women with T2D, the overall risk in T2D women not taking metformin (never-user) was 146.4 per 100,000 person-years compared to 49.4 for those who have taken metformin (ever-user). In contrast, Urpilainen and colleagues (2018) found risk to be 39.3 and 41.1 per 100,000 person-years for never-user and ever-users respectively, among their Finnish cohort. Aside from the small sample size of the Finnish cohort with only 303/137643 patients having ovarian cancer, it is curious that the never-user risk among the Finnish cohort (39.3) is much lower than the never-user risk among the Taiwanese cohort (146.4) suggesting that the Finnish T2D populations's overall risk is lower than the risk among Taiwanese T2D women (Tseng, 2015). More global studies must be carried out to determine the efficacy of metformin use in ovarian cancer risk reduction within the T2D population. Among epidemiological studies exploring metformin and ovarian cancer risk, no mechanisms have been elucidated, with observed effects only hypothesized to be due to the metabolic function of metformin. Here we show that metformin use in post-menopausal women

(metformin ovaries) reverses or prevents fibrosis, as shown by MTS and SHG imaging. A major limitation of this study was that all samples were from formalin-fixed tissues, limiting our ability to study the dynamics of ovarian fibrosis since we cannot assess the level of ovarian fibrosis prior to metformin use in our cohort. More studies are required to determine if metformin prevents collagen anisotropy or reverses it once fibrosis is established. This may be possible through the development of novel models of ovarian fibrosis or emerging imaging modalities that could be employed clinically, such as a recently developed PET imaging probe that detects collagen-fibrosis (Désogère et al., 2017).

Limitations to this study also include a lack of information on parity and oral contraceptive use along with the small sample size of our patient cohort, such that the contribution of cumulative ovulations to age-associated human ovarian fibrosis could not be determined.

Regardless of study limitations, metformin use, fibrosis, and menopausal status were predictors of ovarian gene expression. Metformin ovaries lacking fibrosis clustered independently from fibrotic ovaries among post-menopausal ovaries suggesting metformin, possibly through the regulation of ovarian fibrosis, can alter the ovarian microenvironment. Among genes differentially expressed in metformin compared to fibrotic ovaries, *DPP4* was the most downregulated gene. DPP4 marks a lineage of pro-fibrotic fibroblasts, and we found DPP4+αSMA+ fibroblasts were upregulated in fibrotic ovaries compared to non-fibrotic ovaries and metformin ovaries that also had noted gliptin

use. These results highlight a possible synergistic effect with metformin and gliptin use in the regulation of ovarian fibrosis. Metformin ovaries also had less CD8+ T cell and pro-fibrotic eosinophil infiltration suggestive of reduced inflammation when compared to fibrotic ovaries. In addition, metformin ovaries have reduced *FN1* expression. This along with the restoration of collagen architecture suggests that metformin use has abrogated features characteristic of a PMN within the ovary (Cox and Erler, 2014).

Macrophages are key players in mediating tissue inflammation upon injury, and also in wound healing and resolution (Lech and Anders, 2013). Based on the predicted influx of M1 macrophages in metformin ovaries, we assessed macrophage populations through the ratio of M2:M1 macrophages. Non-fibrotic and metformin ovaries had a reduced CD206:CD68 ratio when compared to fibrotic ovaries suggesting metformin can affect macrophage polarization either directly, or through regulating ovarian fibrosis that in turn alters polarization. Even so, enhanced M1 polarization in metformin ovaries suggests that metformin use remedies the state of chronic inflammation seen in fibrotic ovaries due to the role of M1 in tissue immunosurveillance. In contrast, enhanced M2 polarization in fibrotic ovaries is suggestive of a chronic inflammatory state permissive to tumorigenesis (Mantovani et al., 2002). Consistent with these findings, metformin use downregulated complement pathway proteins *C2* and *C*3, which have been implicated in fibrosis, the establishment of a PMN within the cerebrospinal fluid, and in the promotion of M2 polarization, such that increased C3 promotes M2 polarization during tumor progression (Boire et al., 2017; Danobeitia et al., 2014; Fisher et al., 2017; Khan et al., 2015). In addition to enhanced M1 polarization, the cytokine milieu upregulated in metformin

ovaries (*CCL8, CCL26, IL10, VEGFA*) suggests enhanced M2c polarization among the CD206+ population, which are a subset of M2 macrophages involved in the resolving fibrosis (Lech and Anders, 2013; Ueha et al., 2012). This could indicate that metformin use may also promote the resolution phase of tissue repair. More mechanistic studies that are not limited to fixed tissues will be required to tease out the contribution of various macrophage populations to ovarian aging.

Interestingly, some pre-menopausal samples (patients #1 and 2) had evidence of fibrosis by SHG and MTS and clustered with fibrotic post-menopausal ovaries. Among these two patients, patient #2 was deemed high-risk due to family history, but did not carry a *BRCA* mutation, suggesting factors beyond age may accelerate the development of ovarian fibrosis, warranting more study into ovarian fibrosis and ovarian cancer risk.

To extend these findings into the clinic, it will be important to establish a prospective cohort of non-T2D women who use metformin, in order determine if metformin use could lower ovarian cancer risk among non-T2D women. Prior to a large study in the general population, one such cohort could be PCOS patients who have a high level of ovarian fibrosis, and increased risk of endometrial cancer (Shafiee et al., 2014; Zhou et al., 2017). Another cohort could be high-risk *BRCA* mutation carriers as there is evidence that *BRCA* mutation promotes fibroblast activation and fibrosis dating back to 1996, when Salazar and colleagues (1996) showed *BRCA* mutation carriers have more frequent stromal hyperplasia (Dauplat et al., 2009; Etzold et al., 2016). This may suggest that ovarian fibrosis is

accelerated in this high-risk population and could benefit from metformin use for cancer prophylaxis. Using novel techniques such as PET probes that detect organ fibrosis (Désogère et al., 2017), one could establish a baseline of fibrosis among patients and then measure fibrosis following a time-course of metformin use and downstream ovarian cancer incidence.

Taken together, our study provides a possible mechanism for the demonstrated ovarian cancer risk reduction with metformin use in T2D women through the abrogation of possible mechanosensory and microenvironmental cues that facilitate cancer growth and metastasis. This study positions metformin use in the context of regulating fibrosis instead of solely affecting cell metabolism to reduce cancer risk. Finally, this study offers novel insights into the age- and ovulation-associated risk of ovarian cancer, introducing modulation of ovarian fibrosis as a possible new frontier for ovarian cancer prevention.

4.6 Materials and methods

4.6.1 Experimental design

This study aimed to determine if ovarian fibrosis occurs during human aging and underlies aging and ovulation-associated ovarian cancer risk. We also aimed to determine if metformin use-associated ovarian cancer risk reduction occurs through the regulation of ovarian fibrosis. In exploring these hypotheses, we first set out to validate the findings of age-associated ovarian fibrosis in murine ovaries by Briley and colleagues (2016) using a cohort of aged mice from 3-33 months of age in a controlled lab experiment. For murine VCD studies, a small sample size (N=3) was selected to validate the histology seen

previously in studies from our laboratory (Laviolette et al., 2011). Given that this model did not replicate the fibrosis seen in natural aging, it was not used for downstream analysis due to our specific interest in studying the effects of ovarian fibrosis. To determine if this phenotype is present in aging human ovaries we assembled a cohort of ovarian samples from pre-menopausal, post-menopausal, and post-menopausal women taking metformin for T2D treatment. These human ovarian samples were used to assess collagen architecture, gene expression profiling, and IHC detection of features associated with fibrosis and chronic inflammation. Based on the rarity of healthy human ovarian samples and space and resource limitations with Nanostring arrays (12 samples/run) patient recruitment was halted once a minimum of 5 patients per group was achieved. To increase power, we included contralateral ovarian samples, both as a separate replicate and a good control to assess intra-patient heterogeneity. Patients who had more than two-samples assessed are indicated in Table 4-1. Prior to analysis, patient ovary samples were determined to be histologically normal by an experienced gynecological pathologist (M.K. Senterman), and exclusion criteria was then set based on the reasoning for ovary removal, drug usage, and histology. Patients with contralateral malignant ovarian cancer were excluded. Patients with cystic or inflammatory conditions were excluded with the exception of patient #4, a pre-menopausal patient with progesterone anaphylaxis, as we were curious if this condition affected the immune landscape of the ovary. Patients were also excluded if taking testosterone or Lupron. All quantification of human samples was performed blinded or by automated image analysis software to remove bias, which was important due to obvious structural changes in pre- vs. post-menopausal ovaries.

4.6.2 Patient samples

Ovarian samples were acquired from oophorectomies performed at The Ottawa Hospital. Samples were retrieved from archived tissues with protocol approval of the Ottawa Health Science Network Research Ethics Board. All samples were deemed normal and non-cancerous by an experienced gynecologic pathologist (M.K. Senterman). Large regions of ovarian cortex (often bilateral samples represented by numerous samples per patient in Table 4-1) were isolated, formalin-fixed, and paraffin-embedded for subsequent immunohistochemistry and microdissection.

4.6.3 Animals

Animal experiments were carried out using protocols approved by the Animal Care Committee at the University of Ottawa and conforming to or exceeding the standards defined by the Canadian Council on Animal Care. Female C57BL/lcrfa mice (P. Fotheringham and Davies, 1980) were aged up to 33 months such that there were at least 6 mice per group (0-12 months, 12-20 months, >20 months). Mice were randomly assigned to conventional micro-isolator cages with plastic huts and corn cob bedding, in groups of 5 upon weaning. For VCD treatment, following a 7 day acclimation period, C57BL/6 mice (Charles River, strain code: 027) were randomly allocated to 2 treatment groups (3 mice per group). Mice in each cage were randomly allocated to a group that received intraperitoneal injection of PBS or VCD (240 mg/kg in PBS) for 5 simultaneous days. Injections were completed cage by cage. Mice were assessed for wellness by staff of the Animal Care and Veterinary Service on a daily basis, and mice necropsies were done blinded to treatment group. Mice in this study were sacrificed 60-days post-VCD or PBS

treatment. Mice were maintained in dedicated rooms for animal breeding (aging) or hazardous chemical procedures (VCD) (21 ºC, 40-60% humidity, 12 h/12 h light dark cycle) and a commercial rodent diet (2018 Teklad Global 18% Protein Rodent Diet, Harlan Laboratories) along with acidified water that was available *ad libitum*. Housing, food and water were autoclaved prior to use, and all animal handling was performed in a certified ESCO type A2 BSC hood.

4.6.4 Immunohistochemistry

Histopathological assessment of murine and human ovaries was performed using hematoxylin and eosin (H&E) and Masson's trichrome staining (MTS), as well as immunohistochemistry. All immunohistochemistry experiments were done using 5μm sections of formalin-fixed paraffin embedded (FFPE) tissue. Following deparaffinization in xylenes and an alcohol gradient, pressurized antigen retrieval was performed in a citrate buffer (antigen unmasking solution pH 6.0, Dako). Endogenous peroxidase activity was blocked using 10min incubation in 3% H_2O_2. Following PBS washes, immunostaining for murine (m) CD8 (1:400, abcam #ab217344), CD4 (1:500, abcam #ab183685), FOXP3 (1:500, Ebioscience #14-5773-82), IDO1 (1:500, LsBio #LS-B13273) or human (h) CD8 (1:1500, abcam #ab187279), CD4 (1:500, abcam #ab133616), CD68 (1:500, Novus Biologicals #NB100-683SS), CD206 (1:1000, abcam #ab64693), FOXP3 (1:75, Ebioscience 14-4777-82), DPP4 (1:350, abcam #ab61825), or αSMA (1:600, Dako) was performed either 1 hour at room temperature (mCD8, mCD4, hCD8, hCD4, hCD206, hαSMA), or overnight at 4 ºC (mFOXP3, hFOXP3, mIDO1, hCD68, hDPP4). Species appropriate horseradish peroxidase (HRP) conjugated secondary antibodies (Vector) were then added for 1 hour at room temperature. Sections were developed in either

diaminobenzidene (DAB, Sigma, D8001) for 5 min or ImmPACT VIP peroxidase substrate (Vector, SK-4605) for 10 min, following by counterstaining with either hematoxylin (room temperature for 1 min) or methyl green (55 ^{o}C for 4 min). Sections were then clarified in an alcohol gradient and xylenes and mounted with permount (Fisher Scientific). Images were acquired using the Scanscope CS2 (Aperio).

4.6.5 Immunohistochemistry image analysis

Murine image quantification was performed using Aperio Imagescope for cell counts (mCD8, mCD4, mFOXP3) using the count tool and normalizing to ovarian area and also for automated pixel quantification of Masson's Trichrome staining using hue length: 0.64. Cell counts were performed blinded. Due to the large size of human ovary sections, quantification of hCD68, hCD206, hCD8, hDPP4, hαSMA, hFOXP3, and hCD4 was performed using ImagePro Premier 9.0 software with custom smart segmentation for each stain to quantify cell number or stain area depending on the resolution and clarity of signal. For example, CD4 and CD8 allow for the quantification of cell number, whereas diffuse stains such as DPP4 or αSMA+ fibroblasts where signals are less cell-distinctive made it challenging to quantify individual cell number and thus areas are presented. To quantify DPP4+αSMA+ fibroblasts, the total area of DPP4+ signal was multiplied by the ratio of αSMA+ signal that co-expresses DPP4+ using the Parent-child application on ImagePro Premier software. All measurements were normalized to ovarian cortex area (mm^2).

4.6.6 Second-harmonic generation imaging

Unstained paraffinized 5 μm sections of human ovaries were imaged using second harmonic generation (SHG) microscopy. Two regions of the ovarian cortex representative

of the majority of the cortical collagen architecture by Masson's trichrome staining were annotated for imaging. One outlier region representing heterogeneity of collagen architecture was also imaged to determine if SHG imaging could reveal and match similar features to Masson's trichrome staining. Images were acquired using a laser-scanning microscope (Fluoview FVMPE-RS, Olympus) to scan the sample with a Ti:saphire femto-second laser (Mai Tai HP, Spectra Physics). The pulse duration was 150 fs at an 80 MHz pulse frequency, and wavelength was set to 840 nm. The average laser power at the sample was (28 ± 1) mW. Coherency analysis of collagen fiber orientation in SHG images was performed using the OrientationJ plugin on Fiji software.

4.6.7 Ovary microdissection and RNA isolation

FFPE human ovarian samples were first serially sectioned into 10 μm sections in RNAse-free conditions. All sections were immediately stored at -80 ^{o}C to preserve RNA quality prior to microdissection. Sections were thawed at room temperature prior to automated microdissection using the AVENIO Millesect System (Roche). A serially sectioned hematoxylin-stained reference slide was used to annotate the region of the ovarian cortex to collect. Ovarian surface adhesions and regions near ovulatory follicles (pre-menopausal ovaries) were excluded from collection. All region annotations were proximal to the ovarian surface epithelium to ensure only ovarian cortex was collected with minimal medulla contamination. Tissue was collected in mineral oil from the same regions in three serially sectioned 10 μm sections per sample. RNA was then isolated using the RecoverAll Total Nucleic Acid Isolation kit (Invitrogen, AM1975) as per manufacturer's instructions and stored at -80^{o}C for downstream applications.

4.6.8 Nanostring analysis

RNA quality from microdissected human ovarian samples was assessed using Fragment Analysis (AATI Fragment Analyzer) and concentration was determined using Qubit 3.0 Fluorometer (ThermoFisher). All samples met quality control standards as suggested for use with Nanostring arrays. Nanostring PanCancer Immune Signaling capture and reporter codesets (Nanostring, #115000132) were mixed with 200-300 ng of RNA/sample following concentration of RNA into a 5 μL volume using the RNA clean and concentrator kit (Zymo, R1015). RNA and codeset solutions were incubated at 65 ^{o}C for 22 hours. Samples were then run using the nCounter MAX Analysis System (Nanostring) using high-sensitivity settings. Quality control of resultant data was performed using preset standards on nSolver software (Nanostring) with all samples passing all quality control standards.

For unsupervised hierarchical clustering and visualization, normalized expression values were log2 transformed and housekeeping genes were omitted. Expression values for each gene were then standardized (Z-score transformation) and capped at -3 and 3 to prevent artifactual clustering from a small number of spurious measurements. Samples and genes were separately clustered using Ward's method (ward.d2) from the R package pheatmap. For differential gene expression analysis, normalized expression values were averaged among groups and fold changes were derived in all pairwise comparisons using a p-value cutoff of 0.05 for significance. For cell type prediction analysis, normalized expression values were assessed using the cell type prediction algorithm in the nCounter Advanced Analysis Software package (version 2.0115) with cell type gene annotations provided in Table 4-5. Cell type scores per sample were averaged within groups. Venn diagrams were

produced using the Venny online tool (Oliveros, J.C, 2007) with a minimum fold change cutoff of ±1.25.

4.6.9 Gene ontology analysis

Normalized differential gene expression with a minimum fold change cutoff of ±1.25 was used to enhance gene ontology (GO) term calling based on the small number of differentially expressed genes in the Nanostring dataset. GO term analysis was performed using the DAVID Bioinformatics Resource (Huang et al., 2009a, 2009b) with an EASE threshold of 0.1 in all pairwise comparisons. Only terms containing >2 genes were included, and resultant p-values were -log10 transformed.

4.6.10 Statistical analysis

All experiments were performed on a sample size of ≥3 as indicated in the figure legends or text. Student's t-test was used to determine statistical significance of fold change ratios derived from differential gene expression with statistical significance $p<0.05$. One-way analysis of variance (ANOVA) was used to determine significance when one variable is presented in three or more groups. Two-way ANOVA was used to determine significance when more than one variable was assessed in three or more groups. Tukey's posttest was used in all cases with statistical significance $p<0.05$.

4.7 Acknowledgments

We would like to acknowledge and honor the late Ms. Margaret Craig, whose generous support funded the majority of this study. We would also like to acknowledge the Department of Pathology at the Ottawa Hospital for their hard work in preparing the

ovarian cortex samples. We thank Michele Geoffrion from the Ottawa Heart Institute for her help with Nanostring arrays.

4.8 Funding

This project received funded from the Canadian Institutes of Health Research (MOP136829). CWM is funded by a Vanier Canada Graduate Scholarship. DPC is funded by a CIHR Doctoral Research Award. Competing interests: The authors declare no conflicts of interest.

5 CHAPTER 5: GENERAL DISCUSSION

5.1 Summary of findings

This thesis set out to exploit the features of the TME to develop novel therapeutic, diagnostic, and prevention strategies for ovarian cancer. This led us develop a new syngeneic model of HGSC in the FVB/N strain, the STOSE model, which has features of the TME seen in HGSC (Chapter 2). STOSE cells contained a population of SCA1+ TICs that enhanced anchorage-independent growth in a colony formation assay and were able to initiate tumorigenesis faster than SCA1- cells. The STOSE model offers a rich resource for testing novel therapeutics and diagnostics for ovarian cancer, which led us to collaborate on the first application of deep learning to ovarian tissue classification (Chapter 3). Pre-trained CNNs were able to properly stratify TPEF and SHG images of normal reproductive tissues (both ovary and oviduct) and STOSE-derived tumor tissue. This study provides a proof-of-principle for the application of deep learning to ovarian cancer classification, opening up numerous avenues of research to answer more clinically pressing problems in diagnostics and treatment planning. The structural changes revealed by TPEF and SHG imaging between normal and cancerous tissues began our interest in the normal tissue microenvironment found in a PMN, given that the ovary is a common site for metastasis. This led us to provide the first evidence of age-associated human ovarian fibrosis, which correlated with appearance of features characteristic of PMNs (Chapter 4). Importantly, ovarian fibrosis and PMN features were abrogated by metformin use providing a novel mechanistic basis for the observed ovarian cancer risk reduction in T2D women using metformin, and positioning metformin use as a promising global prophylactic strategy.

5.2 STOSE model utility

Our initial characterization of the STOSE model profiled the growth rate, genomic instability, IHC markers and identified a SCA1+ TIC population (McCloskey et al., 2014). To expand on the relevance of the STOSE model, copy number analysis and whole genome sequencing would improve this model by allowing for more direct comparisons with human HGSC and the TCGA dataset. Additionally, aside from phenocopying IHC markers and having similar dynamics in gene expression (downregulation of *Cdkn2a* and overexpression of *Ccnd1)* as HGSC, STOSE cells lack a *Trp53* mutation. This limits the relevance of the STOSE model to human disease since ~94% of human HGSC have mutant *TP53* (Cole et al., 2016). The use of CRISPR-Cas9 to knockout *Trp53* or knock-in a *Trp53* mutation was recently performed in ID8 cells, generating ID8 cells with a more aggressive phenotype (Walton et al., 2016). Similarly, introducing *Trp53* alterations in STOSE cells would enhance their relevance to HGSC. Additionally, Walton and colleagues (2016) introduced a *Brca1* or *Brca2* mutation along with a *Trp53* alteration in ID8 cells. The addition of both a *Brca2* and *Trp53* mutation better phenocopied the histology of HGSC with the appearance of tertiary lymphoid structures in the resultant tumors. The addition of *Brca1/2* mutations into STOSE cells would generate a syngeneic model of hereditary HGSC that may also be representative of the spontaneous loss of BRCA expression that is characteristic of sporadic HGSC cases (Weberpals et al., 2008).

Given that STOSE cells reproducibly develop HGSC-like tumors in syngeneic FVB/N mice, the STOSE model is apt for developing novel immunotherapies. In future studies, it will be important to assess the features that we have come to appreciate as important

indicators of immunotherapeutic efficacy. Such features include MHC status and PD-L1/2 expression on STOSE cells, total mutational and neoantigen burden, ascites immune composition, hot versus cold immune landscape of the TME, and the contribution of tumor stroma (cancer-associated fibroblasts) to tumor immunosuppression (Kroeger et al., 2016; Martin et al., 2016; McGranahan et al., 2016; Nelson, 2008). We have begun to explore these features by profiling the immune landscape of intrabursal-derived STOSE tumors and have found that STOSE tumors have increased T-cell infiltration and a larger CD4+ Treg population than ID8 tumors, suggesting STOSE tumors contain a T-cell-rich or 'hot' TME. In contrast, orthotopic ID8 tumors generate a myeloid-rich or 'cold' TME. Given the susceptibility of both ID8 cells and STOSE cells to oncolytic virus infection *in vitro* (Thomas et al., 2016), and the contrasting immune landscapes within the TME, using both the STOSE and ID8 models for immunotherapeutic testing will offer robust information on the effects of a therapy on the TME.

5.3 Chemoresistance

The identification of SCA1+ TICs within the STOSE cell population was an exciting addition to this model. To further support that SCA1+ cells represent a TIC population within STOSE tumors, chemosensitivity assays should be performed both *in vitro* and *in vivo*. This could include cell death assays with carboplatin treatment in cultures of SCA1+ sorted STOSE cells *in vitro*, or quantification of the SCA1+ population in tumors following carboplatin treatment *in vivo.* One would expect that chemotherapy expands the SCA1+ population if SCA1+ cells are a classical TIC population. However, *Sca1* has no human ortholog, thereby limiting the translation of our findings to HGSC (Holmes and Stanford, 2007). It will be important to build on our characterization of SCA1+ STOSE cells by

determining the expression of established TIC markers (CD133, CD44, CD24, ALDH1A, CD117) in STOSE cells (Kulkarni-Datar et al., 2013; Parte et al., 2018). It would be interesting to determine the co-expression of these markers given the heterogeneity of the markers used in the literature. It will be important for the field to resolve marker selection for TIC populations in order to assess TIC-targeted therapeutic efficacy in the face of tumor heterogeneity.

5.4 Deep learning and diagnostics

The use of deep learning successfully stratified normal and cancerous murine tissue in our proof-of-principle study (Chapter 3). It is not entirely surprising that TPEF performed nearly as well as combined TPEF and SHG imaging when using the four pre-trained CNNs in our model. This is likely due to the simplicity of our proof-of-principle hypothesis. TPEF reveals cellular morphology, which is known to be altered in cancer where cancer cells have larger, irregularly shaped nuclei with distinctive nucleoli (Baba and Câtoi, 2007; Watson et al., 2014). These morphological changes likely gave a strong enough signal from TPEF images to successfully stratify normal vs. cancer using the CNNs.

Pathologists are extremely adept at determining normal from cancer, however, diagnosing ovarian cancer subtypes requires specialist training that may not be available in all hospitals. Additionally, determining the chemosensitivity or predicting the efficacy of an immunotherapy is currently not possible. Deep learning methodologies could have robust application to the complex questions of subtype classification, chemosensitivity, and immunotherapy. Providing a training set across all ovarian cancer subtypes and a training set of chemosensitive and chemoresistant tumors of matched subtypes, could generate an

easy to use algorithm that could be applied in centers without specialists, or to improve treatment planning. I anticipate that both TPEF and SHG would perform better than TPEF alone in stratifying ovarian cancer subtypes based on the morphological changes within the ECM between subtypes (Kurman and Shih, 2008).

We know that T-cell infiltration correlates with better prognosis in ovarian cancer (Nelson, 2008). Additionally, there are not only immunosuppressive barriers to successful immunotherapy, but also structural determinants of T-cell infiltration into the tumor stroma. Some ovarian tumors lack immune cells (cold-tumors) while other tumors have robust immune infiltration (hot-tumors) (McCloskey et al., 2018; Rodriguez et al., 2018). Based on the smaller size of T-cells (Strokotov et al., 2009), and structural determinants of immune infiltration, I anticipate that deep learning of TPEF and SHG images could be applied to predict immunotherapeutic efficacy. A training set from clinical trials using immune checkpoint blockade (anti-PD1 or anti-CTLA4) with responders and non-responders could be used to fine tune the CNNs. Since increasing patch number and adding horizontal and vertical reflection data improved CNN performance, adding a third imaging modality may improve the sensitivity and specificity. Given the success in using Raman spectroscopy in differentiating chemosensitive and chemoresistant ovarian cancer cell lines (Moradi et al., 2017), combining TPEF, SHG, and Raman imaging in a training dataset could greatly enhance the application of deep learning to more clinically-relevant questions.

A limitation to deep learning methodology is the small field of view of each SHG and TPEF image (250x250 μm^2). Given the heterogeneity of ovarian tumors, this small field of view could miss important features that a pathologist would identify such as mixed histology. Similarly, identifying small and rare precursor lesions may prove difficult with such a small field of view. Moving forward, a tiling microscopy approach that spans the entirety of a tissue sample will be required the ensure accurate sample coverage.

Furthermore, the majority of SHG/TPEF imaging setups are custom-made within each laboratory, highlighting possible issues in applying pre-trained CNNs across diagnostic centers. However, commercially available SHG imaging platforms have recently been released that could improve the reproducibility of a specific training image set.

Overall, these findings reveal a new avenue to explore for ovarian cancer diagnostics and treatment planning.

5.5 Diabetes, fibrosis, and ovarian cancer

Chapter 4 revealed that ovarian fibrosis develops in a majority of post-menopausal ovaries, which was abrogated by metformin use. Given that all post-menopausal ovaries in our study with metformin use had normal collagen architecture and were from women with T2D, while the fibrotic ovaries were from post-menopausal non-T2D women, it could be argued that diabetes prevents ovarian fibrosis, instead of metformin use. A proper control to tease apart the effects of diabetes compared to metformin use would be to assess post-menopausal T2D women who have never used metformin, to determine if ovarian fibrosis also develops in T2D women with age. However, samples meeting these criteria would be

difficult to acquire as metformin is the main therapy for T2D women. Moreover, diabetes has been shown to increase the risk of organ fibrosis, hypothesized to be due to chronic hyperglycemia-induced tissue damage (Ban and Twigg, 2008; Ehrlich et al., 2010), suggesting that age-associated ovarian fibrosis may be present in T2D women who do not use metformin.

Interestingly, combined metformin and gliptin use significantly reduced the number of DPP4+SMA+ fibroblasts suggesting that combined therapy may enhance the antifibrotic effects of metformin alone. Gliptins have been shown to reduce cardiac and liver fibrosis in murine models (Esposito et al., 2017; Hirakawa et al., 2015; Picatoste et al., 2013; Wang et al., 2018). Longitudinal studies assessing cancer incidence with combined metformin and gliptin use, compared to metformin use alone in T2D women should be carried out. I anticipate that combined therapy would further reduce ovarian cancer risk, in part through the abrogation of ovarian fibrosis.

5.6 PCOS, fibrosis, and ovarian cancer

PCOS is a metabolic condition that is diagnosed if a patient meets 2/3 of the following criteria: chronic anovulation, hyperandrogenism, or cystic ovaries (Furat Rencber et al., 2018; Shafiee et al., 2014). PCOS ovaries have marked cortical fibrosis that is largely responsible for chronic anovulation as the thick cortex makes extrusion of the oocyte difficult (Furat Rencber et al., 2018). Fibrosis characteristic of PCOS was shown to be driven by hyperandrogenism in a rat model (Zhang et al., 2013). Interestingly, women with PCOS have a 3-fold higher risk of endometrial cancer and a 2.5-fold higher risk of EOC

(Schildkraut et al., 1996; Shafiee et al., 2014). However, studies reporting PCOS and EOC risk have been controversial, with a meta-analyses showing no change in EOC risk among PCOS women (Barry et al., 2014), while another study showed that PCOS increases the risk of borderline serous ovarian cancer (Harris and Terry, 2016).

Many epidemiological PCOS studies have low power with very few patients that develop ovarian cancer (Harris and Terry, 2016). Additionally, no studies have determined if metformin use abrogates endometrial or ovarian cancer risk in women with PCOS. In a rat model of PCOS, metformin was able to reverse fibrosis around follicles and restore the ovarian follicle reserve, however the amount of fibrosis in the stroma was not analyzed (Furat Rencber et al., 2018). Human PCOS ovaries from patients with and without metformin use could be used as a validation cohort for our findings of ovarian fibrosis in post-menopausal ovaries.

5.7 Models of ovarian fibrosis – looking to the future

The changes in cell populations within the microenvironment of the ovarian cortex in fibrotic ovaries suggests that the ovary becomes a PMN with age (Chapter 4). Our results have opened up a new avenue of research that will require new models of ovarian fibrosis for mechanistic studies, and to determine if fibrosis enhances metastasis to the ovary. Our study was limited to fixed murine tissues preventing the study of metformin in a murine model. Treating aged mice with metformin prior to engrafting syngeneic metastatic ovarian cancer (ID8 or STOSE cells) would be a good proof-of-principle given the findings of

Loughran and colleagues (2018) that showed aged murine ovaries have enhanced metastasis.

Rat PCOS models such as dehydroepiandrosterone treatment that induces ovarian fibrosis may be clinically relevant based on the possible increase in cancer risk among PCOS patients (Harris and Terry, 2016). Recently, Umehara and colleagues (2018) showed that granulosa cell-specific *Nrg1* knockout mice develop ovarian fibrosis, generating a model that could be used to explore the mechanisms of fibrosis development, and the effects of metformin use. Inducible models would have great utility if one could introduce unilateral ovarian fibrosis while maintaining a contralateral non-fibrotic control ovary. Using the intravenous model developed by Coffman and colleagues (2016), it would be interesting to determine if cancer cells preferentially spread to a fibrotic ovary in comparison to a contralateral control. One such model could be intrabursal injection of bleomycin, based on the widespread use of bleomycin to induce lung and skin fibrosis (Choi et al., 2016; Ursini et al., 2016). I would also predict that bleomycin treatment would accelerate ovarian aging by destroying follicles as bleomycin is a chemotherapeutic agent that targets germ cell ovarian cancer (Necchi et al., 2017).

The hen model may also have utility for longitudinal studies with metformin use due to the spontaneously development of ovarian cancer after 2 years of age (Barua et al., 2009). Metformin has been shown to alter liver lipid metabolism in laying hens, however, no assessment of ovarian cancer incidence with metformin use has been reported in hens (Chen et al., 2011).

Lastly, emerging methods allow for the exploration of how mechanosensory signals contribute to cancer metastasis. Liu and colleagues (2017) developed a method to decellularize human ovaries that then could be used as scaffolds to determine if ovarian fibrosis facilitates enhanced tumor cell invasion. Decellularizing pre- and post-menopausal human ovaries with and without metformin (and/or gliptin) use would greatly contribute to our understanding of the mechanosensory signals provided by ovarian fibrosis to invading tumor cells.

5.8 Conclusion

Taken together, the results presented in this thesis highlight the importance of the tumor and tissue microenvironment in developing models, diagnostics, and prevention methods for ovarian cancer. The STOSE model offers a rich resource for testing novel therapeutics and as shown in Chapter 3, STOSE tumors have utility in optimizing novel diagnostic techniques that harness the power of artificial intelligence. Leveraging our knowledge of the tumor microenvironment led to the discovery of age-associated ovarian fibrosis in post-menopausal women, opening up a new frontier for ovarian cancer prevention and providing support for the use of metformin as a global ovarian cancer risk reduction strategy.

6 References

Amsterdam, A., 2011. Epiregulin as a marker for the initial steps of ovarian cancer development. International Journal of Oncology. https://doi.org/10.3892/ijo.2011.1123

Arts-de Jong, M., Maas, A.H.E.M., Massuger, L.F., Hoogerbrugge, N., de Hullu, J.A., 2014. BRCA1/2 mutation carriers are potentially at higher cardiovascular risk. Critical Reviews in Oncology/Hematology 91, 159–171. https://doi.org/10.1016/j.critrevonc.2014.01.008

Auersperg, N., 2013a. Ovarian surface epithelium as a source of ovarian cancers: Unwarranted speculation or evidence-based hypothesis? Gynecologic Oncology 130, 246–251. https://doi.org/10.1016/j.ygyno.2013.03.021

Auersperg, N., 2013b. The Stem-Cell Profile of Ovarian Surface Epithelium is Reproduced in the Oviductal Fimbriae, with Increased Stem-Cell Marker Density in Distal Parts of the Fimbriae: International Journal of Gynecological Pathology 32, 444–453. https://doi.org/10.1097/PGP.0b013e3182800ad5

Auersperg, N., 2013c. The origin of ovarian cancers--hypotheses and controversies. Front Biosci (Schol Ed) 5, 709–719.

Australian Cancer Study, Australian Ovarian Cancer Study Group, Pharoah, P.D.P., Tsai, Y.-Y., Ramus, S.J., Phelan, C.M., Goode, E.L., Lawrenson, K., Buckley, M., Fridley, B.L., Tyrer, J.P., Shen, Howard, Weber, R., Karevan, R., Larson, M.C., Song, H., Tessier, D.C., Bacot, F., Vincent, D., Cunningham, J.M., Dennis, J., Dicks, E., Aben, K.K., Anton-Culver, H., Antonenkova, N., Armasu, S.M., Baglietto, L., Bandera, E.V., Beckmann, M.W., Birrer, M.J., Bloom, G., Bogdanova, N., Brenton, J.D., Brinton, L.A., Brooks-Wilson, A., Brown, R., Butzow, R., Campbell, I., Carney, M.E., Carvalho, R.S., Chang-Claude, J., Chen, Y.A., Chen, Z., Chow, W.-H., Cicek, M.S., Coetzee, G., Cook, L.S., Cramer, D.W., Cybulski, C., Dansonka-Mieszkowska, A., Despierre, E., Doherty, J.A., Dörk, T., du Bois, A., Dürst, M., Eccles, D., Edwards, R., Ekici, A.B., Fasching, P.A., Fenstermacher, D., Flanagan, J., Gao, Y.-T., Garcia-Closas, M., Gentry-Maharaj, A., Giles, G., Gjyshi, A., Gore, M., Gronwald, J., Guo, Q., Halle, M.K., Harter, P., Hein, A., Heitz, F., Hillemanns, P., Hoatlin, M., Høgdall, E., Høgdall, C.K., Hosono, S., Jakubowska, A., Jensen, A., Kalli, K.R., Karlan, B.Y., Kelemen, L.E., Kiemeney, L.A., Kjaer, S.K., Konecny, G.E., Krakstad, C., Kupryjanczyk, J., Lambrechts, D., Lambrechts, S., Le, N.D., Lee, N., Lee, J., Leminen, A., Lim, B.K., Lissowska, J., Lubiński, J., Lundvall, L., Lurie, G., Massuger, L.F.A.G., Matsuo, K., McGuire, V., McLaughlin, J.R., Menon, U., Modugno, F., Moysich, K.B., Nakanishi, T., Narod, S.A., Ness, R.B., Nevanlinna, H., Nickels, S., Noushmehr, H., Odunsi, K., Olson, S., Orlow, I., Paul, J., Pejovic, T., Pelttari, L.M., Permuth-Wey, J., Pike, M.C., Poole, E.M., Qu, X., Risch, H.A., Rodriguez-Rodriguez, L., Rossing, M.A., Rudolph, A., Runnebaum, I., Rzepecka, I.K., Salvesen, H.B., Schwaab, I., Severi, G., Shen, Hui, Shridhar, V., Shu, X.-O., Sieh, W., Southey, M.C., Spellman, P., Tajima, K., Teo, S.-H., Terry, K.L., Thompson, P.J., Timorek, A., Tworoger, S.S., van Altena, A.M., van den Berg, D., Vergote, I., Vierkant, R.A., Vitonis, A.F., Wang-Gohrke, S., Wentzensen, N., Whittemore, A.S., Wik, E., Winterhoff, B., Woo, Y.L., Wu, A.H., Yang, H.P.,

Zheng, W., Ziogas, A., Zulkifli, F., Goodman, M.T., Hall, P., Easton, D.F., Pearce, C.L., Berchuck, A., Chenevix-Trench, G., Iversen, E., Monteiro, A.N.A., Gayther, S.A., Schildkraut, J.M., Sellers, T.A., 2013. GWAS meta-analysis and replication identifies three new susceptibility loci for ovarian cancer. Nature Genetics 45, 362–370. https://doi.org/10.1038/ng.2564

Baba, A.I., Câtoi, C., 2007. TUMOR CELL MORPHOLOGY. The Publishing House of the Romanian Academy.

Ban, C.R., Twigg, S.M., 2008. Fibrosis in diabetes complications: Pathogenic mechanisms and circulating and urinary markers. Vasc Health Risk Manag 4, 575–596.

Bapat, S.A., Mali, A.M., Koppikar, C.B., Kurrey, N.K., 2005. Stem and progenitor-like cells contribute to the aggressive behavior of human epithelial ovarian cancer. Cancer Res. 65, 3025–3029. https://doi.org/10.1158/0008-5472.CAN-04-3931

Bar, Y., Diamant, I., Wolf, L., Greenspan, H., 2015. Deep learning with non-medical training used for chest pathology identification. https://doi.org/10.1117/12.2083124

Barry, J.A., Azizia, M.M., Hardiman, P.J., 2014. Risk of endometrial, ovarian and breast cancer in women with polycystic ovary syndrome: a systematic review and meta-analysis. Hum Reprod Update 20, 748–758. https://doi.org/10.1093/humupd/dmu012

Barua, A., Bitterman, P., Abramowicz, J.S., Dirks, A.L., Bahr, J.M., Hales, D.B., Bradaric, M.J., Edassery, S.L., Rotmensch, J., Luborsky, J.L., 2009. Histopathology of ovarian tumors in laying hens, a preclinical model of human ovarian cancer. Int J Gynecol Cancer 19, 531–539. https://doi.org/10.1111/IGC.0b013e3181a41613

Bastin, D., Aitken, A.S., Pelin, A., Pikor, L.A., Crupi, M.J.F., Huh, M.S., Bourgeois-Daigneault, M.-C., Bell, J.C., Ilkow, C.S., 2018. Enhanced susceptibility of cancer cells to oncolytic rhabdo-virotherapy by expression of Nodamura virus protein B2 as a suppressor of RNA interference. J Immunother Cancer 6, 62. https://doi.org/10.1186/s40425-018-0366-2

Bell, D., Berchuck, A., Birrer, M., Chien, J., Cramer, D.W., Dao, F., Dhir, R., DiSaia, P., Gabra, H., Glenn, P., Godwin, A.K., Gross, J., Hartmann, L., Huang, M., Huntsman, D.G., Iacocca, M., Imielinski, M., Kalloger, S., Karlan, B.Y., Levine, D.A., Mills, G.B., Morrison, C., Mutch, D., Olvera, N., Orsulic, S., Park, K., Petrelli, N., Rabeno, B., Rader, J.S., Sikic, B.I., Smith-McCune, K., Sood, A.K., Bowtell, D., Penny, R., Testa, J.R., Chang, K., Dinh, H.H., Drummond, J.A., Fowler, G., Gunaratne, P., Hawes, A.C., Kovar, C.L., Lewis, L.R., Morgan, M.B., Newsham, I.F., Santibanez, J., Reid, J.G., Trevino, L.R., Wu, Y.-Q., Wang, M., Muzny, D.M., Wheeler, D.A., Gibbs, R.A., Getz, G., Lawrence, M.S., Cibulskis, K., Sivachenko, A.Y., Sougnez, C., Voet, D., Wilkinson, J., Bloom, T., Ardlie, K., Fennell, T., Baldwin, J., Gabriel, S., Lander, E.S., Ding, L., Fulton, R.S., Koboldt, D.C., McLellan, M.D., Wylie, T., Walker, J., O'Laughlin, M., Dooling, D.J., Fulton, L., Abbott, R., Dees, N.D., Zhang, Q., Kandoth, C., Wendl, M., Schierding, W., Shen, D., Harris, C.C., Schmidt, H., Kalicki, J., Delehaunty, K.D., Fronick, C.C., Demeter, R., Cook, L., Wallis, J.W., Lin, L., Magrini, V.J., Hodges, J.S., Eldred, J.M., Smith, S.M., Pohl, C.S., Vandin, F., Raphael, B.J.,

Weinstock, G.M., Mardis, E.R., Wilson, R.K., Meyerson, M., Winckler, W., Getz, G., Verhaak, R.G.W., Carter, S.L., Mermel, C.H., Saksena, G., Nguyen, H., Onofrio, R.C., Lawrence, M.S., Hubbard, D., Gupta, S., Crenshaw, A., Ramos, A.H., Ardlie, K., Chin, L., Protopopov, A., Zhang, Juinhua, Kim, T.M., Perna, I., Xiao, Y., Zhang, H., Ren, G., Sathiamoorthy, N., Park, R.W., Lee, E., Park, P.J., Kucherlapati, R., Absher, D.M., Waite, L., Sherlock, G., Brooks, J.D., Li, J.Z., Xu, J., Myers, R.M., Laird, P.W., Cope, L., Herman, J.G., Shen, H., Weisenberger, D.J., Noushmehr, H., Pan, F., Triche Jr, T., Berman, B.P., Van Den Berg, D.J., Buckley, J., Baylin, S.B., Spellman, P.T., Purdom, E., Neuvial, P., Bengtsson, H., Jakkula, L.R., Durinck, S., Han, J., Dorton, S., Marr, H., Choi, Y.G., Wang, V., Wang, N.J., Ngai, J., Conboy, J.G., Parvin, B., Feiler, H.S., Speed, T.P., Gray, J.W., Levine, D.A., Socci, N.D., Liang, Y., Taylor, B.S., Schultz, N., Borsu, L., Lash, A.E., Brennan, C., Viale, A., Sander, C., Ladanyi, M., Hoadley, K.A., Meng, S., Du, Y., Shi, Y., Li, L., Turman, Y.J., Zang, D., Helms, E.B., Balu, S., Zhou, X., Wu, J., Topal, M.D., Hayes, D.N., Perou, C.M., Getz, G., Voet, D., Saksena, G., Zhang, Junihua, Zhang, H., Wu, C.J., Shukla, S., Cibulskis, K., Lawrence, M.S., Sivachenko, A., Jing, R., Park, R.W., Liu, Y., Park, P.J., Noble, M., Chin, L., Carter, H., Kim, D., Karchin, R., Spellman, P.T., Purdom, E., Neuvial, P., Bengtsson, H., Durinck, S., Han, J., Korkola, J.E., Heiser, L.M., Cho, R.J., Hu, Z., Parvin, B., Speed, T.P., Gray, J.W., Schultz, N., Cerami, E., Taylor, B.S., Olshen, A., Reva, B., Antipin, Y., Shen, R., Mankoo, P., Sheridan, R., Ciriello, G., Chang, W.K., Bernanke, J.A., Borsu, L., Levine, D.A., Ladanyi, M., Sander, C., Haussler, D., Benz, C.C., Stuart, J.M., Benz, S.C., Sanborn, J.Z., Vaske, C.J., Zhu, J., Szeto, C., Scott, G.K., Yau, C., Hoadley, K.A., Du, Y., Balu, S., Hayes, D.N., Perou, C.M., Wilkerson, M.D., Zhang, N., Akbani, R., Baggerly, K.A., Yung, W.K., Mills, G.B., Weinstein, J.N., Penny, R., Shelton, T., Grimm, D., Hatfield, M., Morris, S., Yena, P., Rhodes, P., Sherman, M., Paulauskis, J., Millis, S., Kahn, A., Greene, J.M., Sfeir, R., Jensen, M.A., Chen, J., Whitmore, J., Alonso, S., Jordan, J., Chu, A., Zhang, Jinghui, Barker, A., Compton, C., Eley, G., Ferguson, M., Fielding, P., Gerhard, D.S., Myles, R., Schaefer, C., Mills Shaw, K.R., Vaught, J., Vockley, J.B., Good, P.J., Guyer, M.S., Ozenberger, B., Peterson, J., Thomson, E., 2011. Integrated genomic analyses of ovarian carcinoma. Nature 474, 609–615. https://doi.org/10.1038/nature10166

Bertoldo, M.J., Faure, M., Dupont, J., Froment, P., 2014. Impact of metformin on reproductive tissues: an overview from gametogenesis to gestation. Ann Transl Med 2. https://doi.org/10.3978/j.issn.2305-5839.2014.06.04

Best, C.L., Pudney, J., Welch, W.R., Burger, N., Hill, J.A., 1996. Localization and characterization of white blood cell populations within the human ovary throughout the menstrual cycle and menopause. Hum. Reprod. 11, 790–797.

Bigorie, V., Morice, P., Duvillard, P., Antoine, M., Cortez, A., Flejou, J.F., Uzan, S., Darai, E., Barranger, E., 2010. Ovarian metastases from breast cancer: report of 29 cases. Cancer 116, 799–804. https://doi.org/10.1002/cncr.24807

Birch, A.H., Arcand, S.L., Oros, K.K., Rahimi, K., Watters, A.K., Provencher, D., Greenwood, C.M., Mes-Masson, A.-M., Tonin, P.N., 2011. Chromosome 3 Anomalies Investigated by Genome Wide SNP Analysis of Benign, Low

Malignant Potential and Low Grade Ovarian Serous Tumours. PLoS ONE 6, e28250. https://doi.org/10.1371/journal.pone.0028250
Bodmer, M., Becker, C., Meier, C., Jick, S.S., Meier, C.R., 2011. Use of metformin and the risk of ovarian cancer: a case-control analysis. Gynecol. Oncol. 123, 200–204. https://doi.org/10.1016/j.ygyno.2011.06.038
Boire, A., Zou, Y., Shieh, J., Macalinao, D.G., Pentsova, E., Massagué, J., 2017. Complement Component 3 Adapts the Cerebrospinal Fluid for Leptomeningeal Metastasis. Cell 168, 1101-1113.e13. https://doi.org/10.1016/j.cell.2017.02.025
Bonnans, C., Chou, J., Werb, Z., 2014. Remodelling the extracellular matrix in development and disease. Nat. Rev. Mol. Cell Biol. 15, 786–801. https://doi.org/10.1038/nrm3904
Bradaric, M.J., Penumatsa, K., Barua, A., Edassery, S.L., Yu, Y., Abramowicz, J.S., Bahr, J.M., Luborsky, J.L., 2013. Immune Cells in the Normal Ovary and Spontaneous Ovarian Tumors in the Laying Hen (Gallus domesticus) Model of Human Ovarian Cancer. PLoS ONE 8, e74147. https://doi.org/10.1371/journal.pone.0074147
Braga, T.T., Agudelo, J.S.H., Camara, N.O.S., 2015. Macrophages During the Fibrotic Process: M2 as Friend and Foe. Front Immunol 6. https://doi.org/10.3389/fimmu.2015.00602
Brierley JD., Gospodarowicz MK., Wittekind C., 2017. TNM Classification of Malignant Tumours, 8th Edition [WWW Document]. Wiley.com. URL https://www.wiley.com/en-us/TNM+Classification+of+Malignant+Tumours%2C+8th+Edition-p-9781119263579 (accessed 8.20.18).
Briley, S.M., Jasti, S., McCracken, J.M., Hornick, J.E., Fegley, B., Pritchard, M.T., Duncan, F.E., 2016. Reproductive age-associated fibrosis in the stroma of the mammalian ovary. Reproduction 152, 245–260. https://doi.org/10.1530/REP-16-0129
Brynhildsen, J., 2014. Combined hormonal contraceptives: prescribing patterns, compliance, and benefits versus risks. Ther Adv Drug Saf 5, 201–213. https://doi.org/10.1177/2042098614548857
Campagnola, P., 2011. Second harmonic generation imaging microscopy: applications to diseases diagnostics. Anal. Chem. 83, 3224–3231. https://doi.org/10.1021/ac1032325
Chao, S., 1987. The effect of lactation on ovulation and fertility. Clin Perinatol 14, 39–50.
Chapelle, O., Haffner, P., Vapnik, V.N., 1999. Support vector machines for histogram-based image classification. IEEE Trans Neural Netw 10, 1055–1064. https://doi.org/10.1109/72.788646
Chen, L.-M., Wang, W., Lee, J.-C., Chiu, F.-H., Wu, C.-T., Tai, Cheng-Jeng, Wang, C.-K., Tai, Chen-Jei, Huang, M.-T., Chang, Y.-J., 2013. Thrombomodulin mediates the progression of epithelial ovarian cancer cells. Tumor Biology 34, 3743–3751. https://doi.org/10.1007/s13277-013-0958-x
Chen, W.-L., Wei, H.-W., Chiu, W.-Z., Kang, C.-H., Lin, T.-H., Hung, C.-C., Chen, M.-C., Shieh, M.-S., Lee, C.-C., Lee, H.-M., 2011. Metformin regulates hepatic lipid metabolism through activating AMP-activated protein kinase and inducing ATGL

in laying hens. Eur. J. Pharmacol. 671, 107–112. https://doi.org/10.1016/j.ejphar.2011.09.029
Chen, X., Zhang, J., Zhang, Z., Li, H., Cheng, W., Liu, J., 2013. Cancer stem cells, epithelial-mesenchymal transition, and drug resistance in high-grade ovarian serous carcinoma. Human Pathology 44, 2373–2384. https://doi.org/10.1016/j.humpath.2013.05.001
Chiang, C.L.-L., Kandalaft, L.E., Tanyi, J., Hagemann, A.R., Motz, G.T., Svoronos, N., Montone, K., Mantia-Smaldone, G.M., Smith, L., Nisenbaum, H.L., Levine, B.L., Kalos, M., Czerniecki, B.J., Torigian, D.A., Powell, D.J., Mick, R., Coukos, G., 2013. A Dendritic Cell Vaccine Pulsed with Autologous Hypochlorous Acid-Oxidized Ovarian Cancer Lysate Primes Effective Broad Antitumor Immunity: From Bench to Bedside. Clinical Cancer Research 19, 4801–4815. https://doi.org/10.1158/1078-0432.CCR-13-1185
Choi, S.M., Jang, A.-H., Kim, H., Lee, K.H., Kim, Y.W., 2016. Metformin Reduces Bleomycin-induced Pulmonary Fibrosis in Mice. J Korean Med Sci 31, 1419–1425. https://doi.org/10.3346/jkms.2016.31.9.1419
Cibula, D., Zikan, M., Dusek, L., Majek, O., 2011. Oral contraceptives and risk of ovarian and breast cancers in BRCA mutation carriers: a meta-analysis. Expert Rev Anticancer Ther 11, 1197–1207. https://doi.org/10.1586/era.11.38
Coburn, S., Bray, F., Sherman, M., Trabert, B., 2017. International patterns and trends in ovarian cancer incidence, overall and by histologic subtype. Int J Cancer 140, 2451–2460. https://doi.org/10.1002/ijc.30676
Coffman, L.G., Burgos-Ojeda, D., Wu, R., Cho, K., Bai, S., Buckanovich, R.J., 2016. New models of hematogenous ovarian cancer metastasis demonstrate preferential spread to the ovary and a requirement for the ovary for abdominal dissemination. Transl Res 175, 92-102.e2. https://doi.org/10.1016/j.trsl.2016.03.016
Cole, A.J., Dwight, T., Gill, A.J., Dickson, K.-A., Zhu, Y., Clarkson, A., Gard, G.B., Maidens, J., Valmadre, S., Clifton-Bligh, R., Marsh, D.J., 2016. Assessing mutant p53 in primary high-grade serous ovarian cancer using immunohistochemistry and massively parallel sequencing. Scientific Reports 6, 26191. https://doi.org/10.1038/srep26191
Connolly, D.C., Bao, R., Nikitin, A.Y., Stephens, K.C., Poole, T.W., Hua, X., Harris, S.S., Vanderhyden, B.C., Hamilton, T.C., 2003. Female mice chimeric for expression of the simian virus 40 TAg under control of the MISIIR promoter develop epithelial ovarian cancer. Cancer Res. 63, 1389–1397.
Cools, M., Wolffenbuttel, K.P., Drop, S.L.S., Oosterhuis, J.W., Looijenga, L.H.J., 2011. Gonadal development and tumor formation at the crossroads of male and female sex determination. Sex Dev 5, 167–180. https://doi.org/10.1159/000329477
Cooper, D.B., Adigun, R., 2018. Oral Contraceptive Pills, in: StatPearls. StatPearls Publishing, Treasure Island (FL).
Cornelison, R., Llaneza, D.C., Landen, C.N., 2017. Emerging Therapeutics to Overcome Chemoresistance in Epithelial Ovarian Cancer: A Mini-Review. Int J Mol Sci 18. https://doi.org/10.3390/ijms18102171
Corner, S., Parys, M., W Agnew, D., Moresco, A., Yuzbasiyan-Gurkan, V., 2015. Ovarian Adenocarcinoma in Captive North American Jaguars (Panthera Onca): Tumor Characterization and Investigation Of Brca1 Mutations.

Cox, T.R., Bird, D., Baker, A.-M., Barker, H.E., Ho, M.W.-Y., Lang, G., Erler, J.T., 2013. LOX-mediated collagen crosslinking is responsible for fibrosis-enhanced metastasis. Cancer Res 73, 1721–1732. https://doi.org/10.1158/0008-5472.CAN-12-2233

Cox, T.R., Erler, J.T., 2014. Molecular pathways: connecting fibrosis and solid tumor metastasis. Clin. Cancer Res. 20, 3637–3643. https://doi.org/10.1158/1078-0432.CCR-13-1059

Cox, T.R., Erler, J.T., 2011. Remodeling and homeostasis of the extracellular matrix: implications for fibrotic diseases and cancer. Dis Model Mech 4, 165–178. https://doi.org/10.1242/dmm.004077

Crow, J., Amso, N.N., Lewin, J., Shaw, R.W., 1994. Morphology and ultrastructure of fallopian tube epithelium at different stages of the menstrual cycle and menopause. Hum. Reprod. 9, 2224–2233.

Cufí, S., Vazquez-Martin, A., Oliveras-Ferraros, C., Martin-Castillo, B., Joven, J., Menendez, J.A., 2010. Metformin against TGFβ-induced epithelial-to-mesenchymal transition (EMT): from cancer stem cells to aging-associated fibrosis. Cell Cycle 9, 4461–4468. https://doi.org/10.4161/cc.9.22.14048

Curley, D.P., Bosenberg, M.W., 2008. A new mechanism of release from senescence: suppression of p16INK4a by beta-catenin. Pigment Cell Melanoma Res 21, 5–6. https://doi.org/10.1111/j.1755-148X.2007.00434.x

Dai, W., Teodoridis, J.M., Zeller, C., Graham, J., Hersey, J., Flanagan, J.M., Stronach, E., Millan, D.W., Siddiqui, N., Paul, J., Brown, R., 2011. Systematic CpG Islands Methylation Profiling of Genes in the Wnt Pathway in Epithelial Ovarian Cancer Identifies Biomarkers of Progression-Free Survival. Clinical Cancer Research 17, 4052–4062. https://doi.org/10.1158/1078-0432.CCR-10-3021

Danobeitia, J.S., Djamali, A., Fernandez, L.A., 2014. The role of complement in the pathogenesis of renal ischemia-reperfusion injury and fibrosis. Fibrogenesis Tissue Repair 7, 16. https://doi.org/10.1186/1755-1536-7-16

Dauplat, J., Chene, G., Pomel, C., Dauplat, M.M., Le Bouëdec, G., Mishellany, F., Lagarde, N., Bignon, Y.J., Jaffeux, P., Aublet-Cuvelier, B., Dechelotte, P., Pouly, J.L., Penault-Llorca, F., 2009. Comparison of dysplasia profiles in stimulated ovaries and in those with a genetic risk for ovarian cancer. Eur. J. Cancer 45, 2977–2983. https://doi.org/10.1016/j.ejca.2009.06.012

Débarre, D., Supatto, W., Pena, A.-M., Fabre, A., Tordjmann, T., Combettes, L., Schanne-Klein, M.-C., Beaurepaire, E., 2006. Imaging lipid bodies in cells and tissues using third-harmonic generation microscopy. Nat. Methods 3, 47–53. https://doi.org/10.1038/nmeth813

DeClerck, Y.A., 2012. Desmoplasia: A Response or a Niche? Cancer Discov 2, 772–774. https://doi.org/10.1158/2159-8290.CD-12-0348

Demuth, H.-U., McIntosh, C.H.S., Pederson, R.A., 2005. Type 2 diabetes--therapy with dipeptidyl peptidase IV inhibitors. Biochim. Biophys. Acta 1751, 33–44. https://doi.org/10.1016/j.bbapap.2005.05.010

Deng, B., Zhang, S., Miao, Y., Han, Z., Zhang, X., Wen, F., Zhang, Y., 2012. Adrenomedullin expression in epithelial ovarian cancers and promotes HO8910 cell migration associated with upregulating integrin α5β1 and phosphorylating

FAK and paxillin. Journal of Experimental & Clinical Cancer Research 31, 19. https://doi.org/10.1186/1756-9966-31-19
Deng, J., Dong, W., Socher, R., Li, L.-J., Kai Li, Li Fei-Fei, 2009. ImageNet: A large-scale hierarchical image database, in: 2009 IEEE Conference on Computer Vision and Pattern Recognition. Presented at the 2009 IEEE Computer Society Conference on Computer Vision and Pattern Recognition Workshops (CVPR Workshops), IEEE, Miami, FL, pp. 248–255. https://doi.org/10.1109/CVPR.2009.5206848
Denk, W., Strickler, J.H., Webb, W.W., 1990. Two-photon laser scanning fluorescence microscopy. Science 248, 73–76.
Désogère, P., Tapias, L.F., Hariri, L.P., Rotile, N.J., Rietz, T.A., Probst, C.K., Blasi, F., Day, H., Mino-Kenudson, M., Weinreb, P., Violette, S.M., Fuchs, B.C., Tager, A.M., Lanuti, M., Caravan, P., 2017. Type I collagen-targeted PET probe for pulmonary fibrosis detection and staging in preclinical models. Sci Transl Med 9. https://doi.org/10.1126/scitranslmed.aaf4696
Domcke, S., Sinha, R., Levine, D.A., Sander, C., Schultz, N., 2013. Evaluating cell lines as tumour models by comparison of genomic profiles. Nature Communications 4. https://doi.org/10.1038/ncomms3126
Donahue, J., Jia, Y., Vinyals, O., Hoffman, J., Zhang, N., Tzeng, E., Darrell, T., 2013. DeCAF: A Deep Convolutional Activation Feature for Generic Visual Recognition. arXiv:1310.1531 [cs].
Ehrlich, S.F., Quesenberry, C.P., Van Den Eeden, S.K., Shan, J., Ferrara, A., 2010. Patients Diagnosed With Diabetes Are at Increased Risk for Asthma, Chronic Obstructive Pulmonary Disease, Pulmonary Fibrosis, and Pneumonia but Not Lung Cancer. Diabetes Care 33, 55–60. https://doi.org/10.2337/dc09-0880
Endsley, M.P., Moyle-Heyrman, G., Karthikeyan, S., Lantvit, D.D., Davis, D.A., Wei, J.-J., Burdette, J.E., 2015. Spontaneous Transformation of Murine Oviductal Epithelial Cells: A Model System to Investigate the Onset of Fallopian-Derived Tumors. Front. Oncol. 5. https://doi.org/10.3389/fonc.2015.00154
Esposito, G., Cappetta, D., Russo, R., Rivellino, A., Ciuffreda, L.P., Roviezzo, F., Piegari, E., Berrino, L., Rossi, F., Angelis, A.D., Urbanek, K., 2017. Sitagliptin reduces inflammation, fibrosis and preserves diastolic function in a rat model of heart failure with preserved ejection fraction. British Journal of Pharmacology 174, 4070–4086. https://doi.org/10.1111/bph.13686
Etzold, A., Galetzka, D., Weis, E., Bartsch, O., Haaf, T., Spix, C., Itzel, T., Schweiger, S., Strand, D., Strand, S., Zechner, U., 2016. CAF-like state in primary skin fibroblasts with constitutional BRCA1 epimutation sheds new light on tumor suppressor deficiency-related changes in healthy tissue. Epigenetics 11, 120–131. https://doi.org/10.1080/15592294.2016.1140295
Evans, J.M.M., Donnelly, L.A., Emslie-Smith, A.M., Alessi, D.R., Morris, A.D., 2005. Metformin and reduced risk of cancer in diabetic patients. BMJ 330, 1304–1305. https://doi.org/10.1136/bmj.38415.708634.F7
Fathalla, M.F., 2013. Incessant ovulation and ovarian cancer – a hypothesis re-visited. Facts Views Vis Obgyn 5, 292–297.

Fisher, A.J., Cipolla, E., Varre, A., Gu, H., Mickler, E.A., Vittal, R., 2017. Potential Mechanisms Underlying TGF-β-mediated Complement Activation in Lung Fibrosis. Cell Mol Med Open Access 3.

Fleming, J.S., Beaugié, C.R., Haviv, I., Chenevix-Trench, G., Tan, O.L., 2006. Incessant ovulation, inflammation and epithelial ovarian carcinogenesis: revisiting old hypotheses. Mol. Cell. Endocrinol. 247, 4–21. https://doi.org/10.1016/j.mce.2005.09.014

Flesken-Nikitin, A., Choi, K.-C., Eng, J.P., Shmidt, E.N., Nikitin, A.Y., 2003. Induction of Carcinogenesis by Concurrent Inactivation of p53 and Rb1 in the Mouse Ovarian Surface Epithelium. Cancer Res 63, 3459–3463.

Flesken-Nikitin, A., Hwang, C.-I., Cheng, C.-Y., Michurina, T.V., Enikolopov, G., Nikitin, A.Y., 2013. Ovarian surface epithelium at the junction area contains cancer-prone stem cell niche. Nature 495, 241–245. https://doi.org/10.1038/nature11979

Fleury, H., Communal, L., Carmona, E., Portelance, L., Arcand, S.L., Rahimi, K., Tonin, P.N., Provencher, D., Mes-Masson, A.-M., 2015. Novel high-grade serous epithelial ovarian cancer cell lines that reflect the molecular diversity of both the sporadic and hereditary disease. Genes Cancer 6, 378–398.

Focchi, G.R., Simões, M. de J., Baracat, E.C., de Lima, G.R., Evêncio Neto, J., 1996. Ultrastructural aspects of the remodeling process of the Corpus albicans in the recent postmenopausal period. Sao Paulo Med J 114, 1173–1176.

Foster, R., Buckanovich, R.J., Rueda, B.R., 2013. Ovarian cancer stem cells: Working towards the root of stemness. Cancer Letters 338, 147–157. https://doi.org/10.1016/j.canlet.2012.10.023

Foulkes, W., 2004. BRCA1 functions as a breast stem cell regulator. J Med Genet 41, 1–5. https://doi.org/10.1136/jmg.2003.013805

Furat Rencber, S., Kurnaz Ozbek, S., Eraldemır, C., Sezer, Z., Kum, T., Ceylan, S., Guzel, E., 2018. Effect of resveratrol and metformin on ovarian reserve and ultrastructure in PCOS: an experimental study. J Ovarian Res 11. https://doi.org/10.1186/s13048-018-0427-7

Gaitskell, K., Green, J., Pirie, K., Barnes, I., Hermon, C., Reeves, G.K., Beral, V., 2018. Histological subtypes of ovarian cancer associated with parity and breastfeeding in the prospective Million Women Study. Int J Cancer 142, 281–289. https://doi.org/10.1002/ijc.31063

Gaitskell, K., Green, J., Pirie, K., Reeves, G., Beral, V., Million Women Study Collaborators, 2016. Tubal ligation and ovarian cancer risk in a large cohort: Substantial variation by histological type. Int. J. Cancer 138, 1076–1084. https://doi.org/10.1002/ijc.29856

Galic, V., Coleman, R.L., Herzog, T.J., 2013. Unmet needs in ovarian cancer: dividing histologic subtypes to exploit novel targets and pathways. Curr Cancer Drug Targets 13, 698–707.

Gamwell, L.F., Collins, O., Vanderhyden, B.C., 2012. The Mouse Ovarian Surface Epithelium Contains a Population of LY6A (SCA-1) Expressing Progenitor Cells That Are Regulated by Ovulation-Associated Factors1. Biology of Reproduction 87. https://doi.org/10.1095/biolreprod.112.100347

Garson, K., Gamwell, L.F., Pitre, E.M., Vanderhyden, B.C., 2012. Technical challenges and limitations of current mouse models of ovarian cancer. Journal of Ovarian Research 5, 39. https://doi.org/10.1186/1757-2215-5-39

George, S.H.L., Garcia, R., Slomovitz, B.M., 2016. Ovarian Cancer: The Fallopian Tube as the Site of Origin and Opportunities for Prevention. Front Oncol 6. https://doi.org/10.3389/fonc.2016.00108

Gil, M., Komorowski, M.P., Seshadri, M., Rokita, H., McGray, A.J.R., Opyrchal, M., Odunsi, K.O., Kozbor, D., 2014. CXCL12/CXCR4 Blockade by Oncolytic Virotherapy Inhibits Ovarian Cancer Growth by Decreasing Immunosuppression and Targeting Cancer Initiating Cells. J Immunol 193, 5327–5337. https://doi.org/10.4049/jimmunol.1400201

Golaraei, A., Cisek, R., Krouglov, S., Navab, R., Niu, C., Sakashita, S., Yasufuku, K., Tsao, M.-S., Wilson, B.C., Barzda, V., 2014. Characterization of collagen in non-small cell lung carcinoma with second harmonic polarization microscopy. Biomed Opt Express 5, 3562–3567. https://doi.org/10.1364/BOE.5.003562

grand-challenges - Home [WWW Document], n.d. URL https://grand-challenge.org/ (accessed 8.20.18).

Grange, C., Lanzardo, S., Cavallo, F., Camussi, G., Bussolati, B., 2008. SCA-1 Identifies the Tumor-Initiating Cells in Mammary Tumors of BALB-neuT Transgenic Mice. Neoplasia 10, 1433–1443.

Greenaway, J., Moorehead, R., Shaw, P., Petrik, J., 2008. Epithelial–stromal interaction increases cell proliferation, survival and tumorigenicity in a mouse model of human epithelial ovarian cancer. Gynecologic Oncology 108, 385–394. https://doi.org/10.1016/j.ygyno.2007.10.035

Grindlay, K., Burns, B., Grossman, D., 2013. Prescription requirements and over-the-counter access to oral contraceptives: a global review. Contraception 88, 91–96. https://doi.org/10.1016/j.contraception.2012.11.021

Guo, Z., Wang, X., Cheng, D., Xia, Z., Luan, M., Zhang, S., 2014. PD-1 Blockade and OX40 Triggering Synergistically Protects against Tumor Growth in a Murine Model of Ovarian Cancer. PLoS One 9. https://doi.org/10.1371/journal.pone.0089350

Gupta, H.B., Clark, C.A., Yuan, B., Sareddy, G., Pandeswara, S., Padron, A.S., Hurez, V., Conejo-Garcia, J., Vadlamudi, R., Li, R., Curiel, T.J., 2016. Tumor cell-intrinsic PD-L1 promotes tumor-initiating cell generation and functions in melanoma and ovarian cancer. Signal Transduction and Targeted Therapy 1, 16030. https://doi.org/10.1038/sigtrans.2016.30

Hamad, N.M., 2002. Distinct requirements for Ras oncogenesis in human versus mouse cells. Genes & Development 16, 2045–2057. https://doi.org/10.1101/gad.993902

Hanahan, D., Weinberg, R.A., 2011. Hallmarks of Cancer: The Next Generation. Cell 144, 646–674. https://doi.org/10.1016/j.cell.2011.02.013

Haraldson, K., Kashuba, V.I., Dmitriev, A.A., Senchenko, V.N., Kudryavtseva, A.V., Pavlova, T.V., Braga, E.A., Pronina, I.V., Kondratov, A.G., Rynditch, A.V., Lerman, M.I., Zabarovsky, E.R., 2012. LRRC3B gene is frequently epigenetically inactivated in several epithelial malignancies and inhibits cell growth and replication. Biochimie 94, 1151–1157. https://doi.org/10.1016/j.biochi.2012.01.019

Harper, E.I., Sheedy, E.F., Stack, M.S., 2018. With Great Age Comes Great Metastatic Ability: Ovarian Cancer and the Appeal of the Aging Peritoneal Microenvironment. Cancers (Basel) 10. https://doi.org/10.3390/cancers10070230
Harris, H.R., Terry, K.L., 2016. Polycystic ovary syndrome and risk of endometrial, ovarian, and breast cancer: a systematic review. Fertility Research and Practice 2, 14. https://doi.org/10.1186/s40738-016-0029-2
Hashimoto, T., Yanaihara, N., Okamoto, A., Nikaido, T., Saito, M., Takakura, S., Yasuda, M., Sasaki, H., Ochiai, K., Tanaka, T., 2011. Cyclin D1 predicts the prognosis of advanced serous ovarian cancer. Experimental and Therapeutic Medicine 2, 213–219. https://doi.org/10.3892/etm.2011.194
Hawkridge, A.M., 2014. The Chicken Model of Spontaneous Ovarian Cancer. Proteomics Clin Appl 8, 689–699. https://doi.org/10.1002/prca.201300135
He, K., Zhang, X., Ren, S., Sun, J., 2015. Deep Residual Learning for Image Recognition. CoRR abs/1512.03385.
Henderson, J.T., Webber, E.M., Sawaya, G.F., 2018. Screening for Ovarian Cancer: Updated Evidence Report and Systematic Review for the US Preventive Services Task Force. JAMA 319, 595–606. https://doi.org/10.1001/jama.2017.21421
Hirakawa, H., Zempo, H., Ogawa, M., Watanabe, R., Suzuki, J., Akazawa, H., Komuro, I., Isobe, M., 2015. A DPP-4 Inhibitor Suppresses Fibrosis and Inflammation on Experimental Autoimmune Myocarditis in Mice. PLoS One 10. https://doi.org/10.1371/journal.pone.0119360
Holmes, C., Stanford, W.L., 2007. Concise review: stem cell antigen-1: expression, function, and enigma. Stem Cells 25, 1339–1347. https://doi.org/10.1634/stemcells.2006-0644
Hou, Z., Ye, Q., Qiu, M., Hao, Y., Han, J., Zeng, H., 2017. Increased activated regulatory T cells proportion correlate with the severity of idiopathic pulmonary fibrosis. Respir Res 18. https://doi.org/10.1186/s12931-017-0653-3
Huang, D.W., Sherman, B.T., Lempicki, R.A., 2009a. Systematic and integrative analysis of large gene lists using DAVID bioinformatics resources. Nat Protoc 4, 44–57. https://doi.org/10.1038/nprot.2008.211
Huang, D.W., Sherman, B.T., Lempicki, R.A., 2009b. Bioinformatics enrichment tools: paths toward the comprehensive functional analysis of large gene lists. Nucleic Acids Res. 37, 1–13. https://doi.org/10.1093/nar/gkn923
Huang, Z., Gao, Y., Wen, W., Li, H., Zheng, W., Shu, X.-O., Beeghly-Fadiel, A., 2015. Contraceptive Methods and Ovarian Cancer Risk among Chinese women: a Report from the Shanghai Women's Health Study. Int J Cancer 137, 607–614. https://doi.org/10.1002/ijc.29412
Hunter, S.M., Gorringe, K.L., Christie, M., Rowley, S.M., Bowtell, D.D., on behalf of the Australian Ovarian Cancer Study Group, Campbell, I.G., 2012. Pre-Invasive Ovarian Mucinous Tumors Are Characterized by CDKN2A and RAS Pathway Aberrations. Clinical Cancer Research 18, 5267–5277. https://doi.org/10.1158/1078-0432.CCR-12-1103
Ince, T.A., Sousa, A.D., Jones, M.A., Harrell, J.C., Agoston, E.S., Krohn, M., Selfors, L.M., Liu, W., Chen, K., Yong, M., Buchwald, P., Wang, B., Hale, K.S., Cohick, E., Sergent, P., Witt, A., Kozhekbaeva, Z., Gao, S., Agoston, A.T., Merritt, M.A., Foster, R., Rueda, B.R., Crum, C.P., Brugge, J.S., Mills, G.B., 2015.

Characterization of twenty-five ovarian tumour cell lines that phenocopy primary tumours. Nature Communications 6. https://doi.org/10.1038/ncomms8419
Jacobs, T.W., Byrne, C., Colditz, G., Connolly, J.L., Schnitt, S.J., 1999. Radial scars in benign breast-biopsy specimens and the risk of breast cancer. N. Engl. J. Med. 340, 430–436. https://doi.org/10.1056/NEJM199902113400604
Jarboe, E., Folkins, A., Nucci, M.R., Kindelberger, D., Drapkin, R., Miron, A., Lee, Y., Crum, C.P., 2008. Serous Carcinogenesis in the Fallopian Tube: A Descriptive Classification. International Journal of Gynecological Pathology 27, 1–9. https://doi.org/10.1097/pgp.0b013e31814b191f
Jones, P.M., Drapkin, R., 2013. Modeling High-Grade Serous Carcinoma: How Converging Insights into Pathogenesis and Genetics are Driving Better Experimental Platforms. Frontiers in Oncology 3. https://doi.org/10.3389/fonc.2013.00217
Karnezis, A.N., Cho, K.R., Gilks, C.B., Pearce, C.L., Huntsman, D.G., 2017. The disparate origins of ovarian cancers: pathogenesis and prevention strategies. Nat. Rev. Cancer 17, 65–74. https://doi.org/10.1038/nrc.2016.113
Keikhosravi, A., Bredfeldt, J.S., Sagar, A.K., Eliceiri, K.W., 2014. Second-harmonic generation imaging of cancer. Methods Cell Biol. 123, 531–546. https://doi.org/10.1016/B978-0-12-420138-5.00028-8
Khan, M.A., Assiri, A.M., Broering, D.C., 2015. Complement and macrophage crosstalk during process of angiogenesis in tumor progression. J Biomed Sci 22. https://doi.org/10.1186/s12929-015-0151-1
Kim, H., Lapointe, J., Kaygusuz, G., Ong, D.E., Li, C., van de Rijn, M., Brooks, J.D., Pollack, J.R., 2005. The Retinoic Acid Synthesis Gene *ALDH1a2* Is a Candidate Tumor Suppressor in Prostate Cancer. Cancer Research 65, 8118–8124. https://doi.org/10.1158/0008-5472.CAN-04-4562
Kirkpatrick, N.D., Brewer, M.A., Utzinger, U., 2007. Endogenous optical biomarkers of ovarian cancer evaluated with multiphoton microscopy. Cancer Epidemiol. Biomarkers Prev. 16, 2048–2057. https://doi.org/10.1158/1055-9965.EPI-07-0009
Kita, Y., Takamura, T., Misu, H., Ota, T., Kurita, S., Takeshita, Y., Uno, M., Matsuzawa-Nagata, N., Kato, K.-I., Ando, H., Fujimura, A., Hayashi, K., Kimura, T., Ni, Y., Otoda, T., Miyamoto, K., Zen, Y., Nakanuma, Y., Kaneko, S., 2012. Metformin prevents and reverses inflammation in a non-diabetic mouse model of nonalcoholic steatohepatitis. PLoS ONE 7, e43056. https://doi.org/10.1371/journal.pone.0043056
Kloudová, K., Hromádková, H., Partlová, S., Brtnický, T., Rob, L., Bartůňková, J., Hensler, M., Halaška, M.J., Špíšek, R., Fialová, A., 2016. Expression of tumor antigens on primary ovarian cancer cells compared to established ovarian cancer cell lines. Oncotarget 7, 46120–46126. https://doi.org/10.18632/oncotarget.10028
Komorowski, M.P., McGray, A.R., Kolakowska, A., Eng, K., Gil, M., Opyrchal, M., Litwinska, B., Nemeth, M.J., Odunsi, K.O., Kozbor, D., 2016. Reprogramming antitumor immunity against chemoresistant ovarian cancer by a CXCR4 antagonist-armed viral oncotherapy. Mol Ther Oncolytics 3, 16034. https://doi.org/10.1038/mto.2016.34

Koshiyama, M., Matsumura, N., Konishi, I., 2017. Subtypes of Ovarian Cancer and Ovarian Cancer Screening. Diagnostics (Basel) 7. https://doi.org/10.3390/diagnostics7010012

Krizhevsky, A., Sutskever, I., Hinton, G.E., 2012. ImageNet Classification with Deep Convolutional Neural Networks, in: Proceedings of the 25th International Conference on Neural Information Processing Systems - Volume 1, NIPS'12. Curran Associates Inc., USA, pp. 1097–1105.

Kroeger, D.R., Milne, K., Nelson, B.H., 2016. Tumor-Infiltrating Plasma Cells Are Associated with Tertiary Lymphoid Structures, Cytolytic T-Cell Responses, and Superior Prognosis in Ovarian Cancer. Clinical Cancer Research 22, 3005–3015. https://doi.org/10.1158/1078-0432.CCR-15-2762

Kulkarni-Datar, K., Orsulic, S., Foster, R., Rueda, B.R., 2013. Ovarian tumor initiating cell populations persist following paclitaxel and carboplatin chemotherapy treatment in vivo. Cancer Letters 339, 237–246. https://doi.org/10.1016/j.canlet.2013.06.014

Kurman, R.J., Shih, I.-M., 2010. The Origin and Pathogenesis of Epithelial Ovarian Cancer- a Proposed Unifying Theory. Am J Surg Pathol 34, 433–443. https://doi.org/10.1097/PAS.0b013e3181cf3d79

Kurman, R.J., Shih, I.-M., 2008. Pathogenesis of Ovarian Cancer. Lessons from Morphology and Molecular Biology and their Clinical Implications. Int J Gynecol Pathol 27, 151–160. https://doi.org/10.1097/PGP.0b013e318161e4f5

Langley, R.R., Fidler, I.J., 2011. The seed and soil hypothesis revisited - the role of tumor-stroma interactions in metastasis to different organs. Int J Cancer 128, 2527–2535. https://doi.org/10.1002/ijc.26031

Laviolette, L.A., Ethier, J.-F., Senterman, M.K., Devine, P.J., Vanderhyden, B.C., 2011. Induction of a menopausal state alters the growth and histology of ovarian tumors in a mouse model of ovarian cancer. Menopause 18, 549–557. https://doi.org/10.1097/gme.0b013e3181fca1b6

Laviolette, L.A., Garson, K., Macdonald, E.A., Senterman, M.K., Courville, K., Crane, C.A., Vanderhyden, B.C., 2010. 17β-Estradiol Accelerates Tumor Onset and Decreases Survival in a Transgenic Mouse Model of Ovarian Cancer. Endocrinology 151, 929–938. https://doi.org/10.1210/en.2009-0602

Lech, M., Anders, H.-J., 2013. Macrophages and fibrosis: How resident and infiltrating mononuclear phagocytes orchestrate all phases of tissue injury and repair. Biochim. Biophys. Acta 1832, 989–997. https://doi.org/10.1016/j.bbadis.2012.12.001

Lee, H., Huttunen, M.J., Hsu, K.-J., Partanen, M., Zhuo, G.-Y., Kauranen, M., Chu, S.-W., 2013. Chiral imaging of collagen by second-harmonic generation circular dichroism. Biomed Opt Express 4, 909–916. https://doi.org/10.1364/BOE.4.000909

Lee, J.-Y., Kim, E.-Y., Jung, K.-W., Shin, A., Chan, K.K.L., Aoki, D., Kim, J.-W., Low, J.J.H., Won, Y.-J., 2014. Trends in gynecologic cancer mortality in East Asian regions. J Gynecol Oncol 25, 174–182. https://doi.org/10.3802/jgo.2014.25.3.174

Lee, S.B., Kalluri, R., 2010. Mechanistic connection between inflammation and fibrosis. Kidney Int Suppl S22–S26. https://doi.org/10.1038/ki.2010.418

Lee, Y., Miron, A., Drapkin, R., Nucci, M., Medeiros, F., Saleemuddin, A., Garber, J., Birch, C., Mou, H., Gordon, R., Cramer, D., McKeon, F., Crum, C., 2007. A candidate precursor to serous carcinoma that originates in the distal fallopian tube. The Journal of Pathology 211, 26–35. https://doi.org/10.1002/path.2091

Leinster, D.A., Kulbe, H., Everitt, G., Thompson, R., Perretti, M., Gavins, F.N.E., Cooper, D., Gould, D., Ennis, D.P., Lockley, M., McNeish, I.A., Nourshargh, S., Balkwill, F.R., 2012. The peritoneal tumour microenvironment of high-grade serous ovarian cancer. J Pathol 227, 136–145. https://doi.org/10.1002/path.4002

Lengyel, E., Burdette, J.E., Kenny, H.A., Matei, D., Pilrose, J., Haluska, P., Nephew, K.P., Hales, D.B., Stack, M.S., 2014. Epithelial ovarian cancer experimental models. Oncogene 33, 3619–3633. https://doi.org/10.1038/onc.2013.321

Li, W., Wang, H., Wang, J., L V, F., Zhu, X., Wang, Z., 2012. Ovarian metastases resection from extragenital primary sites: outcome and prognostic factor analysis of 147 patients. BMC Cancer 12, 278. https://doi.org/10.1186/1471-2407-12-278

Liu, W.-Y., Lin, S.-G., Zhuo, R.-Y., Xie, Y.-Y., Pan, W., Lin, X.-F., Shen, F.-X., 2017. Xenogeneic Decellularized Scaffold: A Novel Platform for Ovary Regeneration. Tissue Eng Part C Methods 23, 61–71. https://doi.org/10.1089/ten.tec.2016.0410

Locke, J.A., Zafarana, G., Malloff, C.A., Lam, W.L., Sykes, J., Pintilie, M., Ramnarine, V.R., Meng, A., Ahmed, O., Jurisica, I., Guns, E.T., van der Kwast, T., Milosevic, M., Bristow, R.G., 2012. Allelic loss of the loci containing the androgen synthesis gene, StAR, is prognostic for relapse in intermediate-risk prostate cancer. The Prostate 72, 1295–1305. https://doi.org/10.1002/pros.22478

Loughran, E.A., Leonard, A.K., Hilliard, T.S., Phan, R.C., Yemc, M.G., Harper, E., Sheedy, E., Klymenko, Y., Asem, M., Liu, Y., Yang, J., Johnson, J., Tarwater, L., Shi, Z., Leevy, M., Ravosa, M.J., Stack, M.S., 2018. Aging Increases Susceptibility to Ovarian Cancer Metastasis in Murine Allograft Models and Alters Immune Composition of Peritoneal Adipose Tissue. Neoplasia 20, 621–631. https://doi.org/10.1016/j.neo.2018.03.007

Lv, L., Zhang, T., Yi, Q., Huang, Y., Wang, Z., Hou, H., Zhang, H., Zheng, W., Hao, Q., Guo, Z., Cooke, H.J., Shi, Q., 2012. Tetraploid cells from cytokinesis failure induce aneuploidy and spontaneous transformation of mouse ovarian surface epithelial cells. Cell Cycle 11, 2864–2875. https://doi.org/10.4161/cc.21196

Makabe, S., Motta, P.M., Naguro, T., Vizza, E., Perrone, G., Zichella, L., 1998. Microanatomy of the female reproductive organs in postmenopause by scanning electron microscopy. Climacteric 1, 63–71.

Mani, S.A., Guo, W., Liao, M.-J., Eaton, E.N., Ayyanan, A., Zhou, A.Y., Brooks, M., Reinhard, F., Zhang, C.C., Shipitsin, M., Campbell, L.L., Polyak, K., Brisken, C., Yang, J., Weinberg, R.A., 2008. The epithelial-mesenchymal transition generates cells with properties of stem cells. Cell 133, 704–715. https://doi.org/10.1016/j.cell.2008.03.027

Mannis, G.N., Fehniger, J.E., Creasman, J.S., Jacoby, V.L., Beattie, M.S., 2013. Risk-Reducing Salpingo-oophorectomy and Ovarian Cancer Screening in 1077 Women After BRCA Testing. JAMA Intern Med 173, 96–103. https://doi.org/10.1001/2013.jamainternmed.962

Mantovani, A., Sozzani, S., Locati, M., Allavena, P., Sica, A., 2002. Macrophage polarization: tumor-associated macrophages as a paradigm for polarized M2 mononuclear phagocytes. Trends Immunol. 23, 549–555.

Marchetti, C., De Felice, F., Palaia, I., Perniola, G., Musella, A., Musio, D., Muzii, L., Tombolini, V., Panici, P.B., 2014. Risk-reducing salpingo-oophorectomy: a meta-analysis on impact on ovarian cancer risk and all cause mortality in BRCA 1 and BRCA 2 mutation carriers. BMC Womens Health 14. https://doi.org/10.1186/s12905-014-0150-5

Martin, S.D., Brown, S.D., Wick, D.A., Nielsen, J.S., Kroeger, D.R., Twumasi-Boateng, K., Holt, R.A., Nelson, B.H., 2016. Low Mutation Burden in Ovarian Cancer May Limit the Utility of Neoantigen-Targeted Vaccines. PLOS ONE 11, e0155189. https://doi.org/10.1371/journal.pone.0155189

Matheus, L.H.G., Simão, G.M., Amaral, T.A., Brito, R.B.O., Malta, C.S., Matos, Y.S.T., Santana, A.C., Rodrigues, G.G.C., Albejante, M.C., Bach, E.E., Dalboni, M.A., Camacho, C.P., Dellê, H., 2017. Indoleamine 2, 3-dioxygenase (IDO) increases during renal fibrogenesis and its inhibition potentiates TGF-β 1-induced epithelial to mesenchymal transition. BMC Nephrology 18. https://doi.org/10.1186/s12882-017-0702-7

McCloskey, C.W., Goldberg, R.L., Carter, L.E., Gamwell, L.F., Al-Hujaily, E.M., Collins, O., Macdonald, E.A., Garson, K., Daneshmand, M., Carmona, E., Vanderhyden, B.C., 2014. A New Spontaneously Transformed Syngeneic Model of High-Grade Serous Ovarian Cancer with a Tumor-Initiating Cell Population. Front. Oncol. 4. https://doi.org/10.3389/fonc.2014.00053

McCloskey, C.W., Rodriguez, G.M., Galpin, K.J.C., Vanderhyden, B.C., 2018. Ovarian Cancer Immunotherapy: Preclinical Models and Emerging Therapeutics. Cancers (Basel) 10. https://doi.org/10.3390/cancers10080244

McGranahan, N., Furness, A.J.S., Rosenthal, R., Ramskov, S., Lyngaa, R., Saini, S.K., Jamal-Hanjani, M., Wilson, G.A., Birkbak, N.J., Hiley, C.T., Watkins, T.B.K., Shafi, S., Murugaesu, N., Mitter, R., Akarca, A.U., Linares, J., Marafioti, T., Henry, J.Y., Allen, E.M.V., Miao, D., Schilling, B., Schadendorf, D., Garraway, L.A., Makarov, V., Rizvi, N.A., Snyder, A., Hellmann, M.D., Merghoub, T., Wolchok, J.D., Shukla, S.A., Wu, C.J., Peggs, K.S., Chan, T.A., Hadrup, S.R., Quezada, S.A., Swanton, C., 2016. Clonal neoantigens elicit T cell immunoreactivity and sensitivity to immune checkpoint blockade. Science 351, 1463–1469. https://doi.org/10.1126/science.aaf1490

McLean, K., Mehta, G., 2017. Tumor Microenvironment and Models of Ovarian Cancer: The 11th Biennial Rivkin Center Ovarian Cancer Research Symposium. International Journal of Gynecological Cancer 1. https://doi.org/10.1097/IGC.0000000000001119

McNeal, S., Bitterman, P., Bahr, J.M., Edassery, S.L., Abramowicz, J.S., Basu, S., Barua, A., 2016. Association of Immunosuppression with DR6 Expression during the Development and Progression of Spontaneous Ovarian Cancer in Laying Hen Model [WWW Document]. Journal of Immunology Research. https://doi.org/10.1155/2016/6729379

Menon, U., Karpinskyj, C., Gentry-Maharaj, A., 2018. Ovarian Cancer Prevention and Screening. Obstet Gynecol 131, 909–927. https://doi.org/10.1097/AOG.0000000000002580

Miyoshi, I., Takahashi, K., Kon, Y., Okamura, T., Mototani, Y., Araki, Y., Kasai, N., 2002. Mouse transgenic for murine oviduct-specific glycoprotein promoter-driven simian virus 40 large T-antigen: tumor formation and its hormonal regulation. Mol. Reprod. Dev. 63, 168–176. https://doi.org/10.1002/mrd.10175

Mo, L., Bachelder, R.E., Kennedy, M., Chen, P.-H., Chi, J.-T., Berchuck, A., Cianciolo, G., Pizzo, S.V., 2015. Syngeneic Murine Ovarian Cancer Model Reveals That Ascites Enriches for Ovarian Cancer Stem-Like Cells Expressing Membrane GRP78. Mol. Cancer Ther. 14, 747–756. https://doi.org/10.1158/1535-7163.MCT-14-0579

Moradi, H., Ahmad, A., Shepherdson, D., Vuong, N.H., Niedbala, G., Eapen, L., Vanderhyden, B., Nyiri, B., Murugkar, S., 2017. Raman micro-spectroscopy applied to treatment resistant and sensitive human ovarian cancer cells. J Biophotonics 10, 1327–1334. https://doi.org/10.1002/jbio.201600211

Morin, P.J., Weeraratna, A.T., 2016. Genetically-defined ovarian cancer mouse models. J. Pathol. 238, 180–184. https://doi.org/10.1002/path.4663

Mostaço-Guidolin, L.B., Ko, A.C.-T., Wang, F., Xiang, B., Hewko, M., Tian, G., Major, A., Shiomi, M., Sowa, M.G., 2013. Collagen morphology and texture analysis: from statistics to classification. Sci Rep 3, 2190. https://doi.org/10.1038/srep02190

Munn, D.H., Mellor, A.L., 2016. IDO in the Tumor Microenvironment: Inflammation, Counter-Regulation, and Tolerance. Trends Immunol. 37, 193–207. https://doi.org/10.1016/j.it.2016.01.002

Nadiarnykh, O., LaComb, R.B., Brewer, M.A., Campagnola, P.J., 2010. Alterations of the extracellular matrix in ovarian cancer studied by Second Harmonic Generation imaging microscopy. BMC Cancer 10, 94. https://doi.org/10.1186/1471-2407-10-94

Nakamura, K., Igarashi, K., Ohkawa, R., Yokota, H., Masuda, A., Nakagawa, S., Yano, T., Ikeda, H., Aoki, J., Yatomi, Y., 2012. Serum Autotaxin is not a Useful Biomarker for Ovarian Cancer. Lipids 47, 927–930. https://doi.org/10.1007/s11745-012-3691-0

Nargund, G., 2009. Declining birth rate in Developed Countries: A radical policy re-think is required. Facts Views Vis Obgyn 1, 191–193.

National Cancer Institute, 2018. Cancer Stat Facts: Ovarian Cancer [WWW Document]. URL https://seer.cancer.gov/statfacts/html/ovary.html (accessed 8.15.18).

Nebgen, D.R., Hurteau, J., Holman, L.L., Bradford, A., Munsell, M.F., Soletsky, B.R., Sun, C.C., Chisholm, G.B., Lu, K.H., 2018. Bilateral salpingectomy with delayed oophorectomy for ovarian cancer risk reduction: A pilot study in women with BRCA1/2 mutations. Gynecol. Oncol. 150, 79–84. https://doi.org/10.1016/j.ygyno.2018.04.564

Necchi, A., Miceli, R., Oualla, K., Sonpavde, G., Giannatempo, P., Raggi, D., Nicolai, N., Boffi, R., Busia, A., Mariani, L., Salvioni, R., 2017. Effect of Bleomycin Administration on the Development of Pulmonary Toxicity in Patients With Metastatic Germ Cell Tumors Receiving First-Line Chemotherapy: A Meta-

Analysis of Randomized Studies. Clinical Genitourinary Cancer 15, 213-220.e5. https://doi.org/10.1016/j.clgc.2016.08.021
Nelson, B.H., 2008. The impact of T-cell immunity on ovarian cancer outcomes. Immunol. Rev. 222, 101–116. https://doi.org/10.1111/j.1600-065X.2008.00614.x
Ness, R.B., Dodge, R.C., Edwards, R.P., Baker, J.A., Moysich, K.B., 2011. Contraception Methods, beyond Oral Contraceptives and Tubal Ligation, and Risk of Ovarian Cancer. Ann Epidemiol 21, 188–196. https://doi.org/10.1016/j.annepidem.2010.10.002
Nielsen, S.R., Quaranta, V., Linford, A., Emeagi, P., Rainer, C., Santos, A., Ireland, L., Sakai, T., Sakai, K., Kim, Y.-S., Engle, D., Campbell, F., Palmer, D., Ko, J.H., Tuveson, D.A., Hirsch, E., Mielgo, A., Schmid, M.C., 2016. Macrophage-secreted granulin supports pancreatic cancer metastasis by inducing liver fibrosis. Nat Cell Biol 18, 549–560. https://doi.org/10.1038/ncb3340
Notaridou, M., Quaye, L., Dafou, D., Jones, C., Song, H., Høgdall, E., Kjaer, S.K., Christensen, L., Høgdall, C., Blaakaer, J., McGuire, V., Wu, A.H., Van Den Berg, D.J., Pike, M.C., Gentry-Maharaj, A., Wozniak, E., Sher, T., Jacobs, I.J., Tyrer, J., Schildkraut, J.M., Moorman, P.G., Iversen, E.S., Jakubowska, A., Mędrek, K., Lubiński, J., Ness, R.B., Moysich, K.B., Lurie, G., Wilkens, L.R., Carney, M.E., Wang-Gohrke, S., Doherty, J.A., Rossing, M.A., Beckmann, M.W., Thiel, F.C., Ekici, A.B., Chen, X., Beesley, J., The Australian Ovarian Cancer Study Group/Australian Cancer Study (Ovarian Cancer), Gronwald, J., Fasching, P.A., Chang-Claude, J., Goodman, M.T., Chenevix-Trench, G., Berchuck, A., Pearce, C.L., Whittemore, A.S., Menon, U., Pharoah, P.D.P., Gayther, S.A., Ramus, S.J., on behalf of the Ovarian Cancer Association Consortium, 2011. Common alleles in candidate susceptibility genes associated with risk and development of epithelial ovarian cancer. International Journal of Cancer 128, 2063–2074. https://doi.org/10.1002/ijc.25554
Nounamo, B., Liem, J., Cannon, M., Liu, J., 2017. Myxoma Virus Optimizes Cisplatin for the Treatment of Ovarian Cancer In Vitro and in a Syngeneic Murine Dissemination Model. Molecular Therapy - Oncolytics 6, 90–99. https://doi.org/10.1016/j.omto.2017.08.002
Okochi-Takada, E., Nakazawa, K., Wakabayashi, M., Mori, A., Ichimura, S., Yasugi, T., Ushijima, T., 2006. Silencing of theUCHL1 gene in human colorectal and ovarian cancers. International Journal of Cancer 119, 1338–1344. https://doi.org/10.1002/ijc.22025
Olaso, E., Santisteban, A., Bidaurrazaga, J., Gressner, A.M., Rosenbaum, J., Vidal-Vanaclocha, F., 1997. Tumor-dependent activation of rodent hepatic stellate cells during experimental melanoma metastasis. Hepatology 26, 634–642. https://doi.org/10.1002/hep.510260315
Oliveros, J.C, 2007. Venny. An interactive tool for comparing lists with Venn's diagrams [WWW Document]. Venny. An interactive tool for comparing lists with Venn's diagrams. URL http://bioinfogp.cnb.csic.es/tools/venny/ (accessed 8.15.18).
Orsulic, S., Li, Y., Soslow, R.A., Vitale-Cross, L.A., Gutkind, J.S., Varmus, H.E., 2002. Induction of ovarian cancer by defined multiple genetic changes in a mouse model system. Cancer Cell 1, 53–62.

Ozdemir, F., Altinisik, J., Karateke, A., Coksuer, H., Buyru, N., 2012. Methylation of tumor suppressor genes in ovarian cancer. Experimental and Therapeutic Medicine 4, 1092–1096. https://doi.org/10.3892/etm.2012.715

P. Fotheringham, A., Davies, I., 1980. Age related accumulation of intranuclear membranous inclusions in female mice. Journal of the American Aging Association 3, 1–5. https://doi.org/10.1007/BF02434998

Padilla-Nash, H.M., McNeil, N.E., Yi, M., Nguyen, Q.-T., Hu, Y., Wangsa, D., Mack, D.L., Hummon, A.B., Case, C., Cardin, E., Stephens, R., Difilippantonio, M.J., Ried, T., 2013. Aneuploidy, oncogene amplification and epithelial to mesenchymal transition define spontaneous transformation of murine epithelial cells. Carcinogenesis 34, 1929–1939. https://doi.org/10.1093/carcin/bgt138

Park, J.W., Park, J.M., Park, D.M., Kim, D.-Y., Kim, H.K., 2016. Stem Cells Antigen-1 Enriches for a Cancer Stem Cell-Like Subpopulation in Mouse Gastric Cancer. Stem Cells 34, 1177–1187. https://doi.org/10.1002/stem.2329

Parte, S.C., Batra, S.K., Kakar, S.S., 2018. Characterization of stem cell and cancer stem cell populations in ovary and ovarian tumors. J Ovarian Res 11, 69. https://doi.org/10.1186/s13048-018-0439-3

Perets, R., Wyant, G.A., Muto, K.W., Bijron, J.G., Poole, B.B., Chin, K.T., Chen, J.Y.H., Ohman, A.W., Stepule, C.D., Kwak, S., Karst, A.M., Hirsch, M.S., Setlur, S.R., Crum, C.P., Dinulescu, D.M., Drapkin, R., 2013. Transformation of the Fallopian Tube Secretory Epithelium Leads to High-grade Serous Ovarian Cancer in Brca;Tp53;Pten Models. Cancer Cell 24, 751–765. https://doi.org/10.1016/j.ccr.2013.10.013

Perheentupa, A., Huhtaniemi, I., 2009. Aging of the human ovary and testis. Mol. Cell. Endocrinol. 299, 2–13. https://doi.org/10.1016/j.mce.2008.11.004

Picatoste, B., Ramírez, E., Caro-Vadillo, A., Iborra, C., Egido, J., Tuñón, J., Lorenzo, Ó., 2013. Sitagliptin Reduces Cardiac Apoptosis, Hypertrophy and Fibrosis Primarily by Insulin-Dependent Mechanisms in Experimental type-II Diabetes. Potential Roles of GLP-1 Isoforms. PLOS ONE 8, e78330. https://doi.org/10.1371/journal.pone.0078330

Piek, J.M.J., van Diest, P.J., Zweemer, R.P., Jansen, J.W., Poort-Keesom, R.J.J., Menko, F.H., Gille, J.J.P., Jongsma, A.P.M., Pals, G., Kenemans, P., Verheijen, R.H.M., 2001. Dysplastic changes in prophylactically removed Fallopian tubes of women predisposed to developing ovarian cancer. The Journal of Pathology 195, 451–456. https://doi.org/10.1002/path.1000

Prat, J., 2012. New insights into ovarian cancer pathology. Ann. Oncol. 23 Suppl 10, x111-117. https://doi.org/10.1093/annonc/mds300

Provenzano, P.P., Inman, D.R., Eliceiri, K.W., Knittel, J.G., Yan, L., Rueden, C.T., White, J.G., Keely, P.J., 2008. Collagen density promotes mammary tumor initiation and progression. BMC Med 6, 11. https://doi.org/10.1186/1741-7015-6-11

Quatromoni, J.G., Eruslanov, E., 2012. Tumor-associated macrophages: function, phenotype, and link to prognosis in human lung cancer. Am J Transl Res 4, 376–389.

Quinn, M.C.J., Filali-Mouhim, A., Provencher, D.M., Mes-Masson, A.-M., Tonin, P.N., 2009. Reprogramming of the transcriptome in a novel chromosome 3 transfer

tumor suppressor ovarian cancer cell line model affected molecular networks that are characteristic of ovarian cancer. Molecular Carcinogenesis 48, 648–661. https://doi.org/10.1002/mc.20511

Raja, F.A., Counsell, N., Colombo, N., Pfisterer, J., du Bois, A., Parmar, M.K., Vergote, I.B., Gonzalez-Martin, A., Alberts, D.S., Plante, M., Torri, V., Ledermann, J.A., 2013. Platinum versus platinum-combination chemotherapy in platinum-sensitive recurrent ovarian cancer: a meta-analysis using individual patient data. Ann Oncol 24, 3028–3034. https://doi.org/10.1093/annonc/mdt406

Rangarajan, A., Hong, S.J., Gifford, A., Weinberg, R.A., 2004. Species- and cell type-specific requirements for cellular transformation. Cancer Cell 6, 171–183. https://doi.org/10.1016/j.ccr.2004.07.009

Rebbeck, T.R., Kauff, N.D., Domchek, S.M., 2009. Meta-analysis of Risk Reduction Estimates Associated With Risk-Reducing Salpingo-oophorectomy in BRCA1 or BRCA2 Mutation Carriers. J Natl Cancer Inst 101, 80–87. https://doi.org/10.1093/jnci/djn442

Rebbeck, T.R., Mitra, N., Wan, F., Sinilnikova, O.M., Healey, S., McGuffog, L., Mazoyer, S., Chenevix-Trench, G., Easton, D.F., Antoniou, A.C., Nathanson, K.L., CIMBA Consortium, Laitman, Y., Kushnir, A., Paluch-Shimon, S., Berger, R., Zidan, J., Friedman, E., Ehrencrona, H., Stenmark-Askmalm, M., Einbeigi, Z., Loman, N., Harbst, K., Rantala, J., Melin, B., Huo, D., Olopade, O.I., Seldon, J., Ganz, P.A., Nussbaum, R.L., Chan, S.B., Odunsi, K., Gayther, S.A., Domchek, S.M., Arun, B.K., Lu, K.H., Mitchell, G., Karlan, B.Y., Walsh, C., Lester, J., Godwin, A.K., Pathak, H., Ross, E., Daly, M.B., Whittemore, A.S., John, E.M., Miron, A., Terry, M.B., Chung, W.K., Goldgar, D.E., Buys, S.S., Janavicius, R., Tihomirova, L., Tung, N., Dorfling, C.M., van Rensburg, E.J., Steele, L., Neuhausen, S.L., Ding, Y.C., Ejlertsen, B., Gerdes, A.-M., Hansen, T. v O., Ramón y Cajal, T., Osorio, A., Benitez, J., Godino, J., Tejada, M.-I., Duran, M., Weitzel, J.N., Bobolis, K.A., Sand, S.R., Fontaine, A., Savarese, A., Pasini, B., Peissel, B., Bonanni, B., Zaffaroni, D., Vignolo-Lutati, F., Scuvera, G., Giannini, G., Bernard, L., Genuardi, M., Radice, P., Dolcetti, R., Manoukian, S., Pensotti, V., Gismondi, V., Yannoukakos, D., Fostira, F., Garber, J., Torres, D., Rashid, M.U., Hamann, U., Peock, S., Frost, D., Platte, R., Evans, D.G., Eeles, R., Davidson, R., Eccles, D., Cole, T., Cook, J., Brewer, C., Hodgson, S., Morrison, P.J., Walker, L., Porteous, M.E., Kennedy, M.J., Izatt, L., Adlard, J., Donaldson, A., Ellis, S., Sharma, P., Schmutzler, R.K., Wappenschmidt, B., Becker, A., Rhiem, K., Hahnen, E., Engel, C., Meindl, A., Engert, S., Ditsch, N., Arnold, N., Plendl, H.J., Mundhenke, C., Niederacher, D., Fleisch, M., Sutter, C., Bartram, C.R., Dikow, N., Wang-Gohrke, S., Gadzicki, D., Steinemann, D., Kast, K., Beer, M., Varon-Mateeva, R., Gehrig, A., Weber, B.H., Stoppa-Lyonnet, D., Sinilnikova, O.M., Mazoyer, S., Houdayer, C., Belotti, M., Gauthier-Villars, M., Damiola, F., Boutry-Kryza, N., Lasset, C., Sobol, H., Peyrat, J.-P., Muller, D., Fricker, J.-P., Collonge-Rame, M.-A., Mortemousque, I., Nogues, C., Rouleau, E., Isaacs, C., De Paepe, A., Poppe, B., Claes, K., De Leeneer, K., Piedmonte, M., Rodriguez, G., Wakely, K., Boggess, J., Blank, S.V., Basil, J., Azodi, M., Phillips, K.-A., Caldes, T., de la Hoya, M., Romero, A., Nevanlinna, H., Aittomäki, K., van der Hout, A.H., Hogervorst, F.B.L., Verhoef, S., Collée, J.M., Seynaeve, C.,

Oosterwijk, J.C., Gille, J.J.P., Wijnen, J.T., Gómez Garcia, E.B., Kets, C.M., Ausems, M.G.E.M., Aalfs, C.M., Devilee, P., Mensenkamp, A.R., Kwong, A., Olah, E., Papp, J., Diez, O., Lazaro, C., Darder, E., Blanco, I., Salinas, M., Jakubowska, A., Lubinski, J., Gronwald, J., Jaworska-Bieniek, K., Durda, K., Sukiennicki, G., Huzarski, T., Byrski, T., Cybulski, C., Toloczko-Grabarek, A., Złowocka-Perłowska, E., Menkiszak, J., Arason, A., Barkardottir, R.B., Simard, J., Laframboise, R., Montagna, M., Agata, S., Alducci, E., Peixoto, A., Teixeira, M.R., Spurdle, A.B., Lee, M.H., Park, S.K., Kim, S.-W., Friebel, T.M., Couch, F.J., Lindor, N.M., Pankratz, V.S., Guidugli, L., Wang, X., Tischkowitz, M., Foretova, L., Vijai, J., Offit, K., Robson, M., Rau-Murthy, R., Kauff, N., Fink-Retter, A., Singer, C.F., Rappaport, C., Gschwantler-Kaulich, D., Pfeiler, G., Tea, M.-K., Berger, A., Greene, M.H., Mai, P.L., Imyanitov, E.N., Toland, A.E., Senter, L., Bojesen, A., Pedersen, I.S., Skytte, A.-B., Sunde, L., Thomassen, M., Moeller, S.T., Kruse, T.A., Jensen, U.B., Caligo, M.A., Aretini, P., Teo, S.-H., Selkirk, C.G., Hulick, P.J., Andrulis, I., 2015. Association of type and location of BRCA1 and BRCA2 mutations with risk of breast and ovarian cancer. JAMA 313, 1347–1361. https://doi.org/10.1001/jama.2014.5985

Rena, G., Hardie, D.G., Pearson, E.R., 2017. The mechanisms of action of metformin. Diabetologia 60, 1577–1585. https://doi.org/10.1007/s00125-017-4342-z

Rho, S.B., Dong, S.M., Kang, S., Seo, S.-S., Yoo, C.W., Lee, D.O., Woo, J.S., Park, S.-Y., 2008. Insulin-like growth factor-binding protein-5 (IGFBP-5) acts as a tumor suppressor by inhibiting angiogenesis. Carcinogenesis 29, 2106–2111. https://doi.org/10.1093/carcin/bgn206

Ricard-Blum, S., Baffet, G., Théret, N., 2018. Molecular and tissue alterations of collagens in fibrosis. Matrix Biol. 68–69, 122–149. https://doi.org/10.1016/j.matbio.2018.02.004

Ricci, F., Broggini, M., Damia, G., 2013. Revisiting ovarian cancer preclinical models: Implications for a better management of the disease. Cancer Treatment Reviews 39, 561–568. https://doi.org/10.1016/j.ctrv.2013.01.005

Rinkevich, Y., Walmsley, G.G., Hu, M.S., Maan, Z.N., Newman, A.M., Drukker, M., Januszyk, M., Krampitz, G.W., Gurtner, G.C., Lorenz, H.P., Weissman, I.L., Longaker, M.T., 2015. Skin fibrosis. Identification and isolation of a dermal lineage with intrinsic fibrogenic potential. Science 348, aaa2151. https://doi.org/10.1126/science.aaa2151

Roberts, P.C., Mottillo, E.P., Baxa, A.C., Heng, H.H.Q., Doyon-Reale, N., Gregoire, L., Lancaster, W.D., Rabah, R., Schmelz, E.M., 2005. Sequential molecular and cellular events during neoplastic progression: a mouse syngeneic ovarian cancer model. Neoplasia 7, 944–956.

Roby, K.F., Taylor, C.C., Sweetwood, J.P., Cheng, Y., Pace, J.L., Tawfik, O., Persons, D.L., Smith, P.G., Terranova, P.F., 2000. Development of a syngeneic mouse model for events related to ovarian cancer. Carcinogenesis 21, 585–591.

Rodriguez, G.M., Galpin, K.J.C., McCloskey, C.W., Vanderhyden, B.C., 2018. The Tumor Microenvironment of Epithelial Ovarian Cancer and Its Influence on Response to Immunotherapy. Cancers (Basel) 10. https://doi.org/10.3390/cancers10080242

Rose, G.S., Tocco, L.M., Granger, G.A., DiSaia, P.J., Hamilton, T.C., Santin, A.D., Hiserodt, J.C., 1996. Development and characterization of a clinically useful animal model of epithelial ovarian cancer in the Fischer 344 rat. Am. J. Obstet. Gynecol. 175, 593–599.

Rouède, D., Schaub, E., Bellanger, J.-J., Ezan, F., Scimeca, J.-C., Baffet, G., Tiaho, F., 2017. Determination of extracellular matrix collagen fibril architectures and pathological remodeling by polarization dependent second harmonic microscopy. Sci Rep 7, 12197. https://doi.org/10.1038/s41598-017-12398-0

Roy, L., Cowden Dahl, K.D., 2018. Can Stemness and Chemoresistance Be Therapeutically Targeted via Signaling Pathways in Ovarian Cancer? Cancers (Basel) 10. https://doi.org/10.3390/cancers10080241

Rumelhart, D.E., Hinton, G.E., Williams, R.J., 1988. Neurocomputing: Foundations of Research, in: Anderson, J.A., Rosenfeld, E. (Eds.), . MIT Press, Cambridge, MA, USA, pp. 696–699.

Russakovsky, O., Deng, J., Su, H., Krause, J., Satheesh, S., Ma, S., Huang, Z., Karpathy, A., Khosla, A., Bernstein, M., Berg, A.C., Fei-Fei, L., 2014. ImageNet Large Scale Visual Recognition Challenge. arXiv:1409.0575 [cs].

Russo, A., Czarnecki, A.A., Dean, M., Modi, D.A., Lantvit, D.D., Hardy, L., Baligod, S., Davis, D.A., Wei, J.-J., Burdette, J.E., 2018. PTEN loss in the fallopian tube induces hyperplasia and ovarian tumor formation. Oncogene 37, 1976–1990. https://doi.org/10.1038/s41388-017-0097-8

Salazar, H., Godwin, A.K., Daly, M.B., Laub, P.B., Hogan, W.M., Rosenblum, N., Boente, M.P., Lynch, H.T., Hamilton, T.C., 1996. Microscopic benign and invasive malignant neoplasms and a cancer-prone phenotype in prophylactic oophorectomies. J. Natl. Cancer Inst. 88, 1810–1820.

Sato, E., Nakayama, K., Ishikawa, M., Nakamura, K., Ishibashi, T., Kyo, S., 2017. High-grade serous ovarian cancer 3 years after bilateral salpingectomy: A case report. Mol Clin Oncol 6, 201–203. https://doi.org/10.3892/mco.2016.1105

Sato, N., Takasaka, N., Yoshida, M., Tsubouchi, K., Minagawa, S., Araya, J., Saito, N., Fujita, Y., Kurita, Y., Kobayashi, K., Ito, S., Hara, H., Kadota, T., Yanagisawa, H., Hashimoto, M., Utsumi, H., Wakui, H., Kojima, J., Numata, T., Kaneko, Y., Odaka, M., Morikawa, T., Nakayama, K., Kohrogi, H., Kuwano, K., 2016. Metformin attenuates lung fibrosis development via NOX4 suppression. Respir. Res. 17, 107. https://doi.org/10.1186/s12931-016-0420-x

Sau, A., Lau, R., Cabrita, M.A., Nolan, E., Crooks, P.A., Visvader, J.E., Pratt, M.A.C., 2016. Persistent Activation of NF-κB in BRCA1-Deficient Mammary Progenitors Drives Aberrant Proliferation and Accumulation of DNA Damage. Cell Stem Cell 19, 52–65. https://doi.org/10.1016/j.stem.2016.05.003

Savant, S.S., Sriramkumar, S., O'Hagan, H.M., 2018. The Role of Inflammation and Inflammatory Mediators in the Development, Progression, Metastasis, and Chemoresistance of Epithelial Ovarian Cancer. Cancers (Basel) 10. https://doi.org/10.3390/cancers10080251

Schildkraut, J.M., Schwingl, P.J., Bastos, E., Evanoff, A., Hughes, C., 1996. Epithelial ovarian cancer risk among women with polycystic ovary syndrome. Obstet Gynecol 88, 554–559.

Scurr, L.L., Guminski, A.D., Chiew, Y.-E., Balleine, R.L., Sharma, R., Lei, Y., Pryor, K., Wain, G.V., Brand, A., Byth, K., Kennedy, C., Rizos, H., Harnett, P.R., deFazio, A., 2008. Ankyrin Repeat Domain 1, ANKRD1, a Novel Determinant of Cisplatin Sensitivity Expressed in Ovarian Cancer. Clinical Cancer Research 14, 6924–6932. https://doi.org/10.1158/1078-0432.CCR-07-5189

Sengupta, A., Cancelas, J.A., 2010. Cancer stem cells: A stride towards cancer cure? Journal of Cellular Physiology 225, 7–14. https://doi.org/10.1002/jcp.22213

Shafiee, M.N., Khan, G., Ariffin, R., Abu, J., Chapman, C., Deen, S., Nunns, D., Barrett, D.A., Seedhouse, C., Atiomo, W., 2014. Preventing endometrial cancer risk in polycystic ovarian syndrome (PCOS) women: could metformin help? Gynecol. Oncol. 132, 248–253. https://doi.org/10.1016/j.ygyno.2013.10.028

Sharma, M., Beckley, N., Nazareth, I., Petersen, I., 2017. Effectiveness of sitagliptin compared to sulfonylureas for type 2 diabetes mellitus inadequately controlled on metformin: a systematic review and meta-analysis. BMJ Open 7, e017260. https://doi.org/10.1136/bmjopen-2017-017260

Shaw, T.J., Senterman, M.K., Dawson, K., Crane, C.A., Vanderhyden, B.C., 2004. Characterization of intraperitoneal, orthotopic, and metastatic xenograft models of human ovarian cancer. Mol. Ther. 10, 1032–1042. https://doi.org/10.1016/j.ymthe.2004.08.013

Sherman-Baust, C.A., Kuhn, E., Valle, B.L., Shih, I.-M., Kurman, R.J., Wang, T.-L., Amano, T., Ko, M.S.H., Miyoshi, I., Araki, Y., Lehrmann, E., Zhang, Y., Becker, K.G., Morin, P.J., 2014. A genetically engineered ovarian cancer mouse model based on fallopian tube transformation mimics human high-grade serous carcinoma development. J Pathol 233, 228–237. https://doi.org/10.1002/path.4353

Shetzer, Y., Solomon, H., Koifman, G., Molchadsky, A., Horesh, S., Rotter, V., 2014. The paradigm of mutant p53-expressing cancer stem cells and drug resistance. Carcinogenesis 35, 1196–1208. https://doi.org/10.1093/carcin/bgu073

Shigdar, S., Li, Y., Bhattacharya, S., O'Connor, M., Pu, C., Lin, J., Wang, T., Xiang, D., Kong, L., Wei, M.Q., Zhu, Y., Zhou, S., Duan, W., 2014. Inflammation and cancer stem cells. Cancer Lett. 345, 271–278. https://doi.org/10.1016/j.canlet.2013.07.031

Siegel, R.L., Miller, K.D., Jemal, A., 2016. Cancer statistics, 2016. CA Cancer J Clin 66, 7–30. https://doi.org/10.3322/caac.21332

Sigl, V., Owusu-Boaitey, K., Joshi, P.A., Kavirayani, A., Wirnsberger, G., Novatchkova, M., Kozieradzki, I., Schramek, D., Edokobi, N., Hersl, J., Sampson, A., Odai-Afotey, A., Lazaro, C., Gonzalez-Suarez, E., Pujana, M.A., CIMBA, for, Heyn, H., Vidal, E., Cruickshank, J., Berman, H., Sarao, R., Ticevic, M., Uribesalgo, I., Tortola, L., Rao, S., Tan, Y., Pfeiler, G., Lee, E.Y., Bago-Horvath, Z., Kenner, L., Popper, H., Singer, C., Khokha, R., Jones, L.P., Penninger, J.M., 2016. RANKL/RANK control Brca1 mutation-driven mammary tumors. Cell Res 26, 761–774. https://doi.org/10.1038/cr.2016.69

Simonyan, K., Zisserman, A., 2014. Very Deep Convolutional Networks for Large-Scale Image Recognition. CoRR abs/1409.1556.

Smith, E.R., Xu, X.-X., 2008. Ovarian ageing, follicle depletion, and cancer: a hypothesis for the aetiology of epithelial ovarian cancer involving follicle depletion. Lancet Oncol 9, 1108–1111. https://doi.org/10.1016/S1470-2045(08)70281-X

Smith, E.R., Yeasky, T., Wei, J.Q., Miki, R.A., Cai, K.Q., Smedberg, J.L., Yang, W.-L., Xu, X.-X., 2012. White spotting variant mouse as an experimental model for ovarian aging and menopausal biology. Menopause 19, 588–596. https://doi.org/10.1097/gme.0b013e318239cc53

Son, D.-S., Kabir, S.M., Dong, Y.-L., Lee, E., Adunyah, S.E., 2012. Inhibitory Effect of Tumor Suppressor p53 on Proinflammatory Chemokine Expression in Ovarian Cancer Cells by Reducing Proteasomal Degradation of IκB. PLoS One 7. https://doi.org/10.1371/journal.pone.0051116

Sopik, V., Iqbal, J., Rosen, B., Narod, S.A., 2015. Why have ovarian cancer mortality rates declined? Part I. Incidence. Gynecol. Oncol. 138, 741–749. https://doi.org/10.1016/j.ygyno.2015.06.017

Soslow, R.A., 2008. Histologic Subtypes of Ovarian Carcinoma: An Overview. International Journal of Gynecological Pathology PAP. https://doi.org/10.1097/PGP.0b013e31815ea812

Sousa, S., Määttä, J., 2016. The role of tumour-associated macrophages in bone metastasis. Journal of Bone Oncology, The microenvironment in bone metastasis 5, 135–138. https://doi.org/10.1016/j.jbo.2016.03.004

Srivastava, N., Hinton, G., Krizhevsky, A., Sutskever, I., Salakhutdinov, R., 2014. Dropout: A Simple Way to Prevent Neural Networks from Overfitting. Journal of Machine Learning Research 15, 1929–1958.

St. Onge, E.L., Miller, S., Clements, E., 2012. Sitagliptin/Metformin (Janumet) as Combination Therapy In the Treatment of Type-2 Diabetes Mellitus. P T 37, 699–708.

Stammer, K., Edassery, S.L., Barua, A., Bitterman, P., Bahr, J.M., Hales, D.B., Luborsky, J.L., 2008. Selenium-Binding Protein 1 expression in ovaries and ovarian tumors in the laying hen, a spontaneous model of human ovarian cancer. Gynecologic Oncology 109, 115–121. https://doi.org/10.1016/j.ygyno.2007.12.030

Starbuck, K., Al-Alem, L., Eavarone, D.A., Hernandez, S.F., Bellio, C., Prendergast, J.M., Stein, J., Dransfield, D.T., Zarrella, B., Growdon, W.B., Behrens, J., Foster, R., Rueda, B.R., 2018. Treatment of ovarian cancer by targeting the tumor stem cell-associated carbohydrate antigen, Sialyl-Thomsen-nouveau. Oncotarget 9, 23289–23305. https://doi.org/10.18632/oncotarget.25289

Strokotov, D.I., Yurkin, M.A., Gilev, K.V., van Bockstaele, D.R., Hoekstra, A.G., Rubtsov, N.B., Maltsev, V.P., 2009. Is there a difference between T- and B-lymphocyte morphology? J Biomed Opt 14, 064036. https://doi.org/10.1117/1.3275471

Strupler, M., Pena, A.-M., Hernest, M., Tharaux, P.-L., Martin, J.-L., Beaurepaire, E., Schanne-Klein, M.-C., 2007. Second harmonic imaging and scoring of collagen in fibrotic tissues. Opt. Express, OE 15, 4054–4065. https://doi.org/10.1364/OE.15.004054

Szabova, L., Yin, C., Bupp, S., Guerin, T.M., Schlomer, J.J., Householder, D.B., Baran, M.L., Yi, M., Song, Y., Sun, W., McDunn, J.E., Martin, P.L., Dyke, T.V., Difilippantonio, S., 2012. Perturbation of Rb, p53, and Brca1 or Brca2 Cooperate in Inducing Metastatic Serous Epithelial Ovarian Cancer. Cancer Res 72, 4141–4153. https://doi.org/10.1158/0008-5472.CAN-11-3834

Szegedy, C., Liu, W., Jia, Y., Sermanet, P., Reed, S.E., Anguelov, D., Erhan, D., Vanhoucke, V., Rabinovich, A., 2014. Going Deeper with Convolutions. CoRR abs/1409.4842.

Tajbakhsh, N., Shin, J.Y., Gurudu, S.R., Hurst, R.T., Kendall, C.B., Gotway, M.B., Jianming Liang, null, 2016. Convolutional Neural Networks for Medical Image Analysis: Full Training or Fine Tuning? IEEE Trans Med Imaging 35, 1299–1312. https://doi.org/10.1109/TMI.2016.2535302

Takada, T., Yagi, Y., Maekita, T., Imura, M., Nakagawa, S., Tsao, S.-W., Miyamoto, K., Yoshino, O., Yasugi, T., Taketani, Y., Ushijima, T., 2004. Methylation-associated silencing of the Wnt antagonist SFRP1 gene in human ovarian cancers. Cancer Sci. 95, 741–744.

Tang, Z., Lu, B., Hatch, E., Sacks, S.H., Sheerin, N.S., 2009. C3a Mediates Epithelial-to-Mesenchymal Transition in Proteinuric Nephropathy. JASN 20, 593–603. https://doi.org/10.1681/ASN.2008040434

Tapper, J., Kettunen, E., El-Rifai, W., Seppälä, M., Andersson, L.C., Knuutila, S., 2001. Changes in gene expression during progression of ovarian carcinoma. Cancer Genet. Cytogenet. 128, 1–6.

Teodoridis, J.M., Hall, J., Marsh, S., Kannall, H.D., Smyth, C., Curto, J., Siddiqui, N., Gabra, H., McLeod, H.L., Strathdee, G., Brown, R., 2005. CpG Island Methylation of DNA Damage Response Genes in Advanced Ovarian Cancer. Cancer Research 65, 8961–8967. https://doi.org/10.1158/0008-5472.CAN-05-1187

Testa, J.R., Getts, L.A., Salazar, H., Liu, Z., Handel, L.M., Godwin, A.K., Hamilton, T.C., 1994. Spontaneous transformation of rat ovarian surface epithelial cells results in well to poorly differentiated tumors with a parallel range of cytogenetic complexity. Cancer Res. 54, 2778–2784.

The Wellcome Trust Case-Control Consortium, The Australian Cancer Study (Ovarian Cancer), The Australian Ovarian Cancer Study Group, the Ovarian Cancer Association Consortium (OCAC), Goode, E.L., Chenevix-Trench, G., Song, H., Ramus, S.J., Notaridou, M., Lawrenson, K., Widschwendter, M., Vierkant, R.A., Larson, M.C., Kjaer, S.K., Birrer, M.J., Berchuck, A., Schildkraut, J., Tomlinson, I., Kiemeney, L.A., Cook, L.S., Gronwald, J., Garcia-Closas, M., Gore, M.E., Campbell, I., Whittemore, A.S., Sutphen, R., Phelan, C., Anton-Culver, H., Pearce, C.L., Lambrechts, D., Rossing, M.A., Chang-Claude, J., Moysich, K.B., Goodman, M.T., Dörk, T., Nevanlinna, H., Ness, R.B., Rafnar, T., Hogdall, C., Hogdall, E., Fridley, B.L., Cunningham, J.M., Sieh, W., McGuire, V., Godwin, A.K., Cramer, D.W., Hernandez, D., Levine, D., Lu, K., Iversen, E.S., Palmieri, R.T., Houlston, R., van Altena, A.M., Aben, K.K.H., Massuger, L.F.A.G., Brooks-Wilson, A., Kelemen, L.E., Le, N.D., Jakubowska, A., Lubinski, J., Medrek, K., Stafford, A., Easton, D.F., Tyrer, J., Bolton, K.L., Harrington, P., Eccles, D., Chen, A., Molina, A.N., Davila, B.N., Arango, H., Tsai, Y.-Y., Chen, Z., Risch, H.A., McLaughlin, J., Narod, S.A., Ziogas, A., Brewster, W., Gentry-Maharaj, A., Menon, U., Wu, A.H., Stram, D.O., Pike, M.C., Beesley, J., Webb, P.M., Chen, X., Ekici, A.B., Thiel, F.C., Beckmann, M.W., Yang, H., Wentzensen, N., Lissowska, J., Fasching, P.A., Despierre, E., Amant, F., Vergote, I., Doherty, J., Hein, R., Wang-Gohrke, S., Lurie, G., Carney, M.E., Thompson,

P.J., Runnebaum, I., Hillemanns, P., Dürst, M., Antonenkova, N., Bogdanova, N., Leminen, A., Butzow, R., Heikkinen, T., Stefansson, K., Sulem, P., Besenbacher, S., Sellers, T.A., Gayther, S.A., Pharoah, P.D.P., 2010. A genome-wide association study identifies susceptibility loci for ovarian cancer at 2q31 and 8q24. Nature Genetics 42, 874–879. https://doi.org/10.1038/ng.668

Thomas, E.D., Meza-Perez, S., Bevis, K.S., Randall, T.D., Gillespie, G.Y., Langford, C., Alvarez, R.D., 2016. IL-12 Expressing oncolytic herpes simplex virus promotes anti-tumor activity and immunologic control of metastatic ovarian cancer in mice. J Ovarian Res 9. https://doi.org/10.1186/s13048-016-0282-3

Torre, L.A., Trabert, B., DeSantis, C.E., Miller, K.D., Samimi, G., Runowicz, C.D., Gaudet, M.M., Jemal, A., Siegel, R.L., 2018. Ovarian cancer statistics, 2018. CA: A Cancer Journal for Clinicians 68, 284–296. https://doi.org/10.3322/caac.21456

Touma, S.E., Perner, S., Rubin, M.A., Nanus, D.M., Gudas, L.J., 2009. Retinoid metabolism and ALDH1A2 (RALDH2) expression are altered in the transgenic adenocarcinoma mouse prostate model. Biochemical Pharmacology 78, 1127–1138. https://doi.org/10.1016/j.bcp.2009.06.022

Trabert, B., Pinto, L., Hartge, P., Kemp, T., Black, A., Sherman, M.E., Brinton, L.A., Pfeiffer, R.M., Shiels, M.S., Chaturvedi, A.K., Hildesheim, A., Wentzensen, N., 2014. Pre-diagnostic serum levels of inflammation markers and risk of ovarian cancer in the Prostate, Lung, Colorectal and Ovarian Cancer (PLCO) Screening Trial. Gynecol Oncol 135, 297–304. https://doi.org/10.1016/j.ygyno.2014.08.025

Tseng, C.-H., 2015. Metformin reduces ovarian cancer risk in Taiwanese women with type 2 diabetes mellitus. Diabetes Metab. Res. Rev. 31, 619–626. https://doi.org/10.1002/dmrr.2649

Turner, T.B., Meza-Perez, S., Londoño, A., Katre, A., Peabody, J.E., Smith, H.J., Forero, A., Norian, L.A., Straughn, J.M., Buchsbaum, D.J., Rand all, T.D., Arend, R.C., 2017. Epigenetic modifiers upregulate MHC II and impede ovarian cancer tumor growth. Oncotarget 8, 44159–44170. https://doi.org/10.18632/oncotarget.17395

Ueha, S., Shand, F.H.W., Matsushima, K., 2012. Cellular and Molecular Mechanisms of Chronic Inflammation-Associated Organ Fibrosis. Front Immunol 3. https://doi.org/10.3389/fimmu.2012.00071

Umehara, T., Richards, J.S., Shimada, M., 2018. The stromal fibrosis in aging ovary. Aging (Albany NY) 10, 9–10. https://doi.org/10.18632/aging.101370

Urpilainen, E., Marttila, M., Hautakoski, A., Arffman, M., Sund, R., Ilanne-Parikka, P., Arima, R., Kangaskokko, J., Puistola, U., Läärä, E., Hinkula, M., 2018. The role of metformin and statins in the incidence of epithelial ovarian cancer in type 2 diabetes: a cohort and nested case-control study. BJOG 125, 1001–1008. https://doi.org/10.1111/1471-0528.15151

Ursini, F., Grembiale, R.D., D'Antona, L., Gallo, E., D'Angelo, S., Citraro, R., Visca, P., Olivieri, I., De Sarro, G., Perrotti, N., Russo, E., 2016. Oral Metformin Ameliorates Bleomycin-Induced Skin Fibrosis. J. Invest. Dermatol. 136, 1892–1894. https://doi.org/10.1016/j.jid.2016.05.097

Urzúa, U., Best, L., Munroe, D.J., 2010. Microarray proteomic analysis discriminates tumorigenic mouse ovarian surface epithelial cells of divergent aggressive potential. Molecular BioSystems 6, 2521. https://doi.org/10.1039/c005220e

Urzúa, U., Roby, K.F., Gangi, L.M., Cherry, J.M., Powell, J.I., Munroe, D.J., 2006. Transcriptomic analysis of an in vitro murine model of ovarian carcinoma: Functional similarity to the human disease and identification of prospective tumoral markers and targets. Journal of Cellular Physiology 206, 594–602. https://doi.org/10.1002/jcp.20522

Vanderhyden, B.C., 2005. Loss of ovarian function and the risk of ovarian cancer. Cell Tissue Res. 322, 117–124. https://doi.org/10.1007/s00441-005-1100-1

Vidot, S., Witham, J., Agarwal, R., Greenhough, S., Bamrah, H.S., Tigyi, G.J., Kaye, S.B., Richardson, A., 2010. Autotaxin delays apoptosis induced by carboplatin in ovarian cancer cells. Cellular Signalling 22, 926–935. https://doi.org/10.1016/j.cellsig.2010.01.017

Walker, G., MacLeod, K., Williams, A.R.W., Cameron, D.A., Smyth, J.F., Langdon, S.P., 2007. Insulin-like Growth Factor Binding Proteins IGFBP3, IGFBP4, and IGFBP5 Predict Endocrine Responsiveness in Patients with Ovarian Cancer. Clinical Cancer Research 13, 1438–1444. https://doi.org/10.1158/1078-0432.CCR-06-2245

Walton, J., Blagih, J., Ennis, D., Leung, E., Dowson, S., Farquharson, M., Tookman, L.A., Orange, C., Athineos, D., Mason, S., Stevenson, D., Blyth, K., Strathdee, D., Balkwill, F.R., Vousden, K., Lockley, M., McNeish, I.A., 2016. CRISPR/Cas9-Mediated Trp53 and Brca2 Knockout to Generate Improved Murine Models of Ovarian High-Grade Serous Carcinoma. Cancer Res 76, 6118–6129. https://doi.org/10.1158/0008-5472.CAN-16-1272

Walton, J.B., Farquharson, M., Mason, S., Port, J., Kruspig, B., Dowson, S., Stevenson, D., Murphy, D., Matzuk, M., Kim, J., Coffelt, S., Blyth, K., McNeish, I.A., 2017. CRISPR/Cas9-derived models of ovarian high grade serous carcinoma targeting Brca1, Pten and Nf1, and correlation with platinum sensitivity. Sci Rep 7. https://doi.org/10.1038/s41598-017-17119-1

Wang, D., DuBois, R.N., 2015. Immunosuppression associated with chronic inflammation in the tumor microenvironment. Carcinogenesis 36, 1085–1093. https://doi.org/10.1093/carcin/bgv123

Wang, D., Khosla, A., Gargeya, R., Irshad, H., Beck, A.H., 2016. Deep Learning for Identifying Metastatic Breast Cancer. arXiv:1606.05718 [cs, q-bio].

Wang, Huamin, Rosen, D.G., Wang, Hua, Fuller, G.N., Zhang, W., Liu, J., 2006. Insulin-like growth factor-binding protein 2 and 5 are differentially regulated in ovarian cancer of different histologic types. Modern Pathology 19, 1149–1156. https://doi.org/10.1038/modpathol.3800637

Wang, M., Weng, X., Guo, J., Chen, Z., Jiang, G., Liu, X., 2016. Metformin alleviated EMT and fibrosis after renal ischemia-reperfusion injury in rats. Ren Fail 38, 614–621. https://doi.org/10.3109/0886022X.2016.1149770

Wang, X., Hausding, M., Weng, S.-Y., Kim, Y.O., Steven, S., Klein, T., Daiber, A., Schuppan, D., 2018. Gliptins Suppress Inflammatory Macrophage Activation to Mitigate Inflammation, Fibrosis, Oxidative Stress, and Vascular Dysfunction in Models of Nonalcoholic Steatohepatitis and Liver Fibrosis. Antioxid. Redox Signal. 28, 87–109. https://doi.org/10.1089/ars.2016.6953

Wang, Y., Hill, K.S., Fields, A.P., 2013. Protein Kinase Cι maintains a tumor-initiating cell phenotype that is required for ovarian tumorigenesis. Mol Cancer Res 11, 1624–1635. https://doi.org/10.1158/1541-7786.MCR-13-0371-T

Watson, J.M., Marion, S.L., Rice, P.F., Bentley, D.L., Besselsen, D.G., Utzinger, U., Hoyer, P.B., Barton, J.K., 2014. In vivo time-serial multi-modality optical imaging in a mouse model of ovarian tumorigenesis. Cancer Biol. Ther. 15, 42–60. https://doi.org/10.4161/cbt.26605

Weberpals, J.I., Clark-Knowles, K.V., Vanderhyden, B.C., 2008. Sporadic Epithelial Ovarian Cancer: Clinical Relevance of BRCA1 Inhibition in the DNA Damage and Repair Pathway. Journal of Clinical Oncology 26, 3259–3267. https://doi.org/10.1200/JCO.2007.11.3902

Wei, H., Zhao, L., Li, W., Fan, K., Qian, W., Hou, S., Wang, H., Dai, M., Hellstrom, I., Hellstrom, K.E., Guo, Y., 2013. Combinatorial PD-1 Blockade and CD137 Activation Has Therapeutic Efficacy in Murine Cancer Models and Synergizes with Cisplatin. PLoS One 8. https://doi.org/10.1371/journal.pone.0084927

Weigelin, B., Bakker, G.-J., Friedl, P., 2016. Third harmonic generation microscopy of cells and tissue organization. J. Cell. Sci. 129, 245–255. https://doi.org/10.1242/jcs.152272

Weiskirchen, R., Weiskirchen, S., Tacke, F., 2018. Organ and tissue fibrosis: Molecular signals, cellular mechanisms and translational implications. Mol. Aspects Med. https://doi.org/10.1016/j.mam.2018.06.003

Wen, B., Campbell, K.R., Tilbury, K., Nadiarnykh, O., Brewer, M.A., Patankar, M., Singh, V., Eliceiri, K.W., Campagnola, P.J., 2016. 3D texture analysis for classification of second harmonic generation images of human ovarian cancer. Sci Rep 6, 35734. https://doi.org/10.1038/srep35734

Wen, B.L., Brewer, M.A., Nadiarnykh, O., Hocker, J., Singh, V., Mackie, T.R., Campagnola, P.J., 2014. Texture analysis applied to second harmonic generation image data for ovarian cancer classification. J Biomed Opt 19, 096007. https://doi.org/10.1117/1.JBO.19.9.096007

Weng, S., Xu, X., Li, J., Wong, S.T.C., 2017. Combining deep learning and coherent anti-Stokes Raman scattering imaging for automated differential diagnosis of lung cancer. J Biomed Opt 22, 1–10. https://doi.org/10.1117/1.JBO.22.10.106017

Wentzensen, N., Poole, E.M., Trabert, B., White, E., Arslan, A.A., Patel, A.V., Setiawan, V.W., Visvanathan, K., Weiderpass, E., Adami, H.-O., Black, A., Bernstein, L., Brinton, L.A., Buring, J., Butler, L.M., Chamosa, S., Clendenen, T.V., Dossus, L., Fortner, R., Gapstur, S.M., Gaudet, M.M., Gram, I.T., Hartge, P., Hoffman-Bolton, J., Idahl, A., Jones, M., Kaaks, R., Kirsh, V., Koh, W.-P., Lacey, J.V., Lee, I.-M., Lundin, E., Merritt, M.A., Onland-Moret, N.C., Peters, U., Poynter, J.N., Rinaldi, S., Robien, K., Rohan, T., Sandler, D.P., Schairer, C., Schouten, L.J., Sjöholm, L.K., Sieri, S., Swerdlow, A., Tjonneland, A., Travis, R., Trichopoulou, A., van den Brandt, P.A., Wilkens, L., Wolk, A., Yang, H.P., Zeleniuch-Jacquotte, A., Tworoger, S.S., 2016. Ovarian Cancer Risk Factors by Histologic Subtype: An Analysis From the Ovarian Cancer Cohort Consortium. J Clin Oncol 34, 2888–2898. https://doi.org/10.1200/JCO.2016.66.8178

Williams, R.M., Flesken-Nikitin, A., Ellenson, L.H., Connolly, D.C., Hamilton, T.C., Nikitin, A.Y., Zipfel, W.R., 2010. Strategies for high-resolution imaging of

epithelial ovarian cancer by laparoscopic nonlinear microscopy. Transl Oncol 3, 181–194.
Wright, M.H., Calcagno, A.M., Salcido, C.D., Carlson, M.D., Ambudkar, S.V., Varticovski, L., 2008. Brca1 breast tumors contain distinct CD44+/CD24- and CD133+ cells with cancer stem cell characteristics. Breast Cancer Res 10, R10. https://doi.org/10.1186/bcr1855
Xiao, H., Ma, X., Feng, W., Fu, Y., Lu, Z., Xu, M., Shen, Q., Zhu, Y., Zhang, Y., 2010. Metformin attenuates cardiac fibrosis by inhibiting the TGFbeta1-Smad3 signalling pathway. Cardiovasc. Res. 87, 504–513. https://doi.org/10.1093/cvr/cvq066
Xing, D., Orsulic, S., 2006. A Mouse Model for the Molecular Characterization of Brca1-Associated Ovarian Carcinoma. Cancer Research 66, 8949–8953. https://doi.org/10.1158/0008-5472.CAN-06-1495
Yang-Hartwich, Y., Gurrea-Soteras, M., Sumi, N., Joo, W.D., Holmberg, J.C., Craveiro, V., Alvero, A.B., Mor, G., 2014. Ovulation and extra-ovarian origin of ovarian cancer. Sci Rep 4, 6116. https://doi.org/10.1038/srep06116
Yi, S.-Y., Hao, Y.-B., Nan, K.-J., Fan, T.-L., 2013. Cancer stem cells niche: A target for novel cancer therapeutics. Cancer Treatment Reviews 39, 290–296. https://doi.org/10.1016/j.ctrv.2012.10.004
Zhai, Y., Wu, R., Kuick, R., Sessine, M.S., Schulman, S., Green, M., Fearon, E.R., Cho, K.R., 2017. High-grade serous carcinomas arise in the mouse oviduct via defects linked to the human disease. J. Pathol. 243, 16–25. https://doi.org/10.1002/path.4927
Zhang, X., Zhang, C., Shen, S., Xia, Y. jie, Yi, L., Gao, Q., Wang, Y., 2013. Dehydroepiandrosterone induces ovarian and uterine hyperfibrosis in female rats. Hum. Reprod. 28, 3074–3085. https://doi.org/10.1093/humrep/det341
Zhao, G., Chen, J., Deng, Y., Gao, F., Zhu, J., Feng, Z., Lv, X., Zhao, Z., 2011. Identification of NDRG1-regulated genes associated with invasive potential in cervical and ovarian cancer cells. Biochemical and Biophysical Research Communications 408, 154–159. https://doi.org/10.1016/j.bbrc.2011.03.140
Zhong, W., Gao, L., Zhou, Z., Lin, H., Chen, C., Huang, P., Huang, W., Zhou, C., Huang, S., Nie, L., Liu, Y., Chen, Y., Zhou, D., Lv, Z., 2017. Indoleamine 2,3-dioxygenase 1 deficiency attenuates CCl4-induced fibrosis through Th17 cells down-regulation and tryptophan 2,3-dioxygenase compensation. Oncotarget 8, 40486–40500. https://doi.org/10.18632/oncotarget.17119
Zhou, F., Shi, L.-B., Zhang, S.-Y., 2017. Ovarian Fibrosis: A Phenomenon of Concern. Chin Med J (Engl) 130, 365–371. https://doi.org/10.4103/0366-6999.198931